Université catholique de Louvain
Ecole Polytechnique de Louvain

Heteropolar null-flux electrodynamic bearings for the passive radial suspension of rotors

Corentin Dumont de Chassart
Electromechanical engineer

PhD thesis
February 13th 2016

Members of the jury

Pr.	T. Pardoen	UCL - iMMC	President
Pr.	B. Dehez	UCL - iMMC	Supervisor
Pr.	P. Fisette	UCL - iMMC	
Pr.	A. Tonoli	Politecnico di Torino (Italy)	
Pr.	Ch. Espanet	Université de Franche-Comté (France)	
Dr.	V. Kluyskens	UCL - iMMC	

Abstract

Magnetic bearings allow to support a rotating object without contact. This makes them more suitable than mechanical bearings for applications where removing the wear and/or the lubrication is highly sought-after, for example. Nowadays, the magnetic bearings used in the industry are controlled actively. This requires the use of sensors, controllers and power electronics. However, the complexity, cost and overall dimensions associated with this control system can become prohibitive, especially for small rated power applications. A way to overcome these disadvantages could be the use of magnetic bearings that do not require external control means, i.e. passive bearings. Electrodynamics bearings (EDBs) belong to this category.

Electrodynamic bearings are based on the electromagnetic interaction forces between permanent magnets and currents flowing in a conductor. These currents are induced by the relative speed between the magnets and the conductors. For efficiency purposes, electrodynamic bearings are designed in such a way that there is no net variation in the permanent magnet flux linked by the winding when the rotor spins in a centered position. As a result, there are no induced currents, no forces, and above all no losses in the bearing when the rotor spins in a centered position. This characteristic is referred to as *null-flux*. It is found in all the designs of electrodynamic bearings that are studied nowadays. In contrast, when the rotor spins in an off-centered position, currents are induced in the winding. This creates a force on the rotor that tends to restore its centered position. In this case, the energy dissipated in the windings comes from the drive torque on the rotor that keeps the spin speed constant. On the one hand, this prevents the operation at zero spin speed. On the other hand, it eliminates the need for an additional electrical power supply to feed the bearing, as is the case for the existing active magnetic bearings. Finally, the absence of control system induces gains in compactness, simplicity, costs and reliability. As a result, electrodynamic bearings could be well suited for applications where these aspects are critical.

Despite these advantages, electrodynamic bearings have not made their way out

of the labs yet due to their low stiffness and stability issues. In this context, this thesis aims at taking one further step toward the implementation of heteropolar electrodynamic bearings in practical applications. To this end, new design guidelines and models are proposed, validated, and applied to different case studies.

Indeed, the design of a new electrodynamic bearing is usually based on the intuition and experience of its inventor. This work proposes guidelines to ease this design process. The guidelines are deduced by imposing the null-flux characteristic to a bearing comprising magnets with radial magnetic field and a winding with an arbitrary shape. This yields the identity $q = p \pm 1$, where q and p are the number of pole pairs of the winding and permanent magnets, respectively. Based on these guidelines, new bearing topologies are also introduced.

Regarding the modeling, recent years have seen the emergence of a new kind of model of electrodynamic bearings. As opposed to the previous ones, this model is dynamic, i.e. obtained without making any assumption on the kinematics of the rotor axis. This opened the possibility of performing stability analyses in a rigorous way. Furthermore, the stability can be analyzed using conventional system analysis tools, because the model takes the form of a linear state-space representation. This thesis proposes a dynamic model with an enlarged scope, i.e. suitable for a wider range of bearing geometries. Thanks to this model, the performance and stability of various EDBs can be optimized and compared to find the most appropriate solution for a given application.

Although various embodiments of heteropolar bearings have been proposed, very few efforts have been dedicated to the evaluation and optimization of their performance, and the actual potential of heteropolar EDBs still needs to be evaluated. In this aim, a graphical method based on the analysis of the root locus of the system is proposed. It is then applied to the comparison of bearings with different winding yoke permeabilities. Based on the dynamic model developed in this thesis, the optimization of the stability and stiffness of a yokeless bearing is also carried out, yielding a Pareto front of optimal bearings. These optimal bearings are finally compared to existing homopolar and heteropolar embodiments in terms of stiffness to magnet volume ratio, showing that similar ratios can be obtained.

Lastly, the bearing dynamic model is applied to the prediction of balancing radial electrodynamic forces due to rotor eccentricities in permanent magnet machines. The main assumptions of the model are validated to show its applicability in this case, and the forces from the model are compared to finite element simulation results, showing a good agreement between both predictions.

Acknowledgements

My first thanks go to my supervisor Bruno Dehez, for his unshakeable and contagious trust in the relevance of this research topic, his creative advices, and his continuous support when carrying out the present work. The French word for 'supervisor' is 'promoteur', from the Latin *promovere* - move forward, cause to advance - that yielded 'to promote' in English. Prof. Dehez is a true 'promoter'.

Special thanks to him and Virginie Kluyskens for the intellectually stimulating brain-storming sessions that fed my motivation along this thesis.

I am grateful to the members of the supervising committee/examining board for their valuable insights and feedbacks during the thesis, and for taking the time to review this work. More precisely, my thanks go to:

- Dr Virginie Kluyskens for sharing her expertise and supporting me, especially with communication aspects;
- Prof. Paul Fisette for creating such a lively atmosphere in our corridor, and in the choir;
- Prof. Andrea Tonoli and his team for their great technical insights and the shared enthusiasm about electrodynamic bearings. I remember the warm welcome by the LIM during my stay at Politecnico di Torino;
- Prof. Christophe Espanet, Adrien Gilson, and MMT for the realization of the rotor for the bearing prototype;
- Prof. Thomas Pardoen for chairing the examining board of this thesis.

My gratitude also goes to my colleagues for the kind and lively atmosphere at the CEREM that made me rejoice and jump out of bed every morning. In particular, thanks to my fellow office-mates Virginia, Guillaume, Joachim, Deron, and David

for feeding me with bananas, speeculoos, cupcakes, candies, and jokes that have now transformed into a thesis.

I appreciated a lot the help of the technical and administrative staff. Thanks to Catherine Bauwens, Paul Sente, and Astrid Leduc for their exemplary availability and willingness to help, and to Axel Jottard for sharing his experience and providing smart advices when designing the mechanical parts of the test bench. Thanks also to André Lengelé for helping me with the minor but numerous technical issues that come along with experimental works.

My deepest gratitude is due to the Université catholique de Louvain for financing this work through the Special Research Fund (FSR).

Last but not least, I thank my relatives and friends for their kindness and joyful presence. You guys make visible the love that drives everything.

Contents

Introduction 1

Context and motivations

Magnetic bearings support the moving part of a rotating machine through electromagnetic forces. The absence of contact between the rotating and stationary parts yields numerous advantages. For example, the elimination of mechanical wear increases the bearing lifetime, thereby reducing the maintenance cost in remote applications such as sub sea compressors. Besides, the reduction in friction losses allows for higher energy efficiencies, e.g. in high speed turbomachinery. Another advantage is the absence of lubrication. It eliminates the need of lubrication seals and prevents contamination. These assets are particularly sought after in rotating machinery aimed at transporting aggressive or very pure fluids, and in turbomolecular vacuum pumps.

Nowadays, the vast majority of magnetic bearings is actively controlled. This yields additional advantages as it opens the possibility for compensating unbalances and damping vibration modes when running at higher speeds. As a result, active magnetic bearings are now integrated in an increasing number of applications from the oil and gas to the semiconductor and power generation industries (Schweitzer and Maslen, 2009; SKF, 2016).

Despite their numerous advantages, the spread of active magnetic bearings is still limited by some drawbacks that are associated with the control system, among others (Looser and Kolar, 2014). This system involves sensors, actuators, power amplifiers, and control electronics that increase the complexity, overall dimensions, and cost of the suspension. Furthermore, the suspension relies on a power supply, making the whole system more sensitive to power cuts. As a result, more attention is drawn to bearings that do not require a control system i.e., passive magnetic bearings.

To design a passive suspension, the most intuitive solution consists in assembling permanent magnets to guide the rotor in the axial and radial directions. However,

stable levitation cannot be achieved by using only permanent magnets, as demonstrated by Earnshaw (1842) and Braunbek (1939a,b). More specifically, this theorem states that the sum of the stiffnesses associated with the interaction forces between stationary magnets is zero. As a consequence, the stiffness is negative in at least one direction, and the rotor cannot be supported stably. For example, the ratio of axial to radial stiffness is -2 for permanent magnet configurations with rotational symmetry (Jungmayr et al., 2014). As a consequence, other passive suspension means should be investigated to achieve stability. They could be used in combination with a permanent magnet assembly or alone. A first alternative involves strong diamagnetic materials, i.e. superconductors (Han et al., 2005). However, this requires a cooling system that gathers the same drawbacks as those cited above for active bearings. A second alternative lies in the gyroscopic stabilization which is implemented in the Levitron toy (Genta et al., 1999). However, this device is stable in a narrow spin speed range and remains very sensitive to external disturbances due to its weak radial stiffness. A third option consists in a bearing based on magnetic fields that are not static. Electrodynamic bearings (EDBs) belong to this category.

Electrodynamic bearings (EDBs) comprise permanent magnets and conductors rotating relative to each other. Due to this rotation, the magnetic flux linked by the conductors varies, thereby inducing electromotive forces and currents in the conductors, as predicted by the laws of Faraday and Lenz. This in turn results in forces tending to restore the nominal position of the rotor. During operation, the energy dissipated in the conductors comes from the drive torque on the rotor to keep the spin speed constant. On the one hand, this prevents the operation at zero spin speed. On the other hand, it eliminates the need for an additional electrical power supply to feed the bearing.

Preferably, EDBs are null-flux i.e., they are designed in such a way that the flux linked by the conductors varies only when the rotor is off-centered (Danby, 1971). This drastically reduces the unnecessary currents and losses when the rotor spins in the nominal position, which increases the energy efficiency and avoids thermal issues. As a result, most of the recent studies focus on null-flux EDBs. Finally, EDBs can be categorized into different groups, depending on whether they provide axial or radial support, and whether the magnetic field source is homopolar or heteropolar. More specifically, the conductors of null-flux homopolar bearings can be bulk or wound and experience a field created by a single magnetic pole, whereas the conductors of null-flux heteropolar bearings must be wound and experience a field created by more than one pole, see Fig. 1.1.

Radial homopolar bearings have focused much interest in recent years, yielding significant improvements in their modeling (Detoni, 2012; Kluyskens, 2011; Lembke, 2005) and a successful levitation test (Filatov, 2002). In particular, the conducting part of homopolar bearings can be made out of bulk materials, which eases their

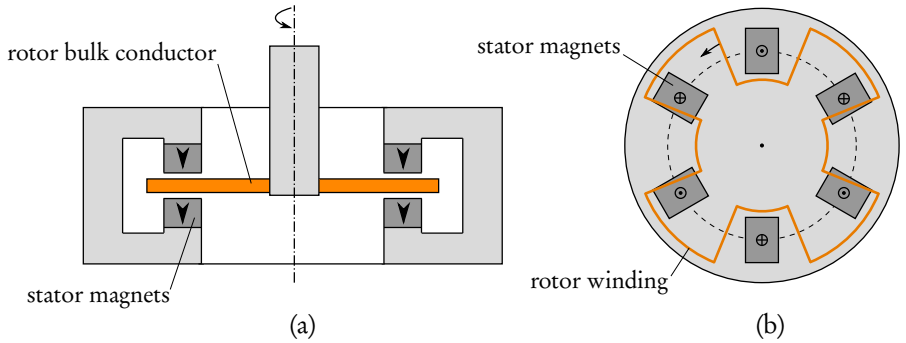

Fig. 1.1: Electrodynamic bearings are categorized into different groups, depending on whether the field experienced by the conductors are created by one of more magnetic poles. (a) Schematic view of a homopolar bearing. The parts are axisymmetric. (b) Schematic view of a heteropolar bearing.

construction. Axial heteropolar bearings drew the attention of researchers too, also resulting in improved models (Bachovchin et al., 2013; Impinna et al., 2013), and a successful levitation test (Sandtner and Bleuler, 2004). For an extensive review of electrodynamic bearings, the reader is referred to (Detoni, 2014).

This thesis is concerned with null-flux, radial heteropolar EDBs. Various embodiments of heteropolar bearings have been proposed and/or patented so far. A first patent was filed in the USA by Danby (1971). It was followed by many others proposed by the teams of Basore, Pinkerton, Davey, and Post in the USA, and by the team of Murakami in Japan. In the design of these bearings, a lot of attention was paid to obtaining the null-flux characteristic. However, general guidelines to be followed for designing null-flux heteropolar bearings do not appear to have been derived yet.

Models of heteropolar EDBs have been proposed by the teams lead by Davey, Post, Murakami, Eichenberg, and Takanashi. These works include some validations based on numerical simulations and a few experimental results. However, the models were derived for specific embodiments. Consequently, they cannot be used to compare different bearing solutions on an objective basis. Furthermore, they neglect the impact of the speed of the rotor center on the electrical variables, i.e. the rotor is assumed to spin in a static eccentricity configuration. This kinematic assumption is usually referred to as the quasi-static assumption, and constitutes a strong limitation for a model that is aimed at studying the rotor dynamics. Recently, this drawback was overcome as Detoni et al. (2012) proposed a model with no assumption on the rotor kinematics, i.e. a dynamic model. Nevertheless, the scope of this model should be enlarged to include a wider range of bearings and allow for comparisons.

Although a successful levitation test was reported by Murakami et al. (1996),

heteropolar EDBs are still under study in the laboratories because of their low stiffness and stability issues. These drawbacks led to the conclusion that electrodynamic bearings may not compete with active bearings. Besides, the research should instead focus on the implementation of EDBs in other niche applications where their abovementioned advantages in terms of cost, compactness, and simplicity are highly valued. Potential applications include the support of the flywheel of a stationary energy storage system, or the support of a satellite reaction wheel.

This thesis further investigates the use of null-flux heteropolar EDBs for the radial suspension of rotors. In this aim, new bearing embodiments and models are presented. These models are then applied to the comparison and the optimization of EDBs, and to the prediction of radial electrodynamic forces in permanent magnet (PM) machines.

Manuscript organization and content

This manuscript is organized as follows. First, the state of the art in the field of heteropolar EDBs is presented. Then, new models of EDBs are proposed. Finally, these models are applied to different study cases.

State of the art

Chapter 2 is a review of the literature about heteropolar EDBs. A first section presents the operating principle of EDBs and gathers the existing designs. This section discusses the qualities of these bearings, such as the null-flux characteristic. From this, it appears that a wide variety of bearings have been proposed, but general guidelines for their design are lacking. At the end of this section, additional bearing topologies are finally proposed. These embodiments are based upon design guidelines that are derived in the following chapters.

The second section of this chapter concerns the modeling. First, the different kinds of models used to predict the behaviour of EDBs are exposed from a broad perspective. Then, a review of the existing models of null-flux heteropolar bearings is presented. In particular, the existence of practical implementations or experimental validations is pointed out. As stated above, the use of the existing models is either limited by the static eccentricity assumption or by their narrow scopes.

Modeling

Predicting the behavior of a rotor supported by EDBs requires an electromechanical model of the complete system. Such model usually consists in a lumped-parameter model whose parameters are identified through an electromagnetic field model. In this work, the field models belong to the literature, whereas the focus is put on the

lumped-parameter models. Two original models of this kind are derived. One is quasi-static whereas the other is dynamic.

Chapter 3 presents a quasi-static model predicting the forces on the rotor of the electrodynamic bearings introduced in chapter 2. From the analysis of this model, general guidelines for the design of null-flux heteropolar bearings are proposed. These results are validated through finite element analyses.

The static-eccentricity assumption precludes the use of this model to predict the dynamics and analyze the stability of a rotor supported by EDBs. However, the model considers the full harmonic content of the permanent magnet field. This allows for studying the impact of higher order harmonics on the average and pulsating components of the forces e.g..

Chapter 4 introduces a new dynamic, lumped-parameter model with an enlarged scope that allows to consider a wider range of bearing topologies. It consists in a linear state-space representation comprising six parameters that fully characterize the dynamic behavior of a bearing. From these parameters, the performance of heteropolar EDBs can be evaluated and compared.

This dynamic model includes no assumption on the rotor kinematics and can thus be used to study the dynamics and stability of rotors supported by EDBs. However, in order for the model to yield a linear governing equation, only the main harmonic of the permanent magnet field is considered. The relevance of this assumption can be checked using the quasi-static model developed in chapter 3, highlighting the complementarity of both kinds of models.

Model applications

The tools developed in the previous chapters aim at evaluating the performance of EDBs, e.g. their stiffness and stability. They can be applied to the comparison and/or the optimization of bearings. They can also be applied to the prediction of radial electrodynamic forces due to the presence of rotor eccentricities in permanent magnet machines.

Chapter 5 first proposes two performance criteria for EDBs, considering their low stiffness and the difficulty of introducing some damping to stabilize the rotor. These criteria are the radial stiffness and the amount of damping required for stability. Then, a graphical method for evaluating these criteria based on a root locus is exposed. The roots are obtained by calculating the eigenvalues of a system obtained following another approach than in chapter 3. This system is simpler as it is based upon a quasi-static model. Although the quasi-static assumption is restricting, this

allows for deriving analytical expressions of the roots, the analysis of which yields the graphical performance evaluation method.

This method is then applied in the second section of this chapter to investigate the impact of the yoke material on the performance of EDBs. In this aim, the stiffness and stability of two bearing with the same geometry but different yoke permeabilities are compared. It is shown that in some cases, the magnetic permeability of the yoke has a very low impact on the bearing performance. Finally, the graphical method derived in the previous section is validated by comparing its predictions to those of the dynamic model from chapter 4.

In a third section, the optimization of a yokeless electrodynamic bearing using the dynamic model from chapter 4 is presented. This optimization is carried out following two objectives. The bearing stiffness is maximized, whereas the required amount of damping to reach the stability is minimized, yielding a Pareto front of optimal solutions. This front provides an upper limit for the performance of the yokeless bearing. The Pareto-optimal bearings are then compared to the state of the art, showing that they can reach a reasonable stiffness to permanent magnet volume ratio compared to the existing homopolar and heteropolar EDBs.

Chapter 6 studies the effect of the rotor off-centering in permanent magnet motors using the model developed in chapter 4. In permanent magnet motors, the presence of rotor eccentricities can alter the airgap field distribution. This results in parasitic radial detent forces that can be reduced by connecting the stator phases in parallel. As a consequence, currents are passively induced in the windings when the rotor spins in an off-centered position, yielding balancing electrodynamic forces. In this chapter, the main assumptions of the model are validated in the particular case of a slotted permanent magnet motor, and its parameters are evaluated. Finally, the centering electrodynamic forces predicted by the model are compared to finite element simulation results for validation.

State of the Art

2

This section presents the state of the art in the field of heteropolar electrodynamic bearings, with a focus on null-flux topologies. In a first section, the operating principle of EDBs is presented. This is followed by a summary of the various designs of heteropolar EDBs that have been proposed in the literature. Then, additional designs are proposed. A second section gathers the models of EDBs from the literature, as well as the results of the existing experimental tests.

2.1 Topologies

Various designs of heteropolar EDBs have been proposed in the literature. This section presents their operating principle and topologies.

2.1.1 Operating principle

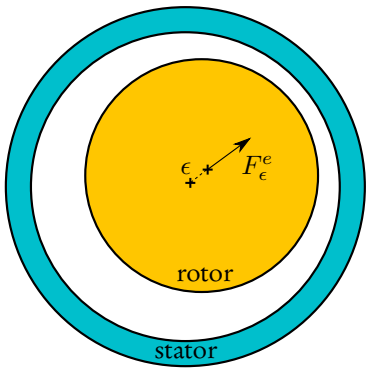

Fig. 2.1: Rotor eccentricity and centering force.

The operation of passive heteropolar EDB relies on electrodynamic forces to center the rotor. In presence of linear materials, this centering force is given by (Grenier et al., 2009):

$$F_{\epsilon}^{e} = \sum_{k=1}^{N} \frac{\partial \Phi_k}{\partial \epsilon} I_k, \tag{2.1}$$

where Φ_k is the PM flux linkage in the k^{th} phase, I_k is the phase current, and N is the number of phases. The eccentricity of the rotor with respect to the stator is denoted ϵ, and the centering force is denoted F_{ϵ}^{e}, see Fig. 2.1.

Another force component that is not aligned with the eccentricity exists, but it is not considered at this point. From (2.1), it appears that the centering electrodynamic force thus results from the combined presence of:

- a gradient of PM flux linkage in the winding. As the magnetic field source is heteropolar, the PM flux linkage vary with time when the rotor spins. A flux gradient means that the amplitude of this variation changes with the eccentricity ϵ;
- a current in the winding. In passive bearings, the winding phases are short-circuited. The current appears because of Faraday's law of induction and opposes the PM flux variation, following Lenz's law.

In the particular case of a null-flux bearing, the winding is such that the amplitude of the flux linkage variation cancels when the rotor is centered. In this situation, no currents are induced, which lowers the Joule losses. However, the gradient of the flux linkage is non-zero to ensure the presence of a centering force. Therefore, the flux linkage is non-zero when the rotor is off-centered and varies with time, thereby inducing currents in the winding. As a consequence, when the rotor is off-centered, both terms $\frac{\partial \Phi_k}{\partial \epsilon}$ and I_k are non-zero in (2.1), which results in a centering force on the rotor.

It follows from the above analysis that, in the following bearing descriptions, the emphasis is given to identifying the flux linkage gradient instead of describing the operation of each bearing in more detail. The null-flux bearings are also pointed out.

Finally, let us illustrate the operating principle of null-flux EDBs by considering the heteropolar bearing shown in Fig. 2.2 (a). It has a stator comprising a single short-circuited conducting phase with two pole pairs. The rotor comprises PMs creating a magnetic field with one pole pair, represented by the blue field lines in Fig. 2.2 (b). The flux linked by the winding can be calculated by integrating the field lines crossing the red areas denoted 1 and 2 in Fig. 2.2 (c), in the direction shown by the red arrows. When the rotor is centered, four field lines cross each of these two areas, but in opposite directions with respect to the red arrows. Therefore, the total

flux linkage in the conducting loop is zero. This remains true as the rotor spins and therefore the phase flux linkage does not vary and no reaction currents or force appear. The bearing has the null-flux characteristic.

The off-centered rotor case is shown in Fig. 2.2 (d). As the number of field lines crossing the areas 1 and 2 are not equal anymore, the phase flux linkage is not zero anymore, and the rotation of the rotor implies a variation of the flux linkage in the winding. This non-zero flux linkage gradient results in reaction or eddy currents tending to oppose the flux variation in the winding. The interaction between the current induced in the conductors and the PM field induces a force that tends to restore the centered position of the rotor. The operation of EDBs is based upon this centering force.

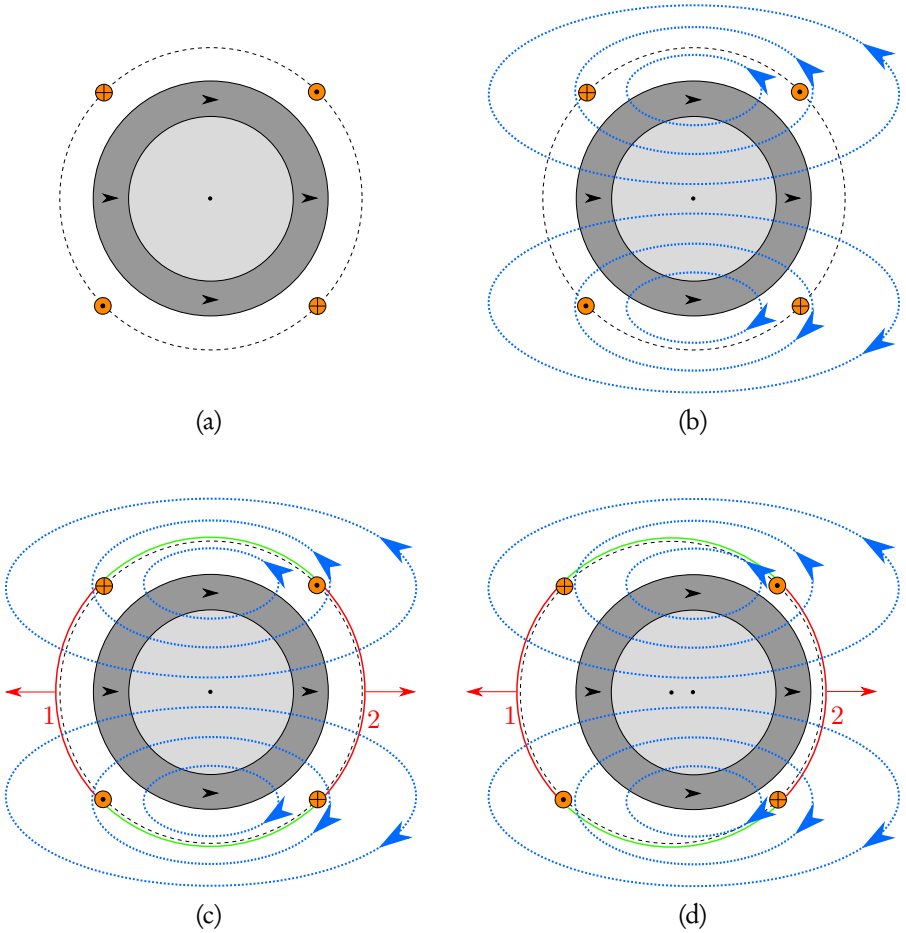

Fig. 2.2: Cross-sectional view of a heteropolar EDB with a one pole pair rotor and a two pole pairs stator winding. (a) Centrifugal compressor supported by active magnetic bearings.

2.1.2 Post et al

(Post, 1999) is a patent covering a bearing with two possible kinds of windings as shown in Fig. 2.3. The bearings comprise a Halbach array of PMs with an even number of pole pairs on the rotor and windings on the stator. The stator can be internal or external.

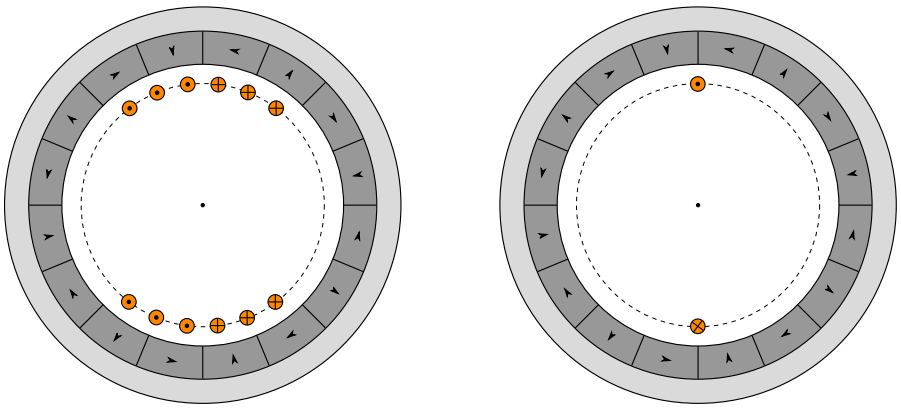

Fig. 2.3: Schematic sectional views of the bearings from (Post, 1999), in the case of PMs with 4 pole pairs and an external rotor. Only one phase is shown. (a) Lap winding. (b) "Window frame" winding.

The lap winding configuration is shown in Fig. 2.3 (a). Each phase is made of two identical parts located 180^o azimuthally from each other. When the rotor is centered, the upper and lower parts in Fig. 2.3 (a) link the same flux. Therefore, they are cross-coupled connected so that the total magnetic flux linked by the phase cancels, and the bearing has the null-flux characteristic. On the other hand, the flux linkage in the upper and lower parts differ from each other when the rotor is off-centered. Then, the total flux in the phase is non-zero, highlighting the presence of a flux linkage gradient.

The "window frame" winding configuration with the axial wires lying transversely across the stator is shown in Fig. 2.3 (b). As the number of PM pole pairs is even, the null-flux characteristic is readily apparent, as well as the flux linkage gradient.

(Post, 1998) is a patent from the same author, covering the bearing shown in Fig. 2.4 (a). It comprises two arrays of PMs fixedly attached together and a winding with short-circuited phases. The PMs can be on the rotor or vice-versa.

The two PMs arrays have identical pole pairs numbers and face each other so that the radial component of the PM field cancels at a radius equal to the radius of the

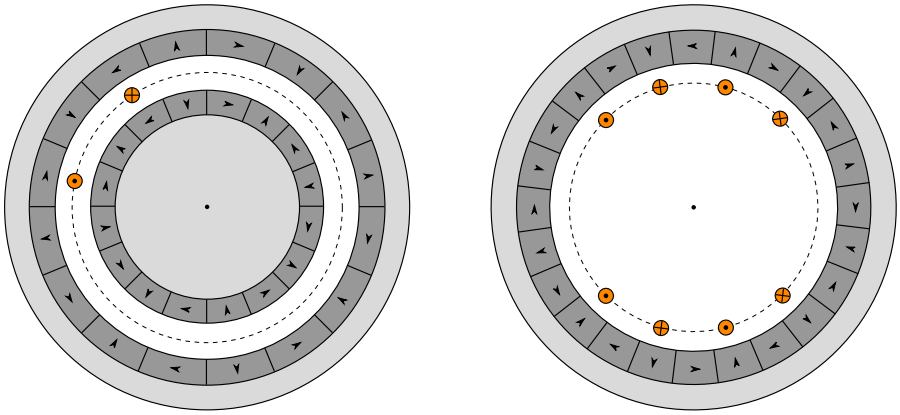

(a) (b)

Fig. 2.4: Sectional views of the bearings from patent (Post, 1998) (a) and (Post, 2006) (b). Only one phase is shown in each case.

winding. Therefore, the flux linkage in the winding phases cancels when the rotor is centered and the bearing has the null-flux characteristic. As shown in Fig. 2.4 (a), the azimuthal spacing between the two legs of each phase is equal to one pole pitch of the PM field. Therefore, the flux linkage is non-zero when the rotor is off-centered, highlighting the flux linkage gradient.

(Post, 2006) is also a patent. The bearing in question is shown in Fig. 2.4 (b) in the particular case of PMs with 6 pairs of poles. It comprises a single array of PMs on the rotor and a winding with two short-circuited phases on the stator. The first winding phase is disposed symmetrically about the vertical plane as shown in Fig. 2.4 (b). The second phase is disposed symmetrically about the horizontal plane and is not represented here. These two phases may not be identical, but each of them is composed of two identical subparts arranged symmetrically around the stator axis. Within each subpart, the axial wires are azimuthally spaced apart from each other by one pole pitch of the PM field. The subparts are connected in such a way as to have the null-flux characteristic. More specifically, the subparts are cross-coupled connected if the PM pole pairs number is odd; they are series connected if the PM pole pairs number is even, which is the case in Fig. 2.4 (b). As a result, the flux linkage equalizes in both subparts when the rotor is centered. This is not the case when the rotor is off-centered, giving rise to a flux linkage gradient.

(Post, 1996) is a patent covering the bearing shown in Fig. 2.5. It is composed of a PM assembly and a conducting part. The PMs can be on the rotor or on the stator, and the rotor can be internal or external. The conducting part can either be made of a bulk conducting surface as shown in Fig. 2.5 (a), or include a multiplicity of wound

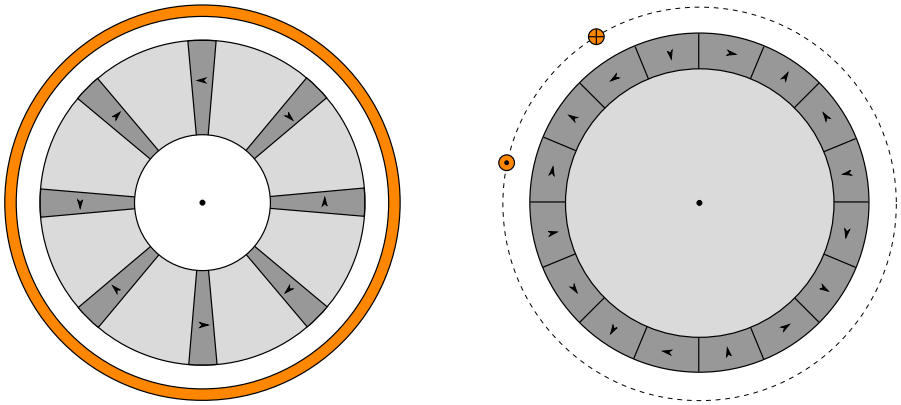

(a) (b)

Fig. 2.5: Schematic sectional views of the bearing from (Post, 1996) in the particular case of a PM field source with 4 pole pairs. (a) Bulk conductor case and (b) wound conductors case. Only one phase is shown.

phases as shown in Fig. 2.5 (b). These two configurations do not have the null-flux characteristic, although the patent applicant suggests to load the short-circuited phases with non-linear resistive or inductive elements to lower the Joule losses in the wound configuration. The flux linkage gradient arises from the air gap width variation as the rotor gets off-centered. The flux linkage increases in the phases near the narrow air gap regions and decreases in the phases near the large air gap regions.

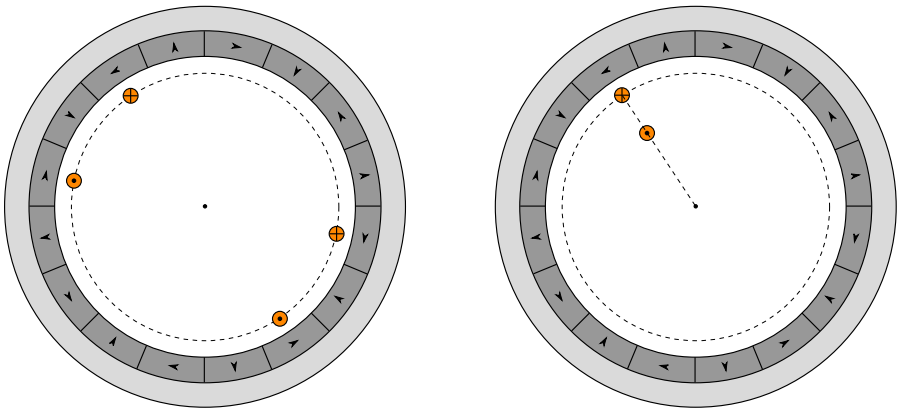

(a) (b)

Fig. 2.6: Sectional views of the bearings from (Post, 2012) (a) and (Post and Ruytov, 1998) (b) in the particular case of a PM field source with 4 pole pairs. Only one phase is shown.

(Post, 2012) covers the bearing shown in Fig. 2.6 (a). It includes a Halbach array of PMs on an external rotor and wound conductors on an internal stator. The PM pole pairs number is even. The winding phases are made of two subparts disposed symmetrically around the stator axis and connected in opposing series to obtain the null-flux characteristic. Each subpart spans an angular width of a half PM field wavelength as shown in Fig. 2.6 (a). The flux linkage gradient arises from the difference in PM flux linked by the two subparts when the rotor is off-centered. Finally, this bearing is similar to the one from Fig. 2.4 (b), except that each subpart includes only two conductors, and that the winding may include more than two phases.

(Post and Ruytov, 1998) covers the bearing shown in Fig. 2.6 (b). It includes a Halbach array on the external rotor and wound conductors on the internal stator. As can be seen in 2.6 (b), the bearing does not have the null-flux characteristic but the flux linkage gradient is present. For example, the flux linked by the phase depicted in the figure increases as the rotor with PMs is off-centered to the right-hand side.

2.1.3 Murakami et al

(Murakami, 1995) proposes a bearing with axial magnetic field. The stator includes a multiplicity of short-circuited phases lying between two rotating PM assemblies placed in attracting mode, as shown in Fig. 2.7 (a). Each assembly includes a multiplicity of PM pairs having opposite polarities and lying in the same plane. The two members of each pair lie at a same angular position but at different radii. An example of assembly with 8 PM pairs and phases with hexagonal shapes is shown in Fig. 2.7 (b).

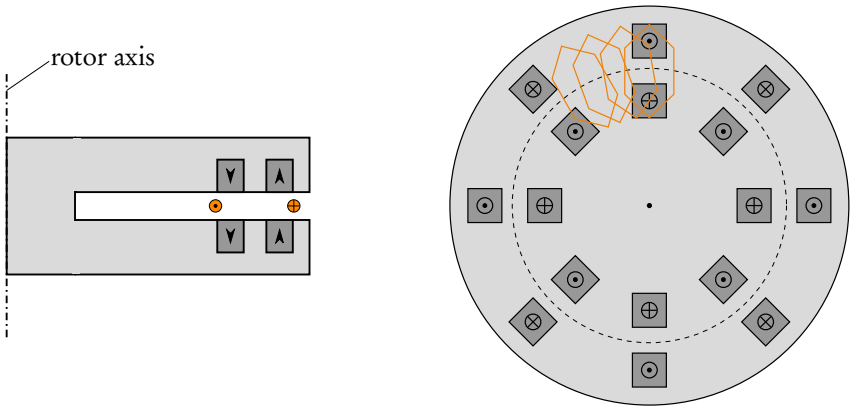

Fig. 2.7: Bearing proposed in (Murakami, 1995). (a) Sectional view of a bearing phase and the two PM assemblies. (b) Top view of a PM arrangement. Only four winding phases are represented.

The null-flux characteristic is obtained by ensuring that the flux linkage from the two members of a PM pair cancel each other when the rotor is centered. This is not the case when the rotor is off-centered, which yields the flux linkage gradient.

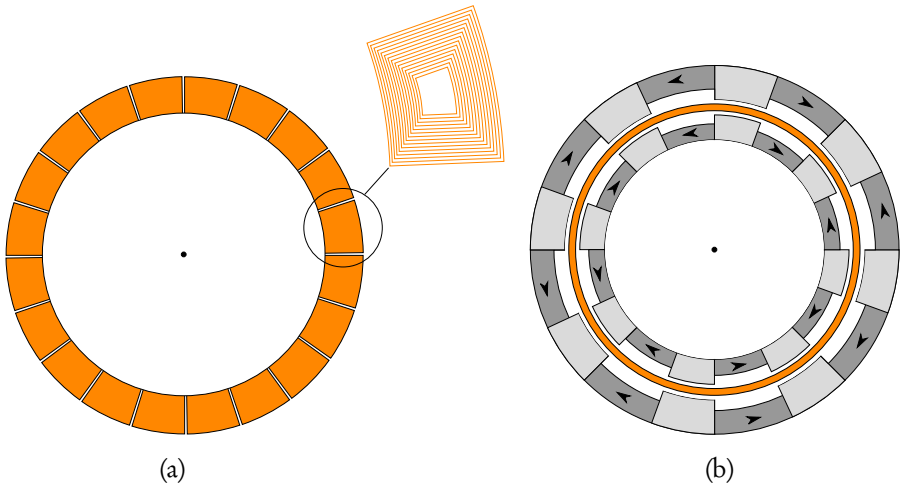

Fig. 2.8: (a) Bearing with improved stator winding from (Murakami et al., 1996), and detailed view of a printed sheet. (b) Bearing from (Basore, 1980).

(Murakami et al., 1996) presents an improved version of the previous bearing. The rotor remains identical but instead of short-circuited wires, the winding is made of a stack of conducting sheets where many thin coils are printed, see Fig. 2.8 (a).

2.1.4 Basore et al

(Basore, 1980) proposes a bearing with a bulk conducting rotor as depicted in Fig. 2.8 (b). The null-flux characteristic is obtained by ensuring that the PM field direction is parallel to the speed of the conductor. In this aim, the magnets are arranged so that the PM field is oriented in the azimuthal direction within the conductor when it is centered. This cannot be satisfied entirely and therefore the bearing is only partially null-flux. It also requires a thin conductor.

When the rotor is off-centered, the flux gradient arises as the conductor experiences radial PM field lines and thus higher flux linkage variations.

2.1.5 Pinkerton et al

In this section, all the bearings have the null-flux characteristic, and the flux linkage gradient is readily apparent.

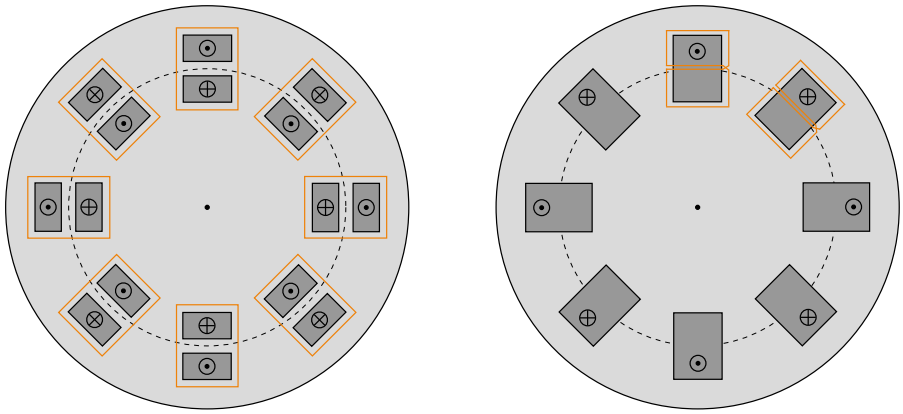

(a) (b)

Fig. 2.9: Bearings patented by Pinkerton (1994). (a) Each phase interacts with two PM poles. (b) Each phase has an eight figure shape and interacts with a single PM pole.

(Pinkerton, 1994) is a patent covering three bearings with axial magnetic field. The first bearing is shown in Fig. 2.9 (a). It is similar to the one shown in Fig. 2.7, except that it may include only one of the PM assemblies.

The second bearing is shown in Fig. 2.9 (b). It is similar to the first one, except that the loops have the shape of an eight figure and interact with a single PM pole.

The third bearing is shown in Fig. 2.10 (a). Each phase includes conducting loops that are symmetrically disposed around the winding center and interact with a single PM pole. The two loops of a phase are connected in order to obtain the null-flux characteristic.

In the three previous bearings, the PMs can either be on the rotor or on the stator. Furthermore, either one or two PM assemblies may be used. In the case of two assemblies, they are facing each other in attracting mode as in Fig. 2.7 (a).

(Clifton et al., 1995) covers the bearing shown in Fig. 2.10 (b). This is an improved version of the bearing from Fig. 2.9 (a). The improvement consists in connecting the loops that are symmetrically disposed around the winding center in order to have the null-flux characteristic even when the rotor expands radially due to centrifugal effects at high speeds.

(Andrews and Pinkerton, 1996) combines two of the bearings presented in (Clifton et al., 1995). The bearings are spaced from each other along the axis, and angularly shifted with respect to each other to smooth the pulsating restoring forces on the rotor.

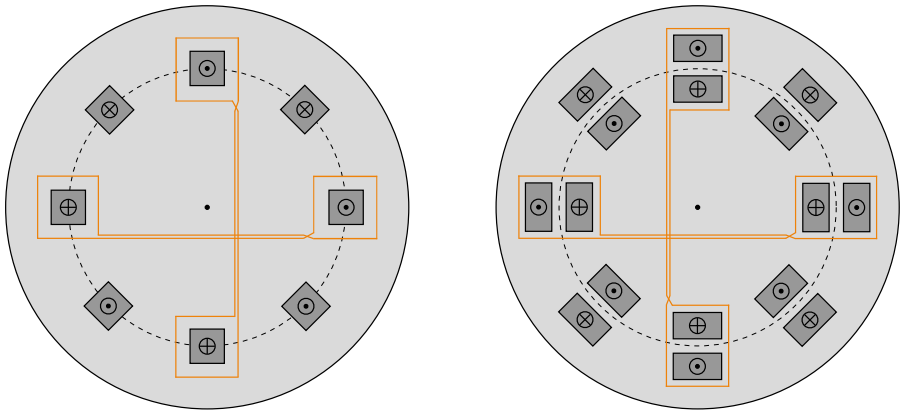

(a) (b)

Fig. 2.10: (a) Bearing patented by Pinkerton (1994) in the case of a PM part including four pole pairs and a winding part with two phases. (b) Improved bearing version from (Clifton et al., 1995) with interconnected loops.

2.1.6 Danby

(Danby, 1971) covers a bearing comprising PMs that can either be on the rotor or on the stator. They are always external and create a magnetic field with two or more pole pairs. The winding is made of a pair of short-circuited phases that are angularly spaced by a pole pitch of the PM field. The number of pole pairs of a phase is equal to the number of pole pairs of the PMs minus one. Each phase links a non-zero PM flux only when the rotor is off-centered. The case of a bearing comprising PMs creating a magnetic field with two pole pairs and a single phase with one pole pair is shown in Fig. 2.11 (a).

2.1.7 Davey et al

(Davey, 1996) covers a bearing with winding phases that guide a rotating shaft in both the radial and axial directions. The operating principle of the radial guiding is the same as that of Fig. 2.9 (b).

(Davey et al., 2005) includes the description of a bearing where the radial support function is similar to that of Fig. 2.9 (a), except that the PMs on the rotor interact with two identical stationary coils assemblies lying on both its sides as shown in Fig. 2.11 (b).

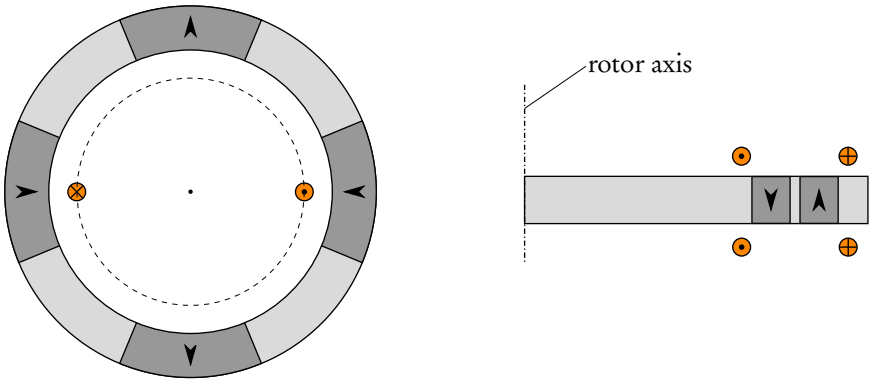

Fig. 2.11: (a) Bearing patented by Danby (1971). (b) Bearing proposed by Davey et al. (2005), where each phase is made up of two identical null-flux coils lying on both sides of the PMs. Only one phase is represented.

2.1.8 New topologies

This section introduces new topologies of null-flux, heteropolar EDBs that are patented in (Dehez et al., 2015). These bearings have axial or radial magnetic field, examples of which are shown in Fig. 2.12.

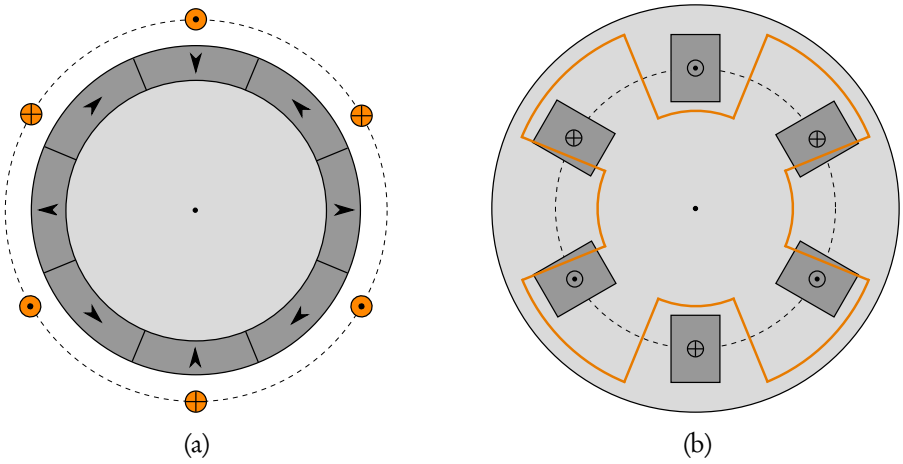

Fig. 2.12: Null-flux heteropolar bearings. (a) Radial PM field version with $p = 2$ and $q = 3$. (b) Axial PM field version with $p = 3$ and $q = 4$. Only one phase is shown.

These bearings are composed of PM and winding parts rotating with respect to each other. Each part may comprise ferromagnetic material or not, and the PMs can either be on the rotor or on the stator. The number of pole pairs of the PMs and winding are p and q, respectively. They are linked through the identity $q = p \pm 1$

that is derived in chapter 3. Satisfying this identity ensures the the bearings have the null-flux characteristic, and that there is a flux linkage gradient and a restoring electrodynamic force on the rotor.

From the above general principles, different bearing topologies can be obtained, both for the winding and the PM parts. Such topologies with radial magnetic field are shown in Fig. 2.13. In the air-gap winding and slotted yoke topologies, the parts comprising the PMs and the winding can move relative to each other. In the bell-shaped topology, the yoke behind the winding and the part comprising the PMs are attached together and can move with respect to the winding. These topology of these bearings is similar to that of electromechanical converters, which would ease construction aspects.

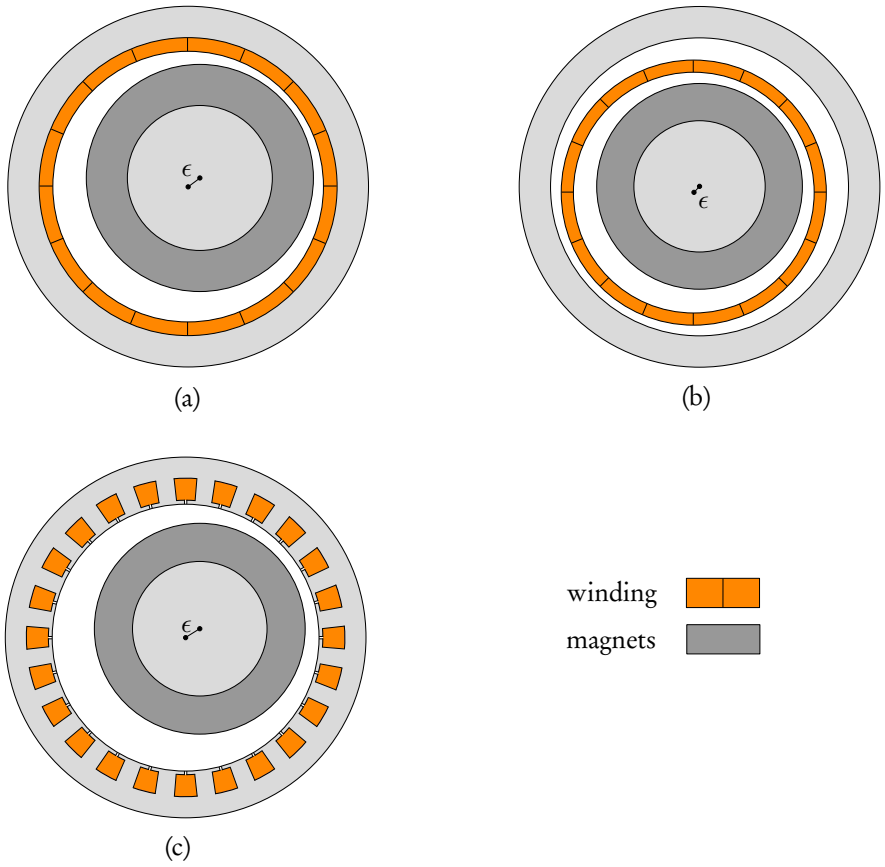

Fig. 2.13: Bearing topologies with radial PM field. (a) Air gap winding. (b) Bell-shaped. (c) Slotted yoke.

Besides, each of the bearing topologies from Fig. 2.13 can be implemented in different ways. The PMs can be on the rotor or on the stator, and the rotor can be

internal or external as shown in Fig. 2.14 in the case of the air gap winding topology.

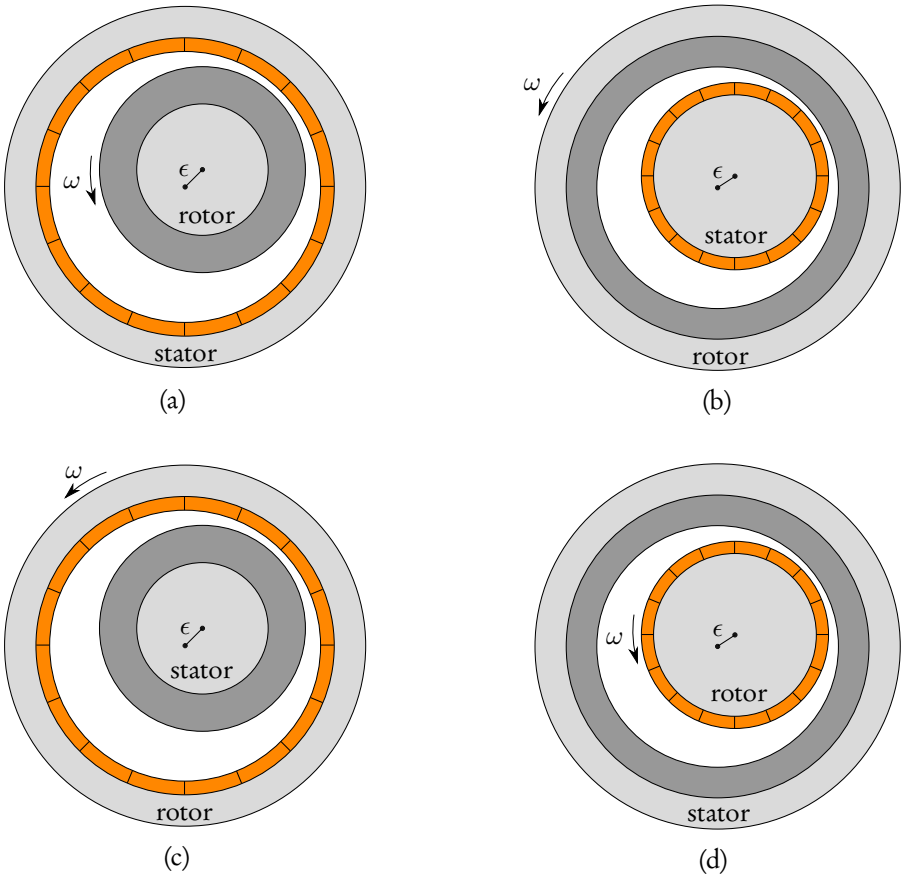

Fig. 2.14: Possible configurations for the bearing with the air gap winding topology. (a) Internal rotor with PMs. (b) External rotor with PMs. (c) External wound rotor. (d) Internal wound rotor.

Finally, other bearings with axial magnetic field can be obtained through a similar approach.

2.1.9 Conclusion

A wide variety of heteropolar EDBs have been proposed in the literature. Usually, the bearing design process goes as follows. A new bearing embodiment is proposed, and its proper operation is demonstrated by proposing a model predicting satisfactory forces on the rotor. In section 2.1.1, a more straightforward way to show the proper operation of a bearing is exposed. This consists in identifying the presence of a flux linkage gradient.

In the next chapters of this thesis, a reversed design approach is followed. A

model adapted to various magnetizations and winding geometries is first proposed. Then, design guidelines are derived by imposing constraints on the model i.e., the presence of the flux linkage gradient and of the null-flux characteristic. Then, new bearing topologies are derived from these guidelines. These new topologies were presented in section 2.1.8.

2.2 Models

Various models have been proposed to predict the performance of heteropolar EDBs. This section presents an overview of these models. Their derivation is briefly explained and the existing experimental validations are pointed out.

2.2.1 Modeling of EDBs

The performance of an EDB is usually predicted with a lumped-parameter electromechanical model whose parameters are calculated using an electromagnetic field model, as shown in Fig. 2.15.

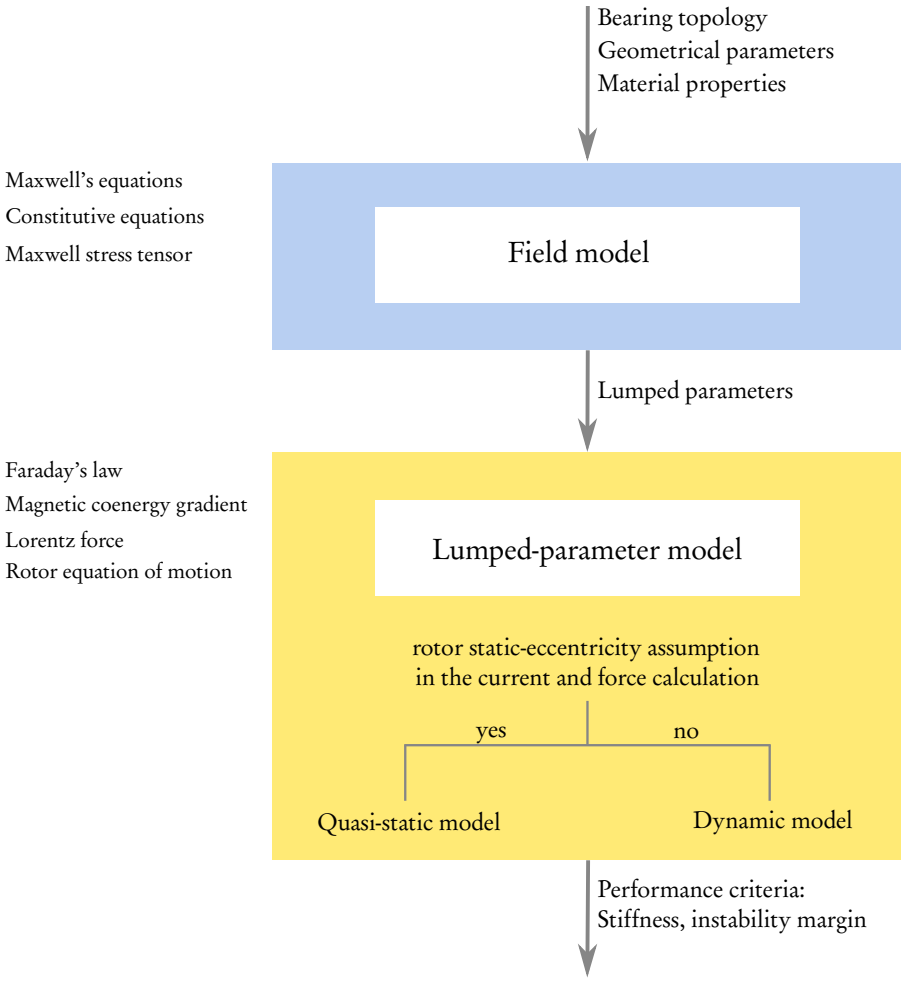

Fig. 2.15: Electromechanical models of EDBs. The parameters of the lumped-parameter model are calculated through a field model. Most of the contributions of this work to the modeling regard electromagnetic lumped-parameter models.

The field model solves Maxwell's equations and the constitutive equations of the materials numerically or analytically. This yields the field distributions in the bearing and the lumped parameters such as the winding resistance and inductances.

These parameters are the input of a lumped-parameter model that solves the winding equivalent circuit for the currents through Faraday's law. Then, the forces are obtained using Lorentz's formula, or by calculating the magnetic coenergy gradient. Finally, the rotor motion is predicted by coupling these forces with a mechanical model of the rotor.

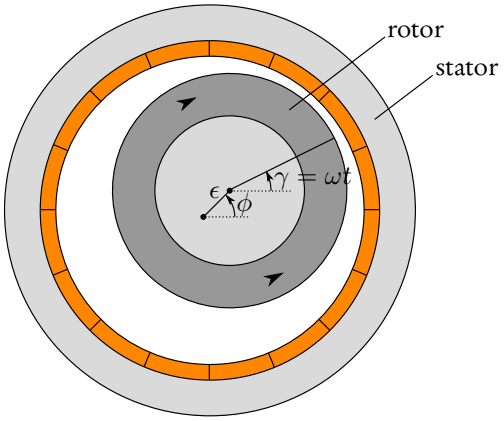

Fig. 2.16: Mechanical variables of a bearing with two degrees of freedom.

The lumped-parameter model is described as quasi-static or dynamic, depending on whether the rotor is assumed to spin in a fixed position or not when calculating the currents and forces. This is referred to as the static-eccentricity assumption. More specifically, the rotor position is described with three variables that are the spin angle γ, the whirl angle ϕ, and the eccentricity ϵ, as shown in Fig. 2.16. The static-eccentricity assumption means that when calculating the induced currents in the winding phases, the contributions to the electromotive force that are associated with the time variation of ϕ and ϵ are neglected compared to the contributions that are associated with the time variation of γ. As a result, Faraday's law applied to one short-circuited phase yields[1]:

$$0 = RI + L_c \frac{dI}{dt} + \frac{d\Phi}{dt}, \tag{2.2}$$

where the electromotive force term is:

[1] R is the phase resistance, L_c is the winding cyclic inductance, I is the phase current, and Φ is the permanent magnet flux linkage in the phase.

$$\begin{aligned}\frac{d\Phi}{dt} &= \frac{\partial\Phi_i}{\partial\gamma}\frac{d\gamma}{dt} + \frac{\partial\Phi_i}{\partial\phi}\frac{d\phi}{dt} + \frac{\partial\Phi_i}{\partial\epsilon}\frac{d\epsilon}{dt} \\ &\cong \frac{\partial\Phi_i}{\partial\gamma}\omega.\end{aligned} \tag{2.3}$$

The static-eccentricity assumption therefore limits the scope of the quasi-static models as the accuracy of the current and force predictions depends on the rotor motion. This is not the case for the dynamic models. In any case, the forces are coupled to a rotor mechanical model that is not impacted by the static-eccentricity assumption. Therefore, this assumption does not prevent the prediction of the rotor dynamics.

2.2.2 Quasi-static models

Most of the existing models assume the static eccentricity of the rotor and thus predict the forces on the rotor spinning in a fixed off-centered position. These models can either be numerical or analytical. Numerical models compute the forces on the rotor using the finite element method or the boundary element method, whereas analytical models are derived following these steps:

1. the PM field distribution is calculated in the conductor region;
2. it is integrated on the surface area of the winding phases, yielding the flux linkage as a function of the rotor position;
3. the induced electromotive force is obtained by deriving the flux linkage with respect to time. The phase currents are then calculated by modeling each phase as an R-L equivalent circuit;
4. the total force is finally obtained by integrating for the Lorentz force along the conductors, or by calculating the magnetic coenergy gradient.

Davey (1997) proposes an analytical model to predict the interaction forces between PMs and null-flux coils arranged as in Fig. 2.9 (a) and (b). The rotor force is calculated in the time and Fourier domains, in the aim of obtaining the optimal relative size of the coils compared to the PMs. However, the model neglects the curvature of the bearing geometry. The PMs and phases thus have straight shapes and move following a rectilinear path, which is a poor approximation of the actual paths of the bearing's rotating elements. Lastly, the model predictions are not validated.

Davey (2003) proposes four models combining the analytical approach with the boundary element method. They predict the interaction forces between PMs and

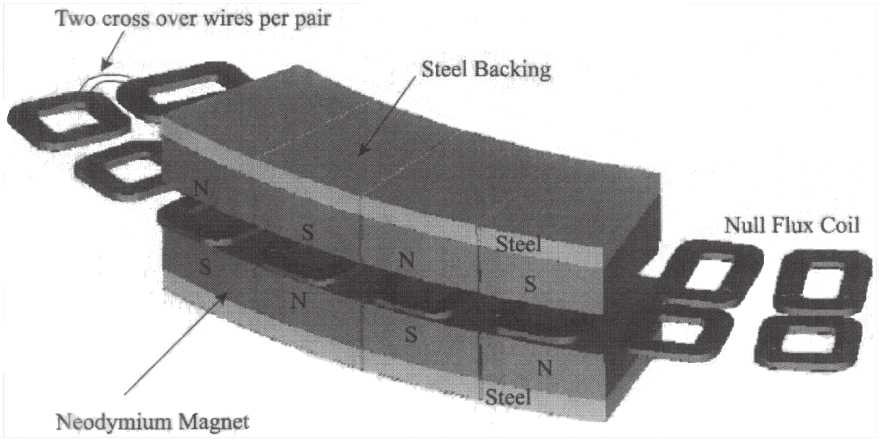

Fig. 2.17: Experimental apparatus presented in (Davey, 2003).

null-flux coils arranged as in Figs. 2.9 (b). Again, the curvature of the bearing geometry is not taken into account as these models are primarily aimed at studying a maglev system.

A prototype was built to validate the predictions of the three models. It includes a rotor with 45 null-flux coils that spins between two PM assemblies on the stator, as shown in Fig. 2.17. Each rotor coil is made of 208 wire turns. The stator assemblies comprise 4 PMs each and are attached in attracting mode. In the experimental tests, the force on the PM arrangement was measured for two different eccentricities.

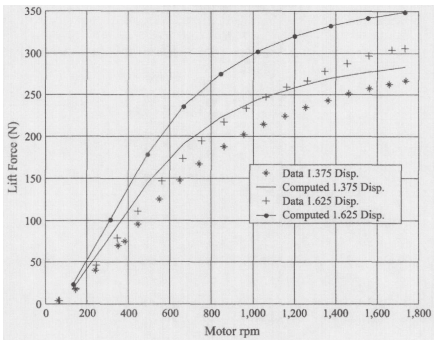

(a)

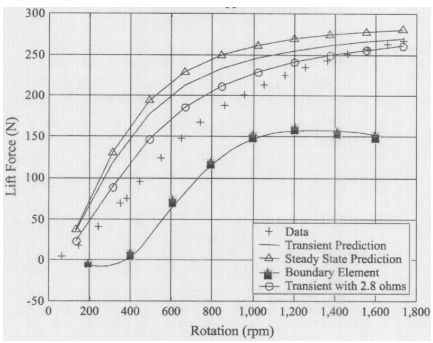

(b)

Fig. 2.18: Data from (Davey, 2003). (a) Experimental results vs two-dimensional boundary element code predictions. (b) Experimental results vs the predictions of the three-dimensional boundary element method, the transient analytical model, the steady-state analytical model, and the transient model with increased phase resistance.

The first model is two dimensional and based on the boundary element method.

Its predictions exceed the experimental results as shown in Fig. 2.18 (a). The authors attribute this difference to the fact that the end region fields are neglected.

The second model is three dimensional and also based on the boundary element method. It is referred to as 'Boundary Element' in Fig. 2.18 (b). It yields bad results that are attributed to the poor geometrical approximation of the conductors that link the two parts of each coil.

The third and fourth models are analytical, one steady-state and the other transient. As opposed to the transient model, the steady-state model neglects the field entry effects i.e., the electrical transient associated with the entry of the rotor coils in the volume between the two PM assemblies spanning over less than 360^o, see Fig. 2.17. In these two models, the PM flux in the coils is computed through a three dimensional static code. All the results are shown in Fig. 2.18 (b). Finally, a last prediction was made after increasing the phase resistance from 2.2 to 2.8 ohms to take the heating of the coil into account.

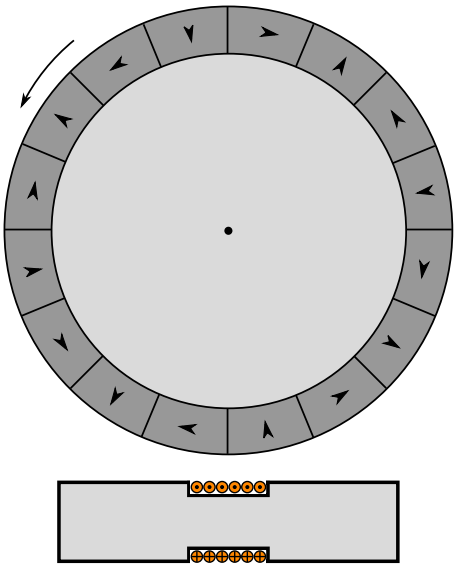

Fig. 2.19: Arrangement of the experimental parts for the tests in (Eichenberg et al., 2006).

Eichenberg et al. (2006) proposes an analytical model for the bearing shown in Fig. 2.6 (b). This model is validated through FE analysis and experimental tests, considering a rotor and a single winding phase. The rotor comprising a Halbach array of PMs spins at a fixed position in front of the winding phase (Fig. 2.19), while the open-circuit voltage, the short-circuit currents and the force on the rotor are measured. The experimental rotor and stator parts are shown in Fig. 2.20 (a) and (b), respectively. Four different phases are tested, with different number of turns

and conductor diameters. The experimental results agree well with the model predictions, except at high rotational speeds. In this case, the rise in temperature and the skin effect affect the phase resistance that is assumed to be constant in the model.

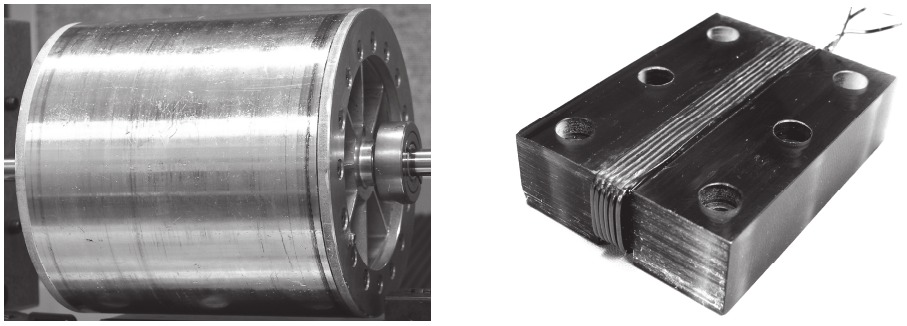

(a) (b)

Fig. 2.20: Experimental parts of Eichenberg et al. (2006). (a) Halbach array rotor. (b) Stator phase wound around a non-ferromagnetic core.

(Post and Ruytov, 1998) includes an analytical model for the bearings shown in Figs. 2.3 (b) and 2.6 (b). Few details of the model derivation are provided, but the final expressions of the bearing stiffness as a function of the spin speed are presented. In the case of the bearing from Fig. 2.3 (b), an experimental validation is given in (Bender and Post, 2000).

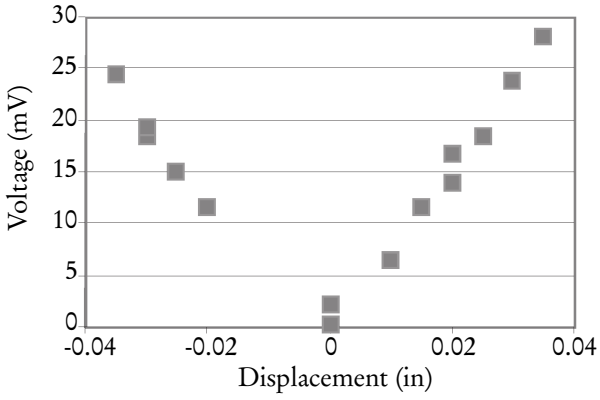

(a) (b)

Fig. 2.21: Experimental apparatus and measurements from Bender and Post (2000). (a) Stator winding part. (b) Peak to peak open-circuit voltage at 600 rpm.

The experimental apparatus includes an external Halbach array rotor and an internal stator with diametrically wound loops of Litz wire which is shown in Fig. 2.21 (a). The open-circuit voltage was measured, yielding the results shown in Fig. 2.21 (b). As stated by the authors, the experimental results agree well with the model

predictions from a qualitative point of view. No voltage is induced when the rotor is centered, and the voltage increases linearly with the eccentricity. However, the induced voltage exceeds the theoretical predictions by 40%. According to the authors, this may come from an error in the measurement of the parameters of the Halbach array. The current was also measured. The conclusion of the authors is that "The voltage and current measurements which have been performed are consistent with a radial stiffness of about 260 kN/m".

(Murakami, 1995; Murakami et al., 1996) include no model but experimental results providing qualitative insights on the difficulty of modeling EDBs. The tests are performed on the bearings shown in Figs. 2.7 and 2.8 (a).

In the first experimental apparatus, the coils have a hexagonal shape made out of thin copper sheets as shown in Fig. 2.22 (a). They lie between the two rotor parts comprising the PMs as shown in Fig. 2.22 (b). The air gap width is 11 mm and the flux density is approximately 0.3 T. An assembly of 17 such coils are molded using resin to form a part of the coil disc on which the measurements are made. The resulting drag and restoring forces are shown in Fig. 2.23 (a).

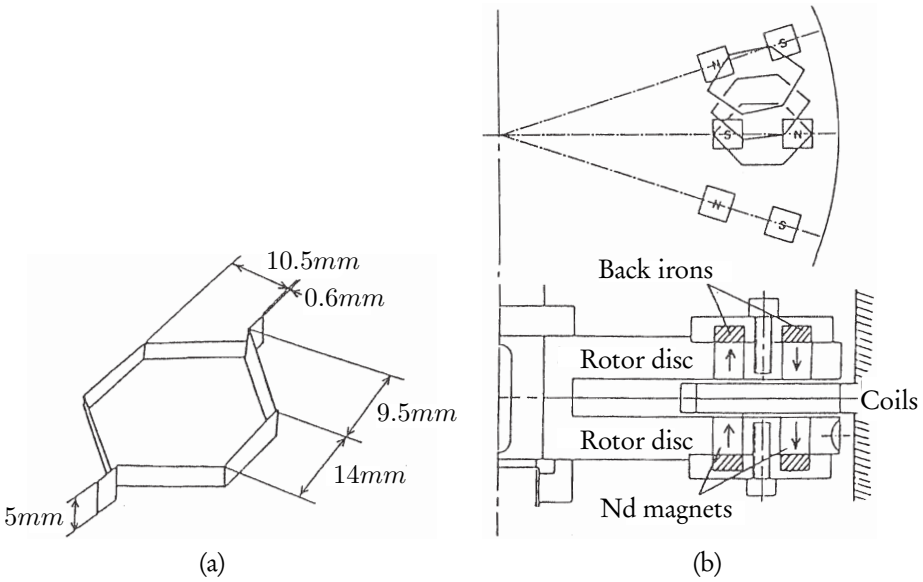

Fig. 2.22: Images from (Murakami et al., 1996). (a) Geometrical parameters of the null-flux coil with hexagonal shape. (b) Experimental set-up for the coils with hexagonal shapes.

The other models predict that, for small rotor eccentricities, the PM flux linkage and thus the induced voltage and current in the phase are proportional to the eccentricity. As a result, the Lorentz forces should be proportional to the eccentricity too. In the present case, the restoring force increases linearly with the eccentricity.

However, it does not reach $(0, 0)$ on the graph, which highlights the difficulty of predicting the null-flux equilibrium position for this bearing. The drag force should also be proportional to the eccentricity. However, the measurements are affected by the large eddy current losses in the coils, which is reflected in the high bias value of the drag force at zero eccentricity. This is confirmed by a second experiment with a rotor including 200 hexagonal coils: the maximum speed achieved by the rotor driven by an air turbine was about 1000 rpm, whereas the target speed of the authors was 3500 rpm.

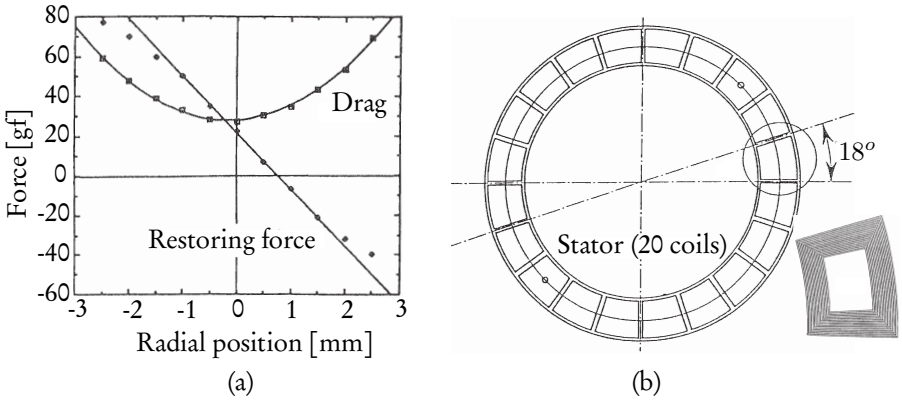

Fig. 2.23: Images from Murakami et al. (1996). (a) Restoring and drag forces as a function of the eccentricity for the prototype with 17 hexagonal coils. (b) Second stator with printed sheets of conductors.

The large eddy current losses motivated the construction of another stator with much thinner coils arranged as in Fig. 2.23 (b). The stator consists of a stack of 120 sheets with 20 coils printed on both sides. Using this stator, a rotational speed of 6000 rpm was reached.

Then, a levitation test was performed with the complete assembly shown in Fig. 2.24 (a). The assembly includes eddy current dampers aimed at stabilizing the unstable modes of the rotor. Levitation was hard to achieve and the authors explained it as follows: "Main difficulty was in low frequency translational mode. It appeared that as all coils are connected in a circle through neighboring mutual inductance, there might be some circular currents, which destabilize that mode. [...] two coils out of 20 coils in Fig. 2.23 (b), which face each other, were cut off in order to cut the circular current." The measured drag torques corresponding to the three stators are gathered in Fig. 2.24 (b). The losses corresponding to the printed stator with 18 of the 20 coils are much lower than the expected $18/20$ of the losses of the stator with 20 coils.

Finally, stable levitation was achieved with the stator comprising the 18 coils. For example, starting from the spin speeds of 5000 and 3000 rpm, the rotor levita-

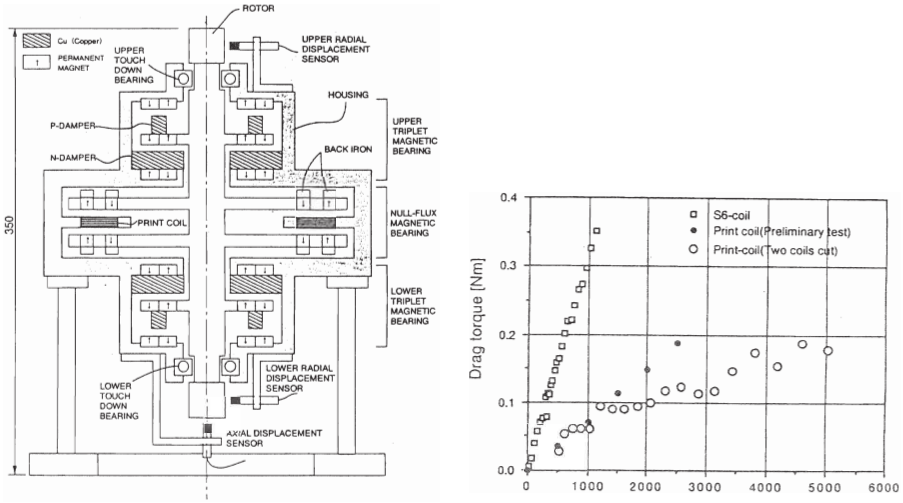

(a) (b)

Fig. 2.24: Images from Murakami et al. (1996). (a) Complete levitation test assembly. (b) Drag torque measurements for the three stators.

tion lasted for 60 and 12 seconds, respectively. Up to now, this is the only successful levitation test of a complete rotor supported by radial heteropolar EDBs that is reported in the literature.

Takanashi et al. (2006) presents results obtained using a three-dimensional FE model of the bearing shown in Fig. 2.5 (a). The forces are calculated after solving for the eddy current in the conductor rotating in a static eccentricity configuration.

2.2.3 Dynamic models

Detoni et al. (2012) introduces a lumped-parameter dynamic model predicting the force in homopolar and heteropolar EDBs. In the case of heteropolar EDBs, it is adapted to the embodiment patented by Post (1999) that is shown in Fig. 2.25.

The rotor is internal and includes two phases with diametrically opposed conductors, and no ferromagnetic parts. The stator is external and includes PMs with an even number of pole pairs. Embodiments with two and four PM pole pairs are shown in Fig. 2.25 (a) and (b), respectively.

The resulting model links the forces to the rotor displacements through a differential equation with four parameters. This equation is finally combined with a mechanical model of the rotor, yielding a linear state-space representation of the rotor dynamics. Remarkably, the effect of the speed of the rotor center on the electrical

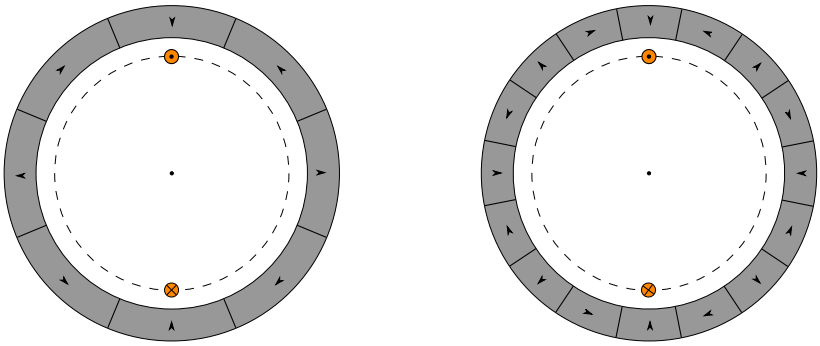

Fig. 2.25: Schematic view of the bearing patented by Post (1999). (a) PMs with two pole pairs. (b) PMs with four pole pairs. Only one phase is shown.

state variables is not neglected and the model is linear. This allows to study the bearing stability with conventional system analysis tools.

The model predicts the necessity of introducing additional damping in the system to achieve stability, for example non-rotating damping between the rotor and the stator. In this case, it also predicts that a stable rotor behaviour then occurs above a threshold speed. To validate the model, the predicted threshold speed is thus compared to that observed by Filatov and Maslen (2001) during experiments on a homopolar EDB. The close agreement between the predicted and the measured threshold speeds confirms the validity of the model.

2.2.4 Conclusion

Numerous quasi-static models have been proposed in the literature. In most cases, their accuracy is satisfactory. However, they are derived for a specific geometry. As a result, they cannot be used to compare various bearings. Furthermore, these models assume a static-eccentricity position of the rotor, which limits their use in the prediction of the dynamic behaviour and stability of the bearing.

Recently, a new dynamic model was derived that removes the static-eccentricity assumption, opening up new possibilities in terms of dynamic behaviour and stability predictions. Its scope includes many bearings. In the next section, this scope is further enlarged, allowing for the performance evaluation and the comparison of a wider range of bearings.

Quasi-static model

3

This chapter presents a quasi-static analytical model of EDBs based on the topologies introduced in section 2.1.8. Then, the model is analyzed and general guidelines for the design of null-flux heteropolar bearings are brought out by ensuring that the following conditions are met:

1. when the rotor is centered, no current is induced in the winding to lower the Joule losses;
2. when the rotor is off-centered, a current is induced and a centering electrodynamic force appears;
3. the centering force has a non-zero time average and a low pulsating component.

The content of this chapter is the subject of (Dumont et al., 2014b).

3.1 Parameters and variables

The design guidelines are obtained by considering a bearing consisting of:

- a rotor with surface mounted PMs producing a magnetic field with p pole pairs and harmonics with spatial periodicities np, n being odd;
- a stator comprising an air gap winding with q pole pairs and harmonics with periodicities mq, m being odd[1].

Nevertheless, the resulting guidelines can be generalized to the other topologies and configurations proposed in chapter 2.1.8.

[1] Considering n and m being odd implies that the magnetization and winding are symmetric, which corresponds to the vast majority of existing magnetization patterns and windings.

The radial dimensions of the bearing in the internal and external rotor cases are given in Fig. 3.1, and the active length is denoted H.

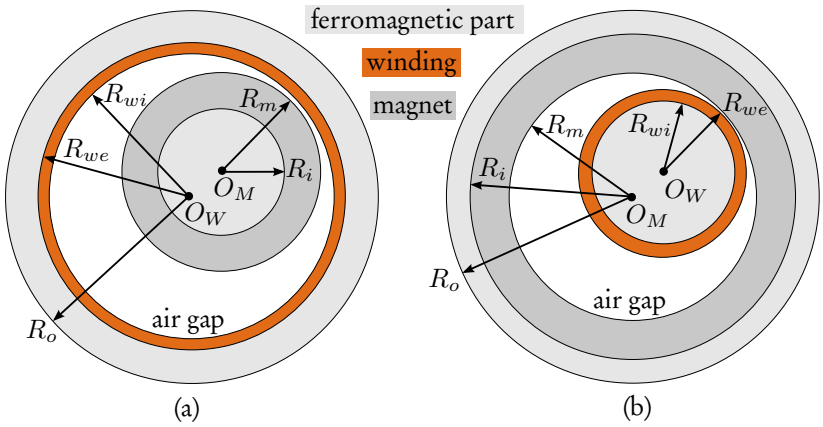

Fig. 3.1: Geometrical parameters in the internal (a) and external (b) rotor cases.

Figure 3.2 shows the coordinates and frames used in the next sections. A first frame is attached to the stator winding center O_W. A second frame is attached to the rotor PM center O_M. The position of the rotor center O_M is $(x = \epsilon\cos(\phi), y = \epsilon\sin(\phi))$ and the associated whirl speed is $\lambda = \frac{d\phi}{dt}$. The orientation of the rotor is given by the spin angle γ, and the associated spin speed is $\omega = \frac{d\gamma}{dt}$.

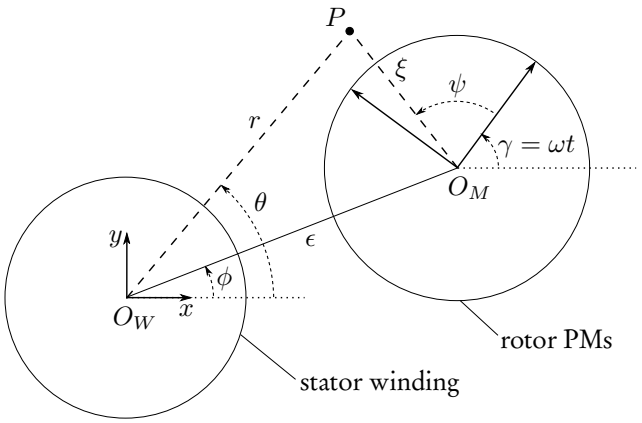

Fig. 3.2: Rotor and stator frames, and associated coordinates.

In the next sections, vectors are denoted using bold fonts. The transpose and time derivative of a given vector or matrix $\mathbf{A}$ are denoted $\mathbf{A}^T$ and $\dot{\mathbf{A}}$, respectively.

3.2 Assumptions

The model is derived under the following assumptions:

- only the two radial dimensions are considered;
- the materials have linear magnetic characteristics;
- the magnetic permeability of the ferromagnetic parts is infinite;
- the eddy currents are neglected except in the winding;
- the amplitude of the rotor eccentricity ϵ is small;
- when calculating the electromotive force, the effects of the rotor speed in the radial direction $\frac{d\epsilon}{dt}$ are neglected compared to those of the spin and whirl speeds ω and λ, respectively;
- the speeds ω and λ are constant;
- the bearing phases are identical and evenly distributed in the air gap.

As a result of these assumptions, the impact of the rotor eccentricity on the winding inductances is neglected, as well as the axial end-effects, the magnetic hysteresis and the saturation.

3.3 Modeling approach

The model presented in this chapter predicts the electromagnetic force on the rotor of the EDB. This force can be separated into two contributions, namely the detent and the electrodynamic forces.

To calculate these forces, a general expression of the vector potential $\mathbf{A}$ created by the magnets attached to an off-centered rotor is first presented (section 3.4). Assuming zero current, the Maxwell stress tensor is integrated in the air gap, yielding the detent force between the rotor magnets and the stator ferromagnetic yoke (section 3.5). In section 3.6, the permanent magnet flux linked by the k^{th} phase is evaluated by integrating the vector potential along the conductor:

$$\Phi_k = \oint \mathbf{A}^T \mathbf{dl}_k. \tag{3.1}$$

Using (3.1), the electrodynamic force due to the k^{th} phase can be calculated:

$$\mathbf{F}_k^e = [\nabla \Phi_k]\, I_k. \tag{3.2}$$

At this point, the phase current I_k is considered as arbitrary. From the analysis of (3.1) and (3.2), the conditions 1 and 2 stated at the beginning of this chapter are then translated into a practical guideline by establishing a link between the number of pole pairs of the permanent magnets and winding (section 3.8).

In section 3.9, this guideline is assumed to be met. The electromotive force and the currents induced in the winding of a bearing that has the null-flux characteristic can thus be calculated. The currents in the short-circuited phases are governed by:

$$0 = R_k I_k + \sum_{l=1}^{N} L_{kl} \frac{dI_l}{dt} + \frac{d\Phi_k}{dt}, \tag{3.3}$$

where R_k is the phase resistance and L_{kl} is the mutual inductance between phases k and l. Solving for the currents and substituting in (3.2), the total electrodynamic force on the rotor is obtained. The current-emf phase shift leading to the maximum mean force and the way to reduce pulsating forces are then discussed in order to meet condition 3. This results in another guideline regarding the number of winding phases (section 3.10). Lastly, section 3.11 shows some FE simulation results to validate the previous outcomes.

Finally, considering this approach and the equations (3.1)-(3.3), let us reformulate the conditions stated in the introductory part of this chapter. The first condition imposes a zero current when the rotor is centered. This current originates from the induced emf term $\frac{d\Phi_k}{dt}$ in (3.3). As the PM field is heteropolar, imposing a zero emf is equivalent to imposing a zero PM flux linked by the winding, hence the qualifier *null-flux*. Similarly, the second condition imposes a non-zero current when the rotor is centered, which translates into imposing a non-zero PM flux linked by the winding. As a consequence, the PM flux amplitude changes with the eccentricity. Therefore, $\nabla \Phi_k \neq 0$ in (3.2) and the electrodynamic force is non-zero too. In summary, the conditions stated at the beginning of this chapter become:

1. a zero PM flux when the rotor is centered;
2. a non-zero PM flux when the rotor is off-centered;
3. a non-zero time average and a low pulsating component of the centering electrodynamic force.

3.4 Permanent magnet field

The magnetic flux density created by an off-centered rotor was obtained by Rahideh and Korakianitis (2011) for various magnetization patterns. It is expressed in the rotor frame and was obtained assuming small rotor eccentricities. As the end effects are neglected, the magnetic field distribution is two-dimensional and only the axial component of the associated vector potential is non-zero. Using the vector potential definition $\mathbf{B} = \nabla \times \mathbf{A}$:

$$\begin{aligned} A_z^{rotor}(\xi,\psi) = \sum_{n,odd}^{\infty} \Big\{ & \left[K_{1n}\xi^{-np} + K_{2n}\xi^{np}\right] \sin\left(np\psi\right) \\ & + \epsilon \left[K_{3n}\xi^{np-1} + K_{4n}\xi^{-np+1}\right] \sin\left(\left(np-1\right)\psi - \gamma + \phi\right) \\ & + \epsilon \left[K_{5n}\xi^{np+1} + K_{6n}\xi^{-np-1}\right] \sin\left(\left(np+1\right)\psi + \gamma - \phi\right) \Big\}, \end{aligned} \tag{3.4}$$

where p is the number of PM pole pairs, and K_{1n},...,K_{6n} are constants depending on the geometry and magnetic properties of the bearing. Their detailed expressions are given in (Rahideh and Korakianitis, 2011). To ease the next calculation steps, the vector potential is re-expressed in the winding frame A_z through the following change of variables:

$$\begin{aligned} \psi &= \theta - \gamma + \sum_{n=1}^{\infty} \frac{1}{n} \left(\frac{\epsilon}{r}\right)^n \sin\left(n\left(\theta - \phi\right)\right) \\ \xi &= \sqrt{r^2 + \epsilon^2 - 2r\epsilon\cos\left(\theta - \phi\right)}. \end{aligned} \tag{3.5}$$

Keeping only the first order term in the Taylor series expansion of (3.5) at $\epsilon/r = 0$ yields:

$$\begin{aligned} \psi &= \theta - \gamma + \frac{\epsilon}{r}\sin\left(\theta - \phi\right) \\ \xi &= r - \epsilon\cos(\theta - \phi). \end{aligned} \tag{3.6}$$

Substituting (3.6) in (3.4), the Taylor series expansion of the vector potential in the winding frame A_z is obtained. In the vicinity of $\epsilon/r = 0$, the first-order terms of the series are:

$$\begin{aligned} A_z(r,\theta) = \sum_{n,odd}^{\infty} \Big\{ & C_n(r)\sin\left(np(\theta-\gamma)\right) \\ & + \epsilon\hat{C}_n(r)\sin\left((np+1)\,\theta - np\gamma - \phi\right) \\ & + \epsilon\check{C}_n(r)\sin\left((np-1)\,\theta - np\gamma + \phi\right) \Big\} \end{aligned} \tag{3.7}$$

where:

$$\begin{aligned} C_n(r) &= K_{1n}r^{-np} + K_{2n}r^{np} \\ \hat{C}_n(r) &= K_{1n}r^{-np-1}np + K_{5n}r^{np+1} + K_{6n}r^{-np-1} \\ \check{C}_n(r) &= -K_{2n}r^{np-1}np + K_{3n}r^{np-1} + K_{4n}r^{-np+1}. \end{aligned} \tag{3.8}$$

Let us analyze (3.7). The terms with C_n have $np\theta$-spatial periodicities. They do not depend on ϵ and correspond to the vector magnetic potential when the rotor is centered. The terms with $\epsilon\hat{C}_n$ and $\epsilon\check{C}_n$ have $(np \pm 1)\,\theta$-spatial periodicities, respectively. They are proportional to the center shift amplitude ϵ and only appear when the rotor is off-centered.

In the internal rotor case, the absence of ferromagnetic yoke on the armature results in $\check{C}_n = 0$. This means that for an internal rotor and no ferromagnetic armature yoke, only the terms with $(np+1)\theta$ periodicities remain. Similarly, in the external rotor case, the absence of ferromagnetic yoke results in $\hat{C}_n$ being zero. Then, only the terms with $(np-1)\theta$ periodicities remain.

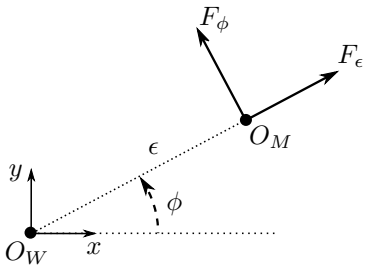

Fig. 3.3: The forces on the rotor are decomposed into two components that are parallel or perpendicular to the eccentricity.

3.5 Detent force

As the PM magnetic field distribution is known, the detent force between the rotor and the stator can be calculated by integrating the Maxwell stress tensor in the air gap. In the present case, the radial and azimuthal components of the tensor are:

$$\begin{aligned} dF_r^d(r,\theta) &= \frac{B_r^2(r,\theta) - B_\theta^2(r,\theta)}{2\mu_0} H r d\theta \\ dF_\theta^d(r,\theta) &= \frac{B_r(r,\theta) B_\theta(r,\theta)}{\mu_0} H r d\theta, \end{aligned} \tag{3.9}$$

where H is the active length of the bearing, and:

$$\mathbf{B} = \nabla \times \mathbf{A} \Rightarrow \begin{cases} B_r(r,\theta) = \dfrac{1}{r}\dfrac{\partial A_z(r,\theta)}{\partial r} \\ B_\theta(r,\theta) = -\dfrac{\partial A_z(r,\theta)}{\partial \theta}. \end{cases} \tag{3.10}$$

The detent force components are obtained through a transformation of variables:

$$\begin{bmatrix} dF_\epsilon^d \\ dF_\phi^d \end{bmatrix} = \begin{bmatrix} \cos(\theta-\phi) & -\sin(\theta-\phi) \\ \sin(\theta-\phi) & \cos(\theta-\phi) \end{bmatrix} \begin{bmatrix} dF_r^d \\ dF_\theta^d \end{bmatrix}, \tag{3.11}$$

where dF_ϵ^d and dF_ϕ^d are the forces in the direction of the off-centering and in the direction perpendicular to it, as shown in Fig. 3.3. Integrating (3.11) along a circle surrounding the rotor yields:

$$\begin{aligned} F_\epsilon^d &= \int_0^{2\pi} \left(\frac{B_r^2(r,\theta) - B_\theta^2(r,\theta)}{2\mu_0} \cos(\theta-\phi) \right. \\ &\qquad \left. - \frac{B_r(r,\theta) B_\theta(r,\theta)}{\mu_0} \sin(\theta-\phi) \right) H r d\theta \\ &= \epsilon \frac{2\pi H p}{\mu_0} \sum_{n,odd}^{\infty} \left\{ (p+1) K_{1n} K_{5n} + (p-1) K_{2n} K_{4n} \right\} \end{aligned} \tag{3.12}$$

$$\begin{aligned} F_\phi^d &= \int_0^{2\pi} \left(\frac{B_r^2(r,\theta) - B_\theta^2(r,\theta)}{2\mu_0} \sin(\theta-\phi) \right. \\ &\qquad \left. + \frac{B_r(r,\theta) B_\theta(r,\theta)}{\mu_0} \cos(\theta-\phi) \right) H r d\theta \\ &= 0. \end{aligned}$$

Under the assumption of small rotor eccentricities, it appears that the detent force is proportional to ϵ and aligned with the eccentricity, whatever the magnetization

pattern. This approximation is not so restrictive, although it requires a case-by-case validation for slotted topologies. As a result, the detent force is associated with a constant stiffness in the next chapters:

$$F_\epsilon^d = -K_d \epsilon, \tag{3.13}$$

where:

$$K_d = -\frac{2\pi H p}{\mu_0} \sum_{n,odd}^{\infty} \Big\{ (p+1) K_{1n} K_{5n} + (p-1) K_{2n} K_{4n} \Big\}. \tag{3.14}$$

Let us note that in (3.4), the constants K_{3n}, K_{4n}, K_{5n} and K_{6n} cancel if the ferromagnetic yoke is absent or attached to the same part as the PMs. As a consequence, $F_\epsilon^d = 0$ and there is no detent force in these cases, which is intuitive since the PMs do not stick to the yoke.

Finally, the detent force is well known in the field of electrical machines and commonly referred to as the unbalanced magnetic pull (Dorrell and Ionel, 2012; Rahideh and Korakianitis, 2011).

3.6 PM flux linkage

In order to consider a wide range of winding shapes, the geometry of each phase is described by a density of current stream lines vector $\mathbf{D_k}$ $[m^{-2}]$ defined as $\mathbf{J}_k = \mathbf{D}_k I_k$, where $\mathbf{J}_k [A/m^2]$ is the current density and $I_k [A]$ is the current amplitude. More details about the density of current stream lines can be found in appendix A. Using this definition, the PM flux (3.1) can be expressed as an integral over a volume comprising this phase:

$$\Phi_k = \int_V \mathbf{A}^T \mathbf{D}_k dv = \int_V A_z(r,\theta) D_{kz}(r,\theta,z) dv, \tag{3.15}$$

where D_{kz} is the axial component of the density of current stream lines vector. Defining the internal and external winding radii R_{wi} and R_{we}, and considering the volume $r \in [R_{wi}, R_{we}]$, $\theta \in [0, 2\pi]$ and $z \in [0, H]$, (3.15) becomes:

$$\Phi_k = \int_{R_{wi}}^{R_{we}} \int_0^{2\pi} A_z(r,\theta) \underbrace{\int_0^H D_{kz}(r,\theta,z) dz}_{=w_k(r,\theta)} r d\theta dr, \tag{3.16}$$

where $w_k(r,\theta)$ is a function that only depends on the geometry of the winding. It can be expanded into a Fourier series:

$$w_k(r,\theta) = \sum_{m,odd}^{\infty} W_m(r) \sin\left(mq\left(\theta - \delta_k\right)\right), \tag{3.17}$$

where δ_k is the angular position of the k^{th} winding phase, q is the winding pole pairs number and $W_m(r)$ is the amplitude of the m^{th} harmonic. As the winding phases are identical, $W_m(r)$ does not depend on k.

Let us illustrate this with examples. Fig. 3.4(a) and (b) show the developed views of a rhombic and a helical winding, respectively, in which the arrows give the direction of the vector $\mathbf{D}$. These two windings have the same w function given in Fig. 3.4(c). Therefore, they link the same magnetic flux created by a given rotor and yield the same force when carrying an identical current. Fig. 3.4(d) gives the coefficients W_m associated with the function w. They are non-zero only for odd values of m because of the winding symmetry. Similarly, the window frame windings in Fig. 3.5(a) and (b) have the same w function, see Fig. 3.5(c). Again, the associated coefficients W_m given in Fig. 3.5(d) are non-zero for odd values of m only[1].

Finally, substituting (3.7) in (3.16) yields:

$$\begin{aligned}\Phi_k = \sum_{n,odd}^{\infty}\sum_{m,odd}^{\infty}\int_{R_{wi}}^{R_{we}}\int_0^{2\pi}\Big(&C_n(r)\sin\left(np(\theta-\gamma)\right)\\ &+\epsilon\hat{C}_n(r)\sin\left(\left(np+1\right)\theta - np\gamma - \phi\right)\\ &+\epsilon\check{C}_n(r)\sin\left(\left(np-1\right)\theta - np\gamma + \phi\right)\Big)\\ &W_m(r)\sin\left(mq\left(\theta-\delta_k\right)\right)d\theta r dr.\end{aligned} \tag{3.18}$$

3.7 Electrodynamic force with arbitrary currents

The electrodynamic force on the rotor due to the presence of an arbitrary current in a single winding phase is calculated using (3.2) and (3.18). The force in the direction of the off-centering is:

[1]The function $w_k(r,\theta)$ can be further understood by considering that the wire is a filament located at a given radius R_w. Then, the function w_k depends only on θ and is worth $w(\theta) = \frac{dz}{R_w|d\theta|}$, i.e. the local derivative of the wire's axial position or height z with respect to the azimuthal distance. Considering that a non-zero m^{th} harmonic in the Fourier series of a function results in a non-zero m^{th} harmonic in the Fourier series of the derivative of this function, knowing z and analyzing the winding shape allows to identify the PM field harmonics that are linked by the winding in a straightforward way.

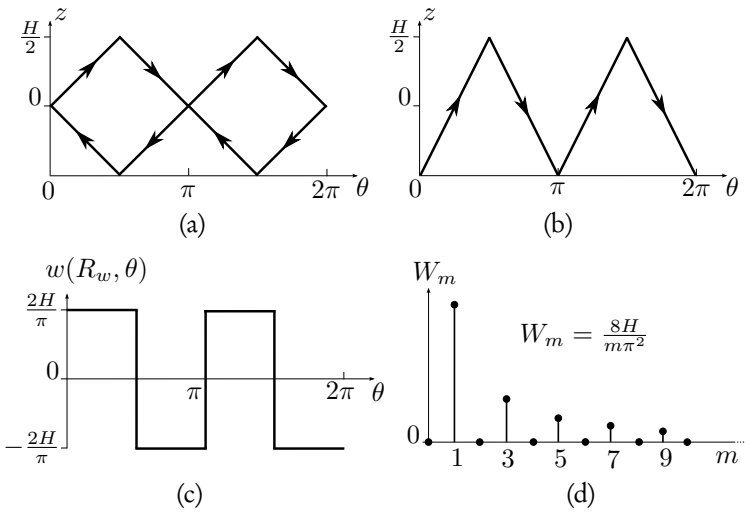

Fig. 3.4: Developed views of a rhombic winding (a) and a helical winding (b), with the associated function w (c) and coefficients W_m (d).

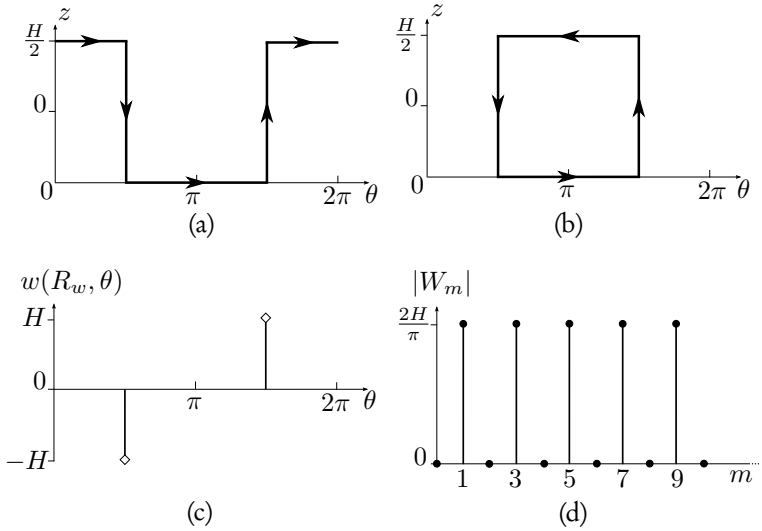

Fig. 3.5: Two window frame windings (a), (b) with different shapes but the same w function (c) and coefficients W_m (d).

$$
\begin{aligned}
F^e_{k\epsilon} &= \frac{\partial \Phi_k}{\partial \epsilon} I_k \\
&= I_k \sum_{n,odd}^{\infty} \sum_{m,odd}^{\infty} \int_{R_{wi}}^{R_{we}} \int_0^{2\pi} \Big(\hat{C}_n(r) \sin\left((np+1)\,\theta - np\gamma - \phi\right) \\
&\qquad + \check{C}_n(r) \sin\left((np-1)\,\theta - np\gamma + \phi\right) \Big) \\
&\qquad W_m(r) \sin\left(mq\,(\theta - \delta_k)\right) d\theta r dr,
\end{aligned}
\tag{3.19}
$$

whereas the force in the direction perpendicular to the off-centering is:

$$\begin{aligned} F^e_{k\phi} &= \frac{\partial \Phi_k}{\epsilon \partial \phi} I_k \\ &= I_k \sum_{n,odd}^{\infty} \sum_{m,odd}^{\infty} \int_{R_{wi}}^{R_{we}} \int_0^{2\pi} \Big(-\hat{C}_n(r) \cos\left((np+1)\,\theta - np\gamma - \phi\right) \\ &\qquad + \check{C}_n(r) \cos\left((np-1)\,\theta - np\gamma + \phi\right) \Big) \\ &\qquad W_m(r) \sin\left(mq\,(\theta - \delta_k)\right) d\theta r dr. \end{aligned} \tag{3.20}$$

3.8 Guidelines regarding the pole pairs numbers

This section aims at imposing constraints on the winding shape so that a bearing meets the conditions 1-2 for a suitable EDB i.e., no flux when the rotor is centered and a non-zero flux when the rotor is off-centered, see section 3.3. More specifically, this section focuses on finding the appropriate number of pole pairs q a winding should have when combined with a rotor with arbitrary number of pole pairs p in the aim of satisfying these conditions.

This section focuses on getting qualitative guidelines to choose an appropriate value for q without studying or optimizing the exact shape of the winding. Therefore, quantitative guidelines on how to choose the best winding shape through coefficients W_m, and on how to choose the best magnetic and geometrical properties of the bearing through C_n are not given here. For example, $C_n W_m$ is never assumed to be zero in this section to remain as general as possible.

3.8.1 Zero flux when centered

Let us apply the first condition for a null-flux bearing to (3.18). When centered, $\epsilon = 0$ and (3.18) becomes:

$$\begin{aligned} \Phi_k = \sum_{n,odd}^{\infty} \sum_{m,odd}^{\infty} & \int_{R_{wi}}^{R_{we}} C_n(r) W_m(r) r dr \\ & \underbrace{\cdot \int_0^{2\pi} \sin\left(np(\theta-\gamma)\right) \sin\left(mq\,(\theta - \delta_k)\right) d\theta.}_{\begin{cases} = 0 & mq \neq np \\ = \pi \cos\left(mq\gamma - mq\delta_k\right) & mq = np \end{cases}} \end{aligned} \tag{3.21}$$

It follows that for a rotor and a winding with p and q pole-pairs, respectively, $mq \neq np$ must be true for every couple (m, n). In this case, (3.21) cancels and there

is no flux in any phase when the bearing is centered. The electrodynamic bearing is null-flux.

3.8.2 Non-zero flux when off-centered

The second condition for a suitable electrodynamic bearing implies that one of the terms proportional to ϵ induces an emf in the winding when $\epsilon \neq 0$. Let us have a look at the terms with $(np+1)\theta$-periodicities in (3.18):

$$\begin{aligned}
&\sum_{n,odd}^{\infty}\sum_{m,odd}^{\infty}\epsilon\int_{R_{wi}}^{R_{we}}\hat{C}_n(r)W_m(r)rdr \\
&\underbrace{.\int_0^{2\pi}\sin\left((np+1)\,\theta-np\gamma-\phi\right)\sin\left(mq\,(\theta-\delta_k)\right)d\theta.}_{\begin{array}{ll}=0 & mq\neq np+1\\ =\pi\cos\left((mq-1)\gamma-mq\delta_k+\phi\right) & mq=np+1\end{array}}
\end{aligned} \tag{3.22}$$

When the rotor is off-centered, there is a net magnetic flux in the winding if this contribution does not cancel i.e. if $mq = np+1$ for at least one couple (m,n). Similarly, the term from (3.18) which is proportional to ϵ and periodic in $(np-1)\theta$ becomes:

$$\begin{aligned}
&\sum_{n,odd}^{\infty}\sum_{m,odd}^{\infty}\epsilon\int_{R_{wi}}^{R_{we}}\check{C}_n(r)W_m(r)rdr \\
&\underbrace{.\int_0^{2\pi}\sin\left((np-1)\,\theta-np\gamma+\phi\right)\sin\left(mq\,(\theta-\delta_k)\right)d\theta.}_{\begin{array}{ll}=0 & mq\neq np-1\\ =\pi\cos\left((mq+1)\gamma-mq\delta_k-\phi\right) & mq=np-1\end{array}}
\end{aligned} \tag{3.23}$$

In this case, having a non-zero magnetic flux in the winding when the rotor is off-centered translates into satisfying the identity $mq = np-1$ for at least one couple (m,n).

In conclusion, satisfying either the identity $mq = np+1$ or $mq = np-1$ ensures that a non-zero flux is linked by the winding when the rotor is off-centered. Furthermore, the flux is proportional to the displacement ϵ.

3.8.3 Non-zero force when off-centered

When a non-zero current flows in phase k, the presence of a restoring force $F^e_{k\epsilon}$ requires that $\frac{\partial\Phi_k}{\partial\epsilon} \neq 0$. In this aim, let us analyze the contributions of the terms

with $(np \pm 1)\,\theta$-periodicities in (3.19):

$$\begin{aligned}
&I_k \sum_{n,odd}^{\infty} \sum_{m,odd}^{\infty} \int_{R_{wi}}^{R_{we}} \hat{C}_n(r) W_m(r) r dr \\
&\underbrace{. \int_0^{2\pi} \sin\left((np+1)\,\theta - np\gamma - \phi\right) \sin\left(mq\,(\theta - \delta_k)\right) d\theta} \\
&\quad = 0 \qquad\qquad\qquad\qquad mq \neq np+1. \\
&\quad = \pi \cos\left((mq-1)\gamma + \phi - mq\delta_k\right) \quad mq = np+1.
\end{aligned} \tag{3.24}$$

$$\begin{aligned}
&I_k \sum_{n,odd}^{\infty} \sum_{m,odd}^{\infty} \int_{R_{wi}}^{R_{we}} \check{C}_n(r) W_m(r) r dr \\
&\underbrace{. \int_0^{2\pi} \sin\left((np-1)\,\theta - np\gamma + \phi\right) \sin\left(mq\,(\theta - \delta_k)\right) d\theta} \\
&\quad = 0 \qquad\qquad\qquad\qquad mq \neq np-1. \\
&\quad = \pi \cos\left((mq+1)\gamma - \phi - mq\delta_k\right) \quad mq = np-1.
\end{aligned}$$

It appears that the identities to satisfy for having a non-zero force $F^e_{k\epsilon}$ are thus identical to the ones ensuring that a non-zero flux is linked by the winding phase when the rotor is off-centered. This was expected, considering the last comments from section 3.3. Note that making the same developments for $F^e_{k\phi}$ yields the same results.

Finally, the above constraints on the winding geometry to create a centering force was derived without making any assumption on the current amplitude and phase. Therefore, it can also be applied to active bearings based on electrodynamic forces, which is consistent with Silber et al. (2012).

3.8.4 Summary

In order to have a non-zero PM flux (and thus an induced emf and an electrodynamic force) when the rotor is off-centered, the number of pole pairs p and q must be such that either $mq = np + 1$ or $mq = np - 1$ is true for at least one couple (m, n). The harmonics numbers m and n being odd integers only, one of these two identities being verified implies that q and p necessarily have different parities. If one is odd, the other is even and vice-versa. It is interesting to note that q and p having different parities induces that the first identity for a null-flux bearing $mq \neq np$ is true whatever the odd values n and m may take. In other words, when restricted to windings and magnetizations with odd harmonics n and m, which is usually the case, having an

induced emf and a non-zero electrodynamic force always implies that the bearing is null-flux.

In conclusion, the two first identities for a suitable bearing thus reduce to choosing the pole pairs numbers q and p such that either:

$$mq = np + 1 \tag{3.25}$$

or:

$$mq = np - 1 \tag{3.26}$$

is true for at least one couple (m, n). In this case, $mq \neq np$ for all the couples (m, n) and the bearing is null-flux, in addition to having an induced emf and force when off-centered. As a result, the constraint for obtaining a null-flux EDB is simple to meet even though the magnetization and winding may have many harmonics.

Two examples of electrodynamic bearings respecting the previous identities are given in Fig. 3.6. In Fig. 3.6 (a), the electrodynamic bearing has an internal rotor and the identity $mq = np + 1$ is satisfied, at least for $m = n = 1$. In Fig. 3.6 (b), the rotor is external and the identity $mq = np - 1$ is satisfied, at least for $m = n = 1$.

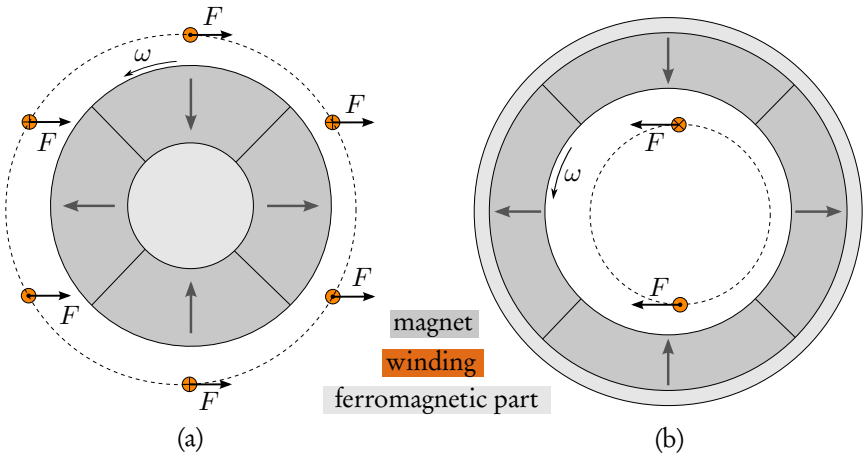

Fig. 3.6: Examples of null-flux electrodynamic bearings. (a) Internal rotor case with $p = 2$, $q = 3$. (b) External rotor case with $p = 2$, $q = 1$.

3.9 Electrodynamic force with induced currents

In this section, the guidelines regarding the pole pairs numbers (3.25) or (3.26) are assumed to be met. The bearing under study thus has the null-flux characteristic. This allows to calculate the current induced in the short-circuited phases and the associated electrodynamic force.

First, let us calculate the emf in the winding phases. As a consequence of the assumptions from section 3.2, the radial off-centering ϵ and the speeds ω and λ are considered as constants[1]. Summing the contributions (3.22) and (3.23) to the PM flux yields:

$$\begin{aligned}\Phi_k = \sum_{m,odd}^{\infty} \Big\{ & \epsilon \hat{H}_m \cos\left((mq-1)\gamma - mq\delta_k + \phi\right) \\ & + \epsilon \check{H}_m \cos\left((mq+1)\gamma - mq\delta_k - \phi\right) \Big\}\end{aligned} \tag{3.27}$$

with:

$$\begin{aligned}\hat{H}_m &= 0 && mq \neq np+1 \\ &= \pi \int_{R_{wi}}^{R_{we}} \hat{C}_n(r) W_m(r) r dr && mq = np+1 \\ \check{H}_m &= 0 && mq \neq np-1 \\ &= \pi \int_{R_{wi}}^{R_{we}} \check{C}_n(r) W_m(r) r dr && mq = np-1.\end{aligned} \tag{3.28}$$

The emf in phase k can then be derived as follows:

$$\begin{aligned}emf_k &= -\frac{d\Phi_k}{dt} = -\frac{\partial \Phi_k}{\partial \gamma}\omega - \frac{\partial \Phi_k}{\partial \phi}\lambda \\ &= \sum_{m,odd}^{\infty} \Big\{ \epsilon \hat{H}_m \left((mq-1)\omega + \lambda\right) \sin\left((mq-1)\gamma - mq\delta_k + \phi\right) \\ &\quad + \epsilon \check{H}_m \left((mq+1)\omega - \lambda\right) \sin\left((mq+1)\gamma - mq\delta_k - \phi\right) \Big\}.\end{aligned} \tag{3.29}$$

From (3.29) and (3.3), the general expression of the current in the k^{th} phase is obtained:

$$\begin{aligned}I_k = \sum_{m,odd}^{\infty} \Big\{ & \hat{I}_m \sin\left((mq-1)\gamma - mq\delta_k + \phi - \hat{\varphi}_m\right) \\ & + \check{I}_m \sin\left((mq+1)\gamma - mq\delta_k - \phi - \check{\varphi}_m\right) \Big\}.\end{aligned} \tag{3.30}$$

[1] This corresponds to neglecting the mechanical time constant associated with the rotor motion compared with the electrical time constant of the winding

The constants and the current phases with respect to the emf are:

$$\begin{aligned}
\hat{I}_m &= \frac{\epsilon \hat{H}_m \left((mq-1)\omega+\lambda\right)}{\sqrt{\left((mq-1)\omega+\lambda\right)^2 L_c^2 + R^2}} \\
\check{I}_m &= \frac{\epsilon \check{H}_m \left((mq+1)\omega-\lambda\right)}{\sqrt{\left((mq+1)\omega+\lambda\right)^2 L_c^2 + R^2}} \\
\hat{\varphi}_m &= \arctan\left(\frac{\left((mq-1)\omega+\lambda\right)L_c}{R}\right) \\
\check{\varphi}_m &= \arctan\left(\frac{\left((mq+1)\omega-\lambda\right)L_c}{R}\right),
\end{aligned} \tag{3.31}$$

where L_c is the cyclic inductance of the winding. Summing the contributions (3.24) to the centering electrodynamic force yields:

$$\begin{aligned}
F_{k\epsilon}^e = I_k \sum_{l,odd}^{\infty} \Big\{ & \hat{H}_l \cos\left((lq-1)\gamma + \phi - lq\delta_k\right) \\
& + \check{H}_l \cos\left((lq+1)\gamma - \phi - lq\delta_k\right) \Big\},
\end{aligned} \tag{3.32}$$

where the constants are given in (3.28). Considering that $\gamma = \omega t$, $\phi = \lambda t$, and substituting the current (3.30) in (3.32):

$$\begin{aligned}
F_{k\epsilon}^e = \sum_{m,odd}^{\infty} \sum_{l,odd}^{\infty} \Bigg(& \hat{I}_m \sin\Big(\left((mq-1)\omega+\lambda\right)t - mq\delta_k - \hat{\varphi}_m \Big) \\
& + \check{I}_m \sin\left(\left((mq+1)\omega-\lambda\right)t - mq\delta_k - \check{\varphi}_m\right) \Bigg) \\
& \Big(\hat{H}_l \cos\left(\left((lq-1)\omega+\lambda\right)t - lq\delta_k\right) \\
& + \check{H}_l \cos\left(\left((lq+1)\omega-\lambda\right)t - lq\delta_k\right) \Big).
\end{aligned} \tag{3.33}$$

3.10 Guidelines regarding the phase number

This section deals with the last condition from section 3.3 concerning the time average and pulsating component of the electrodynamic force. Considering (3.33), it discusses the current-emf phase shift yielding the maximum time average force $\bar{F}_{k\epsilon}$, and the impact of the number of phases on the pulsating forces. The results are then compared to existing predictions in the literature.

3.10.1 Time average of the force

Re-using (3.33), the mean force $\bar{F}_{k\epsilon}$ over one time period T is:

$$\begin{aligned}\bar{F}^{e}_{k\epsilon} = \int_0^T \sum_{m,odd}^{\infty}\sum_{l,odd}^{\infty} \Bigg(& \hat{I}_m \sin\Big(\left((mq-1)\omega+\lambda\right)t - mq\delta_k - \hat{\varphi}_m \Big) \\ & + \check{I}_m \sin\left(\left((mq+1)\omega-\lambda\right)t - mq\delta_k - \check{\varphi}_m\right) \Bigg) \\ & \Bigg(\hat{H}_l \cos\left(\left((lq-1)\omega+\lambda\right)t - lq\delta_k\right) \\ & + \check{H}_l \cos\left(\left((lq+1)\omega-\lambda\right)t - lq\delta_k\right) \Bigg) \frac{dt}{T}.\end{aligned} \tag{3.34}$$

As a reminder, the coefficients $\hat{I}_m$, $\check{I}_m$ are the amplitudes of the current harmonics, while $\hat{H}_l$, $\check{H}_l$ are the amplitudes of the PM flux harmonics. Let us separate the terms of (3.34) into four groups with coefficients $\hat{I}_m\hat{H}_l$; $\check{I}_m\check{H}_l$; $\hat{I}_m\check{H}_l$; and $\check{I}_m\hat{H}_l$. The terms in $\hat{I}_m\hat{H}_l$ cancel when integrated over a time period unless $(mq-1)\omega+\lambda = (lq-1)\omega+\lambda$, i.e. $m=l$. The remaining terms with $m \neq l$ are zero on average, but additional pulsating forces can result from them. Consequently, the total contribution of the terms in $\hat{I}_m\hat{H}_l$ to the average force is:

$$-\frac{1}{2}\sum_{m,odd}^{\infty} \hat{I}_m\hat{H}_m \sin\left(\hat{\varphi}_m\right). \tag{3.35}$$

This shows that the average force increases when the induced current is inductive, reaching a maximum value as the current-emf phase shift $\hat{\varphi}_m$ tends towards $\frac{\pi}{2}$. This is consistent with (Filatov and Maslen, 2001; Kluyskens and Dehez, 2009; Post and Ruytov, 1998). Although the guideline for a non-zero restoring force on the rotor of the bearing were already obtained in section 3.8, (3.35) confirms that their time-average is non-zero. Furthermore, the coefficients $\hat{H}_m$ and $\hat{I}_m$ decrease with m. Therefore, choosing $m = n = 1$ yields the maximum force, as will be shown in section 3.11.2. The previous analysis can be transposed easily to the terms in $\check{I}_m\check{H}_l$. Their mean value is:

$$-\frac{1}{2}\sum_{m,odd}^{\infty} \check{I}_m\check{H}_m \sin\left(\check{\varphi}_m\right). \tag{3.36}$$

Again, the maximum average force is obtained when $\check{\varphi}_m = \frac{\pi}{2}$.

Let us now consider the terms in $\hat{I}_m\check{H}_l$. Their time average cancels, except if $(mq-1)\omega+\lambda = (lq+1)\omega-\lambda$. However, the operation of a bearing shall not be

based on these terms since this identity can only be satisfied for specific values of ω and λ[1]. This is also the case for the terms in $\check{I}_m\hat{H}_l$.

Finally, let us have a look at the time average $\bar{F}_{k\phi}$ of $F_{k\phi}$. The contributions of the terms in $\hat{I}_m\hat{H}_l$ and in $\check{I}_m\check{H}_l$ to $\bar{F}_{k\phi}$ are, respectively:

$$\begin{aligned} &-\frac{1}{2}\sum_{m,odd}^{\infty}\hat{I}_m\hat{H}_m\cos\left(\hat{\varphi}_m\right) \\ &\frac{1}{2}\sum_{m,odd}^{\infty}\check{I}_m\check{H}_m\cos\left(\check{\varphi}_m\right). \end{aligned} \tag{3.37}$$

The inductive behaviour of the winding is also positive in this case, because it lowers the force $\bar{F}_{k\phi}$ that is known to badly affect the bearing stability (Filatov and Maslen, 2001; Kluyskens and Dehez, 2009).

3.10.2 Pulsating electrodynamic forces

In electrodynamic bearings, the presence of pulsating electrodynamic forces can induce vibrations reaching unacceptable levels, even if the time average of the centering force is satisfactory. Looking at (3.33), it appears that the pulsating force created by a single phase is significant as the current is a sine function of time and cancels every period. However, increasing the number of phases smooths the instantaneous force on the rotor.

To illustrate this, the electrodynamic force in presence of numerous phases is calculated assuming a static eccentricity configuration i.e., ω and ϵ are constant and $\lambda = 0$. The angular position of the k^{th} phase is:

$$\delta_k = \frac{\pi k}{qN} \tag{3.38}$$

where $k \in \{0, N-1\}$.

[1] An example of such specific kinematics yielding a non-zero average contribution to the force is the pure static-eccentricity case (ω and ϵ are constant, $\lambda = 0$). Then, the identity for a non-zero average force becomes $(m-l)q = 2$. Considering the properties of m, l, q, this translates into $q = 1$ and $m = l+2$, thereby ruling out the case $m = l = 1$ that is associated with the coefficients $\hat{I}_m\hat{H}_l$ of higher amplitudes. In this static-eccentricity case, this means that the contribution of these terms to the force are less significant than the contributions of the terms in $\hat{I}_m\hat{H}_l$. However, this highlights the importance of considering more than only the most significant harmonics when studying a bearing.

Let us have a look at the terms in $\hat{I}_m \hat{H}_l$ in (3.33):

$$\begin{aligned} F_\epsilon &= \sum_{k=0}^{N-1} F_{k\epsilon} \\ &= \sum_{m,odd}^{\infty} \sum_{l,odd}^{\infty} \hat{I}_m \hat{H}_l \left[\sum_{k=0}^{N-1} \sin\left((mq-1)\omega t - mq\delta_k - \hat{\varphi}_m\right) \right. \\ &\qquad \left. \cos\left((lq-1)\omega t - lq\delta_k\right) \right]. \end{aligned} \tag{3.39}$$

Substituting (3.38) in (3.39), the term between brackets yields:

$$\begin{aligned} \frac{1}{2} \sum_{k=0}^{N-1} \Bigg[& \sin\left((m-l)\, q\omega t - (m-l)\, \frac{\pi k}{N} - \hat{\varphi}_m \right) \\ & + \sin\left(((m+l)\, q - 2)\, \omega t - (m+l)\, \frac{\pi k}{N} - \hat{\varphi}_m \right) \Bigg]. \end{aligned} \tag{3.40}$$

In this equation, computing the sum gives a zero result for the first sine except if $(m-l)$ is a multiple of $2N$ and a zero result for the second sine except if $(m+l)$ is a multiple of $2N$. In other words, if the number of phases N increases, the terms inducing pulsating forces come from higher values of $(m-l)$ and/or $(m+l)$, corresponding to higher order terms $\hat{I}_m$ or $\hat{H}_l$. Since these coefficients usually decrease with m or l, the amplitude of the pulsating force component will decrease, reaching negligible values as the number of phases increases. The same reasoning leads to the same conclusion when applied to the other terms in (3.33), and to F_ϕ.

This highlights the importance of considering the full harmonic content of the magnetic field from the permanent magnets when studying the pulsating forces in an electrodynamic bearing.

3.10.3 Summary

Let us summarize the content of the present section. Firstly, it was shown that the time average of the centering electrodynamic force is non-zero when the guidelines from section 3.8 are met. Also, the behaviour of the bearings improves as the emf-current phase shift approaches $\frac{\pi}{2}$, because the average centering force $\bar{F}_\epsilon$ reaches a maximum whereas the destabilizing force $\bar{F}_\phi$ cancels. Consequently, making sure that the bearing has an inductive behaviour while operating at the required speed is critical.

Secondly, another design guideline was obtained in subsection 3.10.2. It consists in increasing the number of phases to reduce the amplitude of the pulsating forces.

3.11 Validations

Let us validate the results from section 3.8 regarding the pole pairs numbers. In this aim, the predictions of the model for the vector potential and the flux linked by a winding are compared with finite elements (FE) simulation results. The FE simulations are done using COMSOL Multiphysics v.4.2a.

The bearing considered for this validation is shown in Fig. 3.7. It comprises an internal rotor with p pole-pairs. The rotor has surface-mounted permanent magnets with a radial magnetization, a remanent magnetic flux density B_{rem}, and a magnetic permeability μ_r. The permeability of the rotor shaft and the stator yoke is infinite in the analytical model, whereas they are set to $\mu_i = 4000$ in the FE model. The stator winding phases have q pole-pairs and a helical shape as shown in Fig. 3.4(b). The wire is assumed to have no thickness and is located at radius R_w. The bearing parameters are summarized in Table 3.1.

Table 3.1: Bearing parameters for the validation.

parameter	value	units
R_i	3	mm
R_m	6.5	mm
R_w	7.5	mm
R_{we}	8	mm
R_o	10	mm
H	30	mm
B_{rem}	1.32	T
μ_r	1.01	-
μ_i	4000	-

In this section, only the most significant harmonics of the previous analytical expressions (3.7) and (3.17) are considered. For clarity purposes, the rotor eccentricity is described by the variable $e = \epsilon/g$, where the nominal airgap of the bearing $g = R_{we} - R_m$ in the present case.

3.11.1 Magnetic vector potential

The expression of the vector potential in the rotor frame (3.4) was validated by Rahideh and Korakianitis (2011). Let us now validate the expression of the vector potential in the stator frame (3.7). In particular, the focus is placed on the actual harmonic content and on the linear dependency between the harmonics amplitude and the eccentricity.

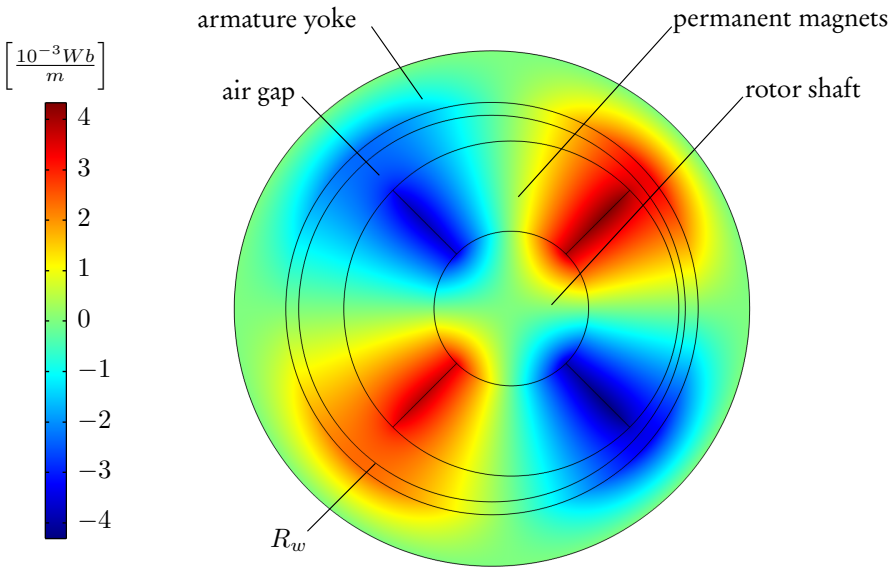

Fig. 3.7: Amplitude of A_z for $p = 2$ and $e = 0.5$.

Assuming $p = 2$ and $\phi = \gamma = 0$, the vector potential is first obtained with FE methods, see Fig. 3.7. The evolution of A_z with the eccentricity and the associated harmonic content are shown in Fig. 3.8(a) and (b), respectively. The harmonic content of A_z predicted by the analytical model is presented in Table 3.2. The first row of the table gives the harmonics numbers n corresponding to the nominal magnetic field, i.e. when $e = 0$. The other rows give the spatial periodicities of the vector potential harmonics when $e \neq 0$.

Table 3.2: Analytical model predictions of the vector potential harmonics for $p = 2$.

harmonic #	spatial periodicity		
n	$np-1$	np	$np+1$
1	1	2	3
3	5	6	7
5	9	10	11

Analytical predictions for the amplitude of the harmonics with $np\theta$-, $(np+1)\theta$- and $(np-1)\theta$-spatial periodicities, namely C_n, $\epsilon\hat{C}_n$ and $\epsilon\check{C}_n$ in (3.7), are compared with FE results in Fig. 3.9(a), (b) and (c), respectively. As shown in Fig. 3.9(a), the values of C_n are non-zero when $e = 0$ and remain constant with e, which was well predicted by the model. These values correspond to the amplitude of the harmonics of the magnetic field in the airgap when the rotor is centered. Fig. 3.9(b) shows the amplitude of the harmonics with $(np+1)\theta$-spatial periodicities, i.e. $\epsilon\hat{C}_n$. Again, their amplitudes are well predicted by the analytical model. They are zero when

there is no eccentricity and only appear when the rotor is off-centered, increasing linearly with e. Fig. 3.9(c) shows the amplitudes of the harmonics with $(np-1)\theta$-spatial periodicities, i.e. $\epsilon\check{C}_n$. The analytical prediction is appropriate for $n = 1$ i.e., for the θ-spatial periodicity harmonic but not in the other cases. This can be interpreted in the following way: the amplitudes of the harmonics with $(np-1)\theta$-periodicities are much lower than the amplitudes of the harmonics with $(np+1)\theta$-periodicities. Therefore, higher order effects in ϵ are not negligible and $\epsilon\check{C}_3$, $\epsilon\check{C}_5$ do not increase linearly with the eccentricity. As shown in Fig. 3.8(b), other harmonics appear when the rotor is off-centered, namely harmonics 4 and 8. They are second order effects which are neglected in the analytical model and therefore their predicted amplitudes are zero.

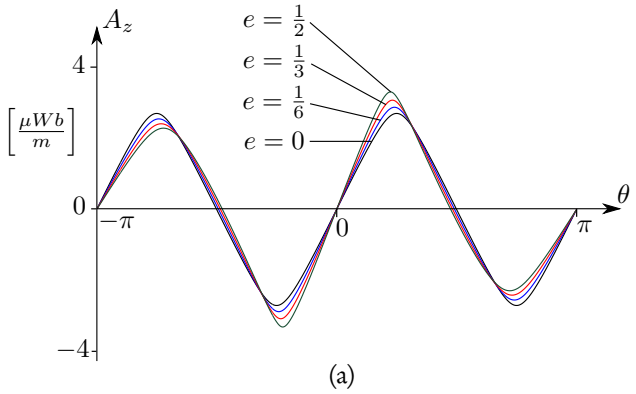

(a)

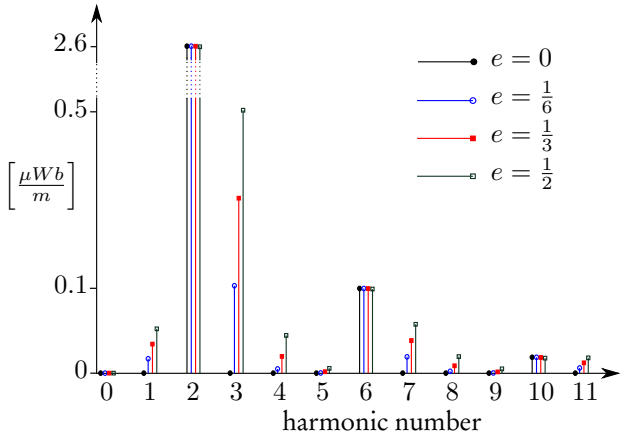

(b)

Fig. 3.8: FE results for the amplitude of the magnetic vector potential at radius R_w (a), and corresponding harmonic content of A_z (b).

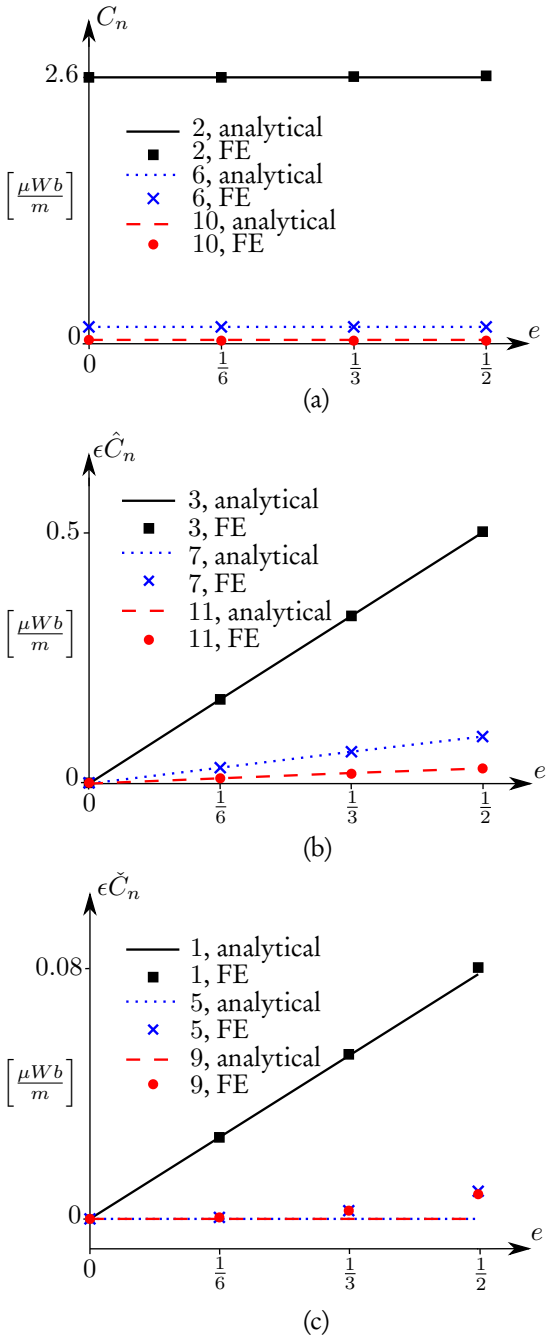

Fig. 3.9: Comparison between analytical FE predictions of the harmonic content of A_z with the eccentricity.

3.11.2 Permanent magnet flux

For this validation, the maximum amplitude of the magnetic flux linked by the winding is calculated for all the combinations corresponding to $p = 1, 2, 4$ and $q = 1, 2, 3, 4$ and for different values of e. The other parameters of the bearing are kept identical.

Table 3.3 gives the predictions of the analytical model concerning the magnetic flux for each winding and permanent magnets combination. In the white cells, the flux amplitude is predicted to be independent of e because q and p have the same parity, and therefore $mq \neq np + 1$ and $mq \neq np - 1$ for every couple (m, n). In these cases, either $mq = np$ is verified for the couples (m, n) indicated in the table and the predicted flux is non-zero, or $mq = np$ is not verified and the predicted flux is zero. As a result, the bearing cannot work since the flux does not vary with the off-centering, and sometimes the bearing is not even null-flux. In the green cells of table 3.3, the flux is predicted to grow linearly with e because either $mq = np + 1$ or $mq = np - 1$ is verified for the couples (m, n) given in the table. Furthermore, q and p having different parities in these cases, $mq \neq np$ for all the couples (m, n) and the flux is zero when the rotor is centered i.e., when $e = 0$. Only the couples (m, n) giving rise to a non-zero flux and having the lowest orders m and n are given in the table.

Table 3.3: Properties of the PM flux, and associated pair (m, n).

	$q = 1$	$q = 2$	$q = 3$	$q = 4$
$p = 1$	constant $(1,1)$ $(3,3)$ $(5,5)$	linear $(1,1)$ $(1,3)$ $(3,5)$	constant $(1,3)$ $(3,9)$	linear $(1,3)$ $(1,5)$
$p = 2$	linear $(1,1)$ $(3,1)$ $(5,3)$ $(7,3)$	constant $(1,1)$ $(3,3)$ $(5,5)$	linear $(1,3)$ $(3,5)$	null
$p = 4$	linear $(3,1)$ $(5,1)$	null	linear $(1,1)$	constant $(1,1)$ $(3,3)$ $(5,5)$

As shown in Fig. 3.10(a), the amplitude of the magnetic flux from the FE analysis remains almost constant with e and is non-zero at $e = 0$ when $(p, q) = (1, 1)$, $(1, 3)$, $(2, 2)$ and $(4, 4)$, which corresponds to analytical predictions. In this case, the harmonics created by the PMs when the rotor is centered are linked by the winding and the bearing is not null-flux. This will result in Joule losses when the rotor spins in the equilibrium position. These losses are significant because the winding links harmonics that are with significant amplitudes, see Fig. 3.8(b) and Fig. 3.10. When $(p, q) = (2, 4)$ and $(4, 2)$, the model predicts a zero flux and only second order effects

are present.

As shown in Fig. 3.10(a) and (b), the amplitude of the magnetic flux increases linearly with e when $(p, q) = (1, 2)$, $(2, 3)$, $(1, 4)$, $(2, 1)$, $(4, 1)$ and $(4, 3)$. In these cases, the data behave as predicted although some higher order effects in ϵ are visible as e increases, or when the predicted value of the flux is very low.

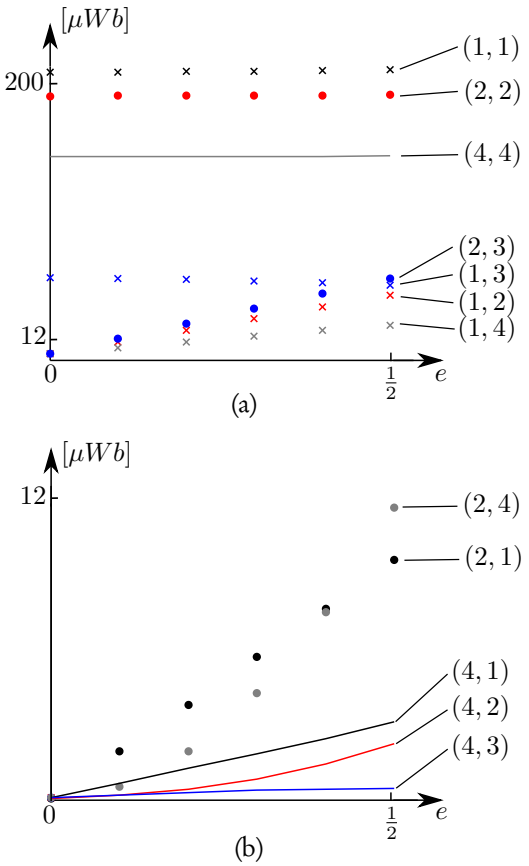

Fig. 3.10: FE results for the magnetic flux intercepted by the winding for different couples (p, q) and evolution with e. Harmonics with higher amplitudes (a), and lower amplitudes (b).

The validations were done in qualitative terms. Let us now give some quantitative comments. In practice, by observing Fig. 3.10, meeting the guideline $mq = np + 1$ for $m = n = 1$ yields higher flux amplitudes. Therefore, satisfying the identity $q = p + 1$ should be preferred when building a bearing based on this internal PM configuration.

Conversely, we observe that the identity $q = p - 1$ should be preferred in the external rotor case.

3.12 Conclusion

This chapter sets guidelines to build a centering, null flux electrodynamic bearing based on the interaction between a rotor with permanent magnets and an armature with short-circuited windings.

The design guidelines were obtained by developing an quasi-static, analytical model predicting the forces on the rotor. It was shown that imposing the null-flux characteristic and the presence of an electrodynamic force when the rotor is off-centered can be achieved by choosing the rotor and winding pole pairs numbers p and q in order to satisfy $mq = np + 1$ or $mq = np - 1$ for at least a couple (m, n).

This conclusion was validated for some values of ϵ up to half of the airgap, which can be considered as a realistic upper limit for the off-centering amplitude in an electrodynamic bearing. The FE results were in good agreement with the expectations from the analytical model, even though the presence of some second order effects in ϵ was observed for harmonics with high spatial periodicities at large rotor eccentricities.

In order to maximize the magnetic flux and the force, the FE simulations also highlighted that the rotor and armature pole pairs numbers should be such that $q = p \pm 1$. The identity $q = p + 1$ should be preferred in the internal rotor case and the identity $q = p - 1$ should be preferred in the external rotor case.

Finally, the model also showed that having a winding with an inductive behaviour has a positive effect on the time average centering force and on the stability of the bearing. This result has not been validated but corresponds to existing predictions in the literature. In addition, increasing the number of winding phases was shown to decrease the amplitude of the pulsating forces.

Dynamic model

4

Like most of the models from the literature, the quasi-static model presented in section 2.2 yields the forces on the rotor under the static eccentricity assumption. However, such a kinematic assumption constitute a strong limitation for a model that is used to study the rotor dynamics. Recent years saw the derivation of a linear state-space representation of the dynamics of electrodynamic bearings with no assumption on the kinematics of the rotor axis. However, the scope of this model is still limited regarding the bearing topologies.

This chapter presents an analytical lumped-parameter model of heteropolar bearings following the guideline $q = p \pm 1$. Compared with the literature (Detoni et al., 2012), some restrictions on the bearing topology are removed, namely:

1. the number of pole pairs of the PMs p is even and the number of winding pole pairs is $q = 1$, while a wider range of bearings could be considered by following the design guidelines from chapter 3;
2. the number of winding phases is $N = 2$, while increasing N could have a positive impact on the bearing stiffness (Dumont et al., 2016d) and reduce the parasitic eddy currents in the conductors (Bender and Post, 2000);
3. the PMs are attached to the stator, while this is not necessary for heteropolar EDBs;
4. no ferromagnetic yoke is attached to the windings. This restriction is also removed.

As a result, the dynamics and stability of a wider range of heteropolar electrodynamic bearings can now be studied with a linear model. Finally, this tool is applied to an example of bearing as a case study.

The content of this chapter is the subject of (Dumont et al., 2016b).

4.1 Parameters and variables

The bearing is composed of the PMs and winding parts with symmetry axes O_M and O_W, respectively. The frames and coordinates used in this chapter are given in Fig. 4.1 (a) and (b), depending on whether the winding or the PMs are on the stator.

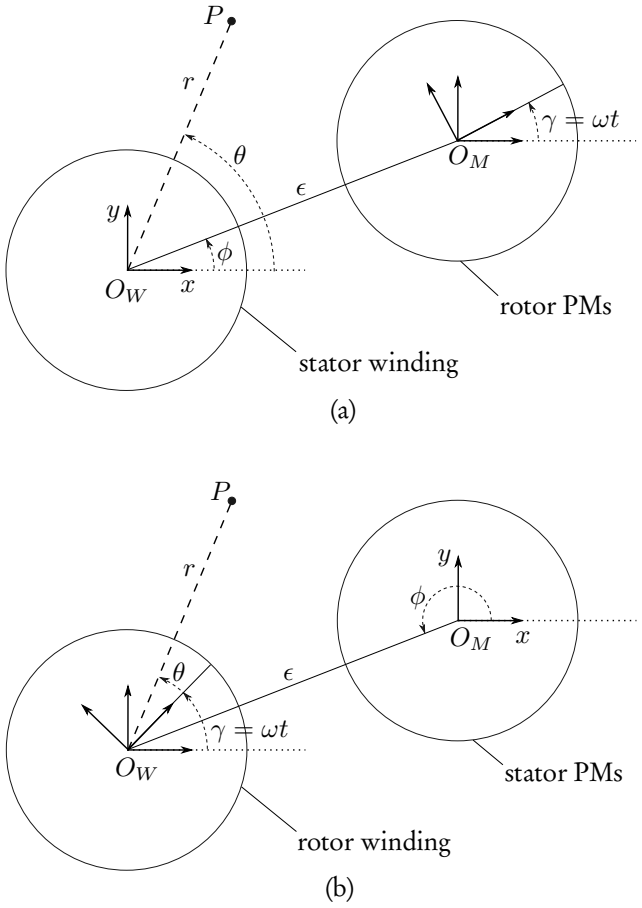

Fig. 4.1: Rotor and stator frames, and associated coordinates.

The position of the rotor axis in the stator frame is $(x = \epsilon\cos(\phi); y = \epsilon\sin(\phi))$ and the spin angle of the rotor is $\gamma = \omega t$. Using these coordinates and frames, all configurations from chapter 2.1.8 can be considered.

4.2 Assumptions

The following assumptions are made when deriving the model:

1. the materials have linear magnetic characteristics and therefore magnetic hysteresis and saturation are neglected;
2. the impact of the rotor off-centering ϵ on the winding inductances is neglected;
3. there is no proximity or skin effect in the conductors;
4. the eddy currents are neglected except in the windings;
5. the impacts of the rotor off-centering and of the slotting effect on the detent force are neglected;
6. only the main PM flux harmonic is considered in each phase;
7. the magnetic axes of the rotor and winding remain parallel;
8. the rotor spin speed ω is an input to the system and is constant;
9. the $N \geq 2$ phases are identical and evenly distributed around the winding axis.

4.3 PM flux linkage

Knowing the PM flux linkage allows to calculate the winding currents and the electrodynamic force on the rotor. Therefore, let us calculate the flux linked by the k^{th} winding phase by integrating the vector potential along the conductor:

$$\Phi_k = \oint_{\Gamma_k} \mathbf{A}.\mathbf{dl}. \tag{4.1}$$

The expression of $\mathbf{A}$ is derived in chapter 3 in the case of a winding attached to the stator:

$$\begin{aligned} A_z(r,\theta) = & A(r)\sin\left(p(\theta-\gamma)\right) \\ & + \epsilon A^i(r)\sin\left((p+1)\,\theta - p\gamma - \phi\right) \\ & + \epsilon A^e(r)\sin\left((p-1)\,\theta - p\gamma + \phi\right). \end{aligned} \tag{4.2}$$

Similarly, in the case of a winding attached to the rotor, the expression of $\mathbf{A}$ is:

$$\begin{aligned} A_z(r,\theta) = & A(r)\sin\left(p(\theta+\gamma)\right) \\ & + \epsilon A^i(r)\sin\left((p+1)\,\theta + (p+1)\,\gamma - \phi\right) \\ & + \epsilon A^e(r)\sin\left((p-1)\,\theta + (p-1)\,\gamma + \phi\right). \end{aligned} \tag{4.3}$$

As the end-effects are not considered, the magnetic vector potential is axial. In addition, only the components with the greatest amplitudes are considered. In (4.2) and (4.3), the term with $A(r)$ has p pole pairs and corresponds to the magnetic field when the rotor is centered. The terms with A^i and A^e are non-zero only when the rotor is off-centered. They are proportional to ϵ and have $p \pm 1$ pole pairs. One of these two harmonics is linked by the winding, depending on whether $q = p + 1$ or $q = p - 1$ is satisfied. Lastly, (4.2) and (4.3) are always expressed in the winding frame to ease the calculation of $\mathbf{\Phi}$. Since the vector potential is axial, (4.1) becomes:

$$\Phi_k = \oint_{\Gamma_k} A_z dl_z. \tag{4.4}$$

In the case of a bearing with the PMs attached to the rotor and $q = p+1$, this yields:

$$\begin{aligned}
\Phi_k &= \epsilon K_\Phi \cos\left((q-1)\,\gamma + \phi - q\delta_k\right) \\
&= K_\Phi \Big(\cos\left((q-1)\,\gamma - q\delta_k\right) \epsilon \cos\left(\phi\right) \\
&\qquad - \sin\left((q-1)\,\gamma - q\delta_k\right) \epsilon \sin\left(\phi\right) \Big) \\
&= K_\Phi \Big(\cos\left((q-1)\,\gamma - q\delta_k\right) x \\
&\qquad - \sin\left((q-1)\,\gamma - q\delta_k\right) y \Big),
\end{aligned} \tag{4.5}$$

where K_Φ is a constant that depends only on the geometric and magnetic parameters of the bearing, and δ_k is the angular position of the k^{th} phase:

$$\delta_k = \frac{2\pi(k-1)}{qN}, \tag{4.6}$$

with $k \in \{1, N\}$. Rewriting (4.5) in a matrix form yields:

$$\mathbf{\Phi} = K_\Phi \mathbf{P}\mathbf{Q}\mathbf{x}, \tag{4.7}$$

where $\mathbf{\Phi}$ is the vector of the magnetic flux in the winding phases and:

$$\mathbf{P} = \begin{bmatrix} \cos\left(q\delta_1\right) & \sin\left(q\delta_1\right) \\ \vdots & \vdots \\ \cos\left(q\delta_N\right) & \sin\left(q\delta_N\right) \end{bmatrix} \tag{4.8}$$

$$\mathbf{Q} = \begin{bmatrix} \cos\left((q-1)\,\gamma\right) & -\sin\left((q-1)\,\gamma\right) \\ \sin\left((q-1)\,\gamma\right) & \cos\left((q-1)\,\gamma\right) \end{bmatrix}. \tag{4.9}$$

This corresponds to a bearing with PMs attached to the rotor and $q = p + 1$. In the other configurations, the matrix $\mathbf{Q}$ in (4.7) changes, see appendix B.

In the next sections, the model is derived in the particular case of a bearing with PMs attached to the rotor and $q = p + 1$, but the final results are provided for all configurations and for $q = p \pm 1$.

4.4 Governing equations

This section presents the equations governing the electrical, mechanical and magnetic variables in the bearing.

4.4.1 Electrical equations

The current I_k in the short-circuited winding phase k is governed by Faraday's law applied to R-L circuits:

$$u_k = 0 = R_k I_k + \frac{d\Psi_k}{dt} = R_k I_k + \frac{d\left(\sum_{l=1}^{N} L_{kl} I_l\right)}{dt} + \frac{d\Phi_k}{dt}, \tag{4.10}$$

where Ψ_k is the total magnetic flux linkage in the winding phase, Φ_k is the flux linkage from the PMs only, and R_k and L_{kl} are the phase resistance and mutual inductances, respectively. Because of the assumptions from section 4.2, the inductance matrix is constant and (4.10) yields:

$$0 = R_k I_k + \sum_{l=1}^{N} L_{kl} \frac{dI_l}{dt} + \frac{d\Phi_k}{dt}, \tag{4.11}$$

which can be rewritten in matrix form as:

$$\mathbf{0} = \mathbf{R}\mathbf{I} + \mathbf{L}\frac{d\mathbf{I}}{dt} + \frac{d\mathbf{\Phi}}{dt}. \tag{4.12}$$

As stated previously, the winding phases are identical, evenly distributed and their properties are constant. Therefore, the inductance matrix $\mathbf{L}$ is symmetric and circulant[1]:

$$\begin{aligned} L_{kl} &= L_{lk} \\ L_{kl} &= L_{k+i,l+i} \\ L_{1l} &= L_{1,N+2-l}, \end{aligned} \tag{4.13}$$

where $i, k, l \in \{1, N\}$. The phase resistances are equal which yields:

$$\mathbf{R} = R\mathbb{1}, \tag{4.14}$$

where R is the phase resistance and $\mathbb{1}$ is the identity matrix.

[1] Additional inductors of equal impedance could be connected in series with each winding phase if necessary. This does not affect the properties (4.13) and could be used to modify the stiffness or the stability properties of the bearing.

4.4.2 Electromagnetic equations

As a reminder, the general expressions of the electromagnetic forces on the rotor are:

$$\begin{aligned} F_x &= \frac{\partial W_0}{\partial x} + \sum_{k=1}^{N} \frac{\partial \Phi_k}{\partial x} I_k + \frac{1}{2} \sum_{k=1}^{N} \sum_{l=1}^{N} \frac{\partial L_{kl}}{\partial x} I_k I_l \\ F_y &= \frac{\partial W_0}{\partial y} + \sum_{k=1}^{N} \frac{\partial \Phi_k}{\partial y} I_k + \frac{1}{2} \sum_{k=1}^{N} \sum_{l=1}^{N} \frac{\partial L_{kl}}{\partial y} I_k I_l, \end{aligned} \tag{4.15}$$

where the terms $\frac{\partial W_0}{\partial x}$ and $\frac{\partial W_0}{\partial y}$ correspond to the gradient of the magnetic coenergy in the system at zero current. It is a detent force due to the presence of PMs. Under assumptions 1 and 5 from section 4.2, this detent force acts in the direction of the off-centering and it can be associated with a constant negative stiffness, as shown in section 3.5. In addition, the inductance matrix $\mathbf{L}$ is constant. Therefore (4.15) can be rewritten as:

$$\begin{aligned} F_x &= -K_d x + \sum_{k=1}^{N} \frac{\partial \Phi_k}{\partial x} I_k \\ F_y &= -K_d y + \sum_{k=1}^{N} \frac{\partial \Phi_k}{\partial y} I_k, \end{aligned} \tag{4.16}$$

where $K_d \leq 0$ is the stiffness associated with the detent force. Defining:

$$\begin{aligned} \mathbf{F} &= \begin{bmatrix} F_x \\ F_y \end{bmatrix} \\ \mathbf{x} &= \begin{bmatrix} x \\ y \end{bmatrix}, \end{aligned} \tag{4.17}$$

the matrix form of (4.16) yields:

$$\mathbf{F} = -K_d \mathbf{x} + \left[\nabla \mathbf{\Phi}^T\right] \mathbf{I}. \tag{4.18}$$

4.4.3 Mechanical equations

Let us consider a simple rotor model consisting of a point mass with two degrees of freedom in presence of non-rotating damping (Genta, 2005)[1]. In this case, the equation governing the rotor dynamics is:

$$M\ddot{\mathbf{x}} + C\dot{\mathbf{x}} = \mathbf{F} + \mathbf{F_e}, \tag{4.19}$$

where M is the rotor mass, C is the amount of external non-rotating damping in the system, and $\mathbf{F_e}$ are the external forces acting on the rotor.

[1] As a result, the rotor is assumed to be perfectly balanced, and gyroscopic effects are not considered.

4.5 Variables transformation

Thanks to the presence of symmetries in the bearing geometry and phases distribution, the study of the present EDB has some similarities with the study of N-phased rotating field machines. As for the rotating field machines, it is possible to reduce the number of variables needed to describe the operation of EDBs through an appropriate transformation. This is done in this section, following the approach described in (White and Woodson, 1959).

4.5.1 Electrical equations

Let us define the variables transformation:

$$\begin{aligned} \mathbf{I} &= \mathbf{U}\mathbf{I^s}; \\ \mathbf{\Phi} &= \mathbf{U}\mathbf{\Phi^s}, \end{aligned} \tag{4.20}$$

with:

$$U_{kl} = \frac{1}{\sqrt{N}} e^{-j(k-1)(l-1)\frac{2\pi}{N}}, \tag{4.21}$$

where $j = \sqrt{-1}$. Substituting (4.20) into (4.12) yields:

$$\mathbf{0} = R\mathbf{U}\mathbf{I^s} + \mathbf{L}\mathbf{U}\frac{d\mathbf{I^s}}{dt} + \mathbf{U}\frac{d\mathbf{\Phi^s}}{dt}. \tag{4.22}$$

The inverse of matrix $\mathbf{U}$ is given in (White and Woodson, 1959):

$$U^{-1}_{kl} = \frac{1}{\sqrt{N}} e^{j(k-1)(l-1)\frac{2\pi}{N}}. \tag{4.23}$$

Multiplying (4.22) by $\mathbf{U^{-1}}$ gives:

$$\mathbf{0} = R\mathbf{I^s} + \mathbf{U^{-1}}\mathbf{L}\mathbf{U}\frac{d\mathbf{I^s}}{dt} + \frac{d\mathbf{\Phi^s}}{dt}. \tag{4.24}$$

Due to the properties of $\mathbf{U}$ and $\mathbf{L}$, the product $\mathbf{U^{-1}}\mathbf{L}\mathbf{U} = \mathbf{L^s}$ is a diagonal matrix and:

$$L^s_{ii} = \sum_{k=1}^{N} L_{1k} e^{-j(i-1)(k-1)\frac{2\pi}{N}}, \tag{4.25}$$

with $i \in \{1, N\}$. As a result, (4.24) is a set of N decoupled equations:

$$\mathbf{0} = R\mathbf{I^s} + \mathbf{L^s}\frac{d\mathbf{I^s}}{dt} + \frac{d\mathbf{\Phi^s}}{dt}. \tag{4.26}$$

Based on (4.7) and (4.20), $\mathbf{\Phi^s}$ can be calculated, see appendix C:

$$\mathbf{\Phi^s} = \frac{K_\Phi \sqrt{N}}{2} \begin{bmatrix} 0 & 0 \\ 1 & j \\ 0 & 0 \\ \vdots & \vdots \\ 0 & 0 \\ 1 & -j \end{bmatrix} \mathbf{Qx}. \tag{4.27}$$

In this vector, only the components Φ_2^s et Φ_N^s are non-zero. As a result, only two equations in (4.26) have an inhomogeneous term. As these equations are decoupled, only the corresponding currents I_2^s and I_N^s are non-zero. Defining:

$$\mathbf{\Phi^r} = \begin{bmatrix} \Phi_2^s \\ \Phi_N^s \end{bmatrix} = \frac{K_\Phi \sqrt{N}}{2} \begin{bmatrix} 1 & j \\ 1 & -j \end{bmatrix} \mathbf{Qx} \tag{4.28}$$

$$\mathbf{I^r} = \begin{bmatrix} I_2^s \\ I_N^s \end{bmatrix}, \tag{4.29}$$

the number of governing equations for the current can be reduced to two and (4.26) yields:

$$\mathbf{0} = R\mathbf{I^r} + \mathbf{L^r} \frac{d\mathbf{I^r}}{dt} + \frac{d\mathbf{\Phi^r}}{dt}, \tag{4.30}$$

where $\mathbf{L^r} = L_c \mathbb{1}$ and:

$$L_c = L_{22}^s = L_{NN}^s = \sum_{k=1}^{N} L_{1k} \cos\left((k-1) \frac{2\pi}{N} \right) \tag{4.31}$$

is the cyclic inductance of the winding. Finally, substituting $\mathbf{\Phi^r}$ with its expression into (4.30) yields:

$$\mathbf{0} = R\mathbf{I^r} + L_c \frac{d\mathbf{I^r}}{dt} + \frac{K_\Phi \sqrt{N}}{2} \begin{bmatrix} 1 & j \\ 1 & -j \end{bmatrix} \left[\dot{\mathbf{Q}}\mathbf{x} + \mathbf{Q}\dot{\mathbf{x}} \right]. \tag{4.32}$$

4.5.2 Electromagnetic equations

Let us also apply the change of variables (4.20) to the expression of the force (4.18). First, as the current is a real variable, (4.18) can be rewritten as:

$$\mathbf{F} = -K_d \mathbf{x} + \left[\nabla \mathbf{\Phi}^T \right] \mathbf{I}^*, \tag{4.33}$$

where $\mathbf{I}^*$ denotes the complex conjugate of $\mathbf{I}$. Then, substituting (4.20) into (4.33) yields:

$$\begin{aligned} \mathbf{F} &= -K_d \mathbf{x} + \left(\nabla \left[\mathbf{U\Phi^s} \right]^T \right) (\mathbf{UI^s})^* \\ &= -K_d \mathbf{x} + \left(\nabla \left[\mathbf{\Phi^s} \right]^T \right) \mathbf{U^T U^* I^{s*}}. \end{aligned} \tag{4.34}$$

Since $\mathbf{U^T} = \mathbf{U}$ and $\mathbf{U}^* = \mathbf{U^{-1}}$, (4.34) becomes:

$$\mathbf{F} = -K_d\mathbf{x} + \left(\nabla\left[\mathbf{\Phi^s}\right]^T\right)\mathbf{I^{s*}}. \tag{4.35}$$

Since only Φ_2^s and Φ_N^s are non-zero in $\mathbf{\Phi^s}$ and only I_2^s and I_N^s are non-zero in $\mathbf{I}^s$, (4.35) can be rewritten as:

$$\mathbf{F} = -K_d\mathbf{x} + \left(\nabla\left[\mathbf{\Phi^r}\right]^T\right)\mathbf{I^{r*}}. \tag{4.36}$$

Finally, substituting (4.28) into (4.36) yields:

$$\mathbf{F} = -K_d\mathbf{x} + \frac{K_\Phi\sqrt{N}}{2}\mathbf{Q^T}\begin{bmatrix}1 & 1\\ j & -j\end{bmatrix}\mathbf{I^{r*}}. \tag{4.37}$$

As a result of the variable transformation (4.20), the number of variables in the current and magnetic flux vectors are lowered from N to 2, as well as the number of electrical equations in (4.32).

4.6 Dynamic model

The final equation linking the forces and the position of the rotor is obtained by substituting the current variables in (4.32) and (4.37).

4.6.1 Current variables elimination

The number of variables of the system can be further reduced by eliminating the currents in the electrical and electromechanical equations. Let us isolate $\mathbf{I^{r*}}$ in (4.37):

$$\mathbf{I^{r*}} = \frac{1}{K_\Phi\sqrt{N}}\begin{bmatrix}1 & -j\\ 1 & j\end{bmatrix}\mathbf{Q}\left[\mathbf{F} + K_d\mathbf{x}\right]. \tag{4.38}$$

Since $\mathbf{F}$ and $\mathbf{x}$ are real, obtaining $\mathbf{I^r}$ from (4.38) is straightforward:

$$\mathbf{I^r} = \mathbf{I^{r**}} = \frac{1}{K_\Phi\sqrt{N}}\begin{bmatrix}1 & j\\ 1 & -j\end{bmatrix}\mathbf{Q}\left[\mathbf{F} + K_d\mathbf{x}\right]. \tag{4.39}$$

Then, substituting (4.39) into (4.32) yields:

$$\begin{aligned}\mathbf{0} =& \frac{R}{K_\Phi\sqrt{N}}\begin{bmatrix}1 & j\\ 1 & -j\end{bmatrix}\mathbf{Q}\left[\mathbf{F} + K_d\mathbf{x}\right]\\ &+ \frac{L_c}{K_\Phi\sqrt{N}}\begin{bmatrix}1 & j\\ 1 & -j\end{bmatrix}\left[\dot{\mathbf{Q}}\left[\mathbf{F} + K_d\mathbf{x}\right] + \mathbf{Q}\left[\dot{\mathbf{F}} + K_d\dot{\mathbf{x}}\right]\right]\\ &+ \frac{K_\Phi\sqrt{N}}{2}\begin{bmatrix}1 & j\\ 1 & -j\end{bmatrix}\left[\dot{\mathbf{Q}}\mathbf{x} + \mathbf{Q}\dot{\mathbf{x}}\right],\end{aligned} \tag{4.40}$$

which can be further simplified by multiplying to the left by $\frac{K_\Phi\sqrt{N}\mathbf{Q^T}}{2}\begin{bmatrix}1 & 1\\ -j & j\end{bmatrix}$:

$$\begin{aligned}\mathbf{0} =& R\left[\mathbf{F}+K_d\mathbf{x}\right]\\ &+L_c\left[\mathbf{Q^T}\dot{\mathbf{Q}}\left[\mathbf{F}+K_d\mathbf{x}\right]+\left[\dot{\mathbf{F}}+K_d\dot{\mathbf{x}}\right]\right]\\ &+\frac{K_\Phi^2 N}{2}\left[\mathbf{Q^T}\dot{\mathbf{Q}}\mathbf{x}+\dot{\mathbf{x}}\right].\end{aligned} \tag{4.41}$$

Considering the definition of $\mathbf{Q}$ in (4.9):

$$\mathbf{Q^T}\dot{\mathbf{Q}}=\omega_e\begin{bmatrix}0 & -1\\ 1 & 0\end{bmatrix}, \tag{4.42}$$

where $\omega_e = (q-1)\omega$ is the electrical pulsation of the currents in the static-eccentricity position, (4.41) reduces to:

$$\begin{aligned}\dot{\mathbf{F}} =& -\frac{R}{L_c}\mathbf{F}-\omega_e\begin{bmatrix}0 & -1\\ 1 & 0\end{bmatrix}\mathbf{F}-\left(K_d+\frac{K_\Phi^2 N}{2L_c}\right)\dot{\mathbf{x}}\\ &-\frac{RK_d}{L_c}\mathbf{x}-\omega_e\left(K_d+\frac{K_\Phi^2 N}{2L_c}\right)\begin{bmatrix}0 & -1\\ 1 & 0\end{bmatrix}\mathbf{x}.\end{aligned} \tag{4.43}$$

The currents are not involved anymore in the governing equation (4.43). However, they can be deduced from the forces and rotor motion using (4.38) and (4.20). Finally, using the complex notation which is widespread in the field of rotordynamics, (4.43) can be restated as follows:

$$\begin{aligned}\dot{F} =& -\frac{R}{L_c}F-j\omega_e F-K_d\dot{z}-\frac{K_\Phi^2 N}{2L_c}\dot{z}\\ &-\frac{RK_d}{L_c}z-j\omega_e zK_d-\frac{K_\Phi^2 N\omega_e}{2L_c}jz;\end{aligned} \tag{4.44}$$

where:

$$\begin{aligned}F &= F_x+jF_y\\ z &= x+jy.\end{aligned} \tag{4.45}$$

This identity relates the force and the radial position of the rotor through a linear equation with constant coefficients. Replacing by the appropriate expression for ω_e given in Table 4.1, it applies for all bearing configurations.

4.6.2 Parameters identification

The model equation (4.44) comprises six parameters that depend on the magnetic bearing only. The number of winding phases N and the electrical pulsation ω_e (see

Table 4.1) are set arbitrarily, whereas the four other parameters can be identified using analytical or computational models, or experiments. Namely, R is the phase resistance, L_c is the cyclic inductance given in (4.31), K_d is the detent stiffness, and K_Φ is the flux constant given in (4.5).

Table 4.1: Electrical pulsation ω_e as a function of the spin speed ω.

null-flux characteristic	rotor part	ω_e
$q = p + 1$	magnets	$(q-1)\omega$
	winding	$-q\omega$
$q = p - 1$	magnets	$-(q+1)\omega$
	winding	$q\omega$

If a static-eccentricity model or experimental data are available, the bearing parameters can be identified in another, indirect way. In particular, K_d corresponds to the bearing stiffness when the rotor does not spin and is in a static-eccentricity position, i.e., when $\dot{z} = 0$ and $\omega = 0$. Also, $NK_\Phi^2/(2L_c) + K_d$ corresponds to the bearing stiffness if the rotor is in a static-eccentricity position and the winding has a purely inductive behaviour, i.e., when $\dot{z} = 0$ and $R \ll |\omega_e| L_c$.

4.6.3 State-space representation

A complete electromechanical model of the system results from the coupling of (4.44) with a mechanical model of the rotor, e.g. (4.19). Using the complex formulation, (4.19) becomes:

$$M\ddot{z} + C\dot{z} = F + F_e. \tag{4.46}$$

Coupling (4.44) and (4.46) yields a state-space representation of the rotor dynamics[1]:

$$\begin{bmatrix} \dot{F} \\ \ddot{z} \\ \dot{z} \end{bmatrix} = \mathbf{A} \begin{bmatrix} F \\ \dot{z} \\ z \end{bmatrix} + \mathbf{B} F_e, \tag{4.47}$$

where the dynamic and input gain matrices are:

$$\mathbf{A} = \begin{bmatrix} -\frac{R}{L_c} - j\omega_e & -K_d - \frac{K_\Phi^2 N}{2L_c} & -\frac{RK_d}{L_c} - j\omega_e K_d - j\frac{\omega_e K_\Phi^2 N}{2L_c} \\ \frac{1}{M} & -\frac{C}{M} & 0 \\ 0 & 1 & 0 \end{bmatrix} \tag{4.48}$$

$$\mathbf{B} = \frac{1}{M} \begin{bmatrix} 0 & 1 & 0 \end{bmatrix}^T.$$

[1] The state-space representation using the real notation is given in the appendix D.

The root locus of the state-space model is obtained by calculating the eigenvalues of (4.48), yielding the stability of the system.

4.7 Case study

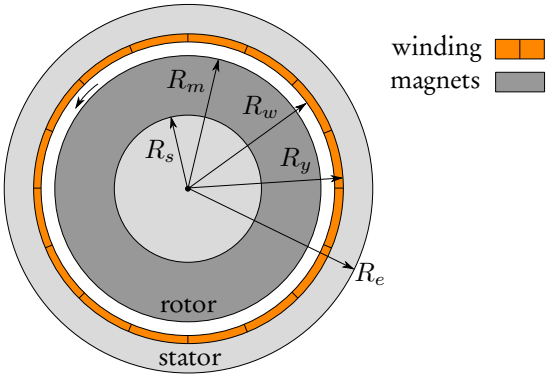

Fig. 4.2: Bearing with an air gap winding on the stator and surface-mounted PMs attached to an internal rotor.

Using the model derived in the previous sections, let us analyze the stability of the bearing in Fig. 4.2. It comprises an internal rotor with PMs and a stator with an air gap winding and a ferromagnetic yoke. The magnetization pattern of the permanent magnets is parallel with one pole pair ($p = 1$), and the remanent magnetization is 1.32 T. The winding has $q = p + 1 = 2$ pole pairs and three phases ($N = 3$). Lastly, the dimensions of the bearing are given in Table 4.2.

Table 4.2: Bearing dimensions [mm].

parameter	value
R_s	10
R_m	18
R_w	20
R_y	21
R_e	25
L (active length)	70

The parameters of $\mathbf{A}$ corresponding to this bearing are summarized in Table 4.3. Some of them are set arbitrarily, namely M and C. The electrical pulsation $\omega_e = \omega$ because the magnets are attached to the rotor and $q = p + 1$, see Table 4.1. The other parameters are calculated using the two-dimensional static-eccentricity model presented in chapter 5, and applying the method described in section 4.6.2.

Table 4.3: Model parameters.

parameter	value	units
M	1	kg
N	3	-
C	$\{0, 100\}$	Ns/m
R	4.35	Ω
L_c	3.2	mH
K_Φ^2	600	NsΩ/m
K_d	-139	kN/m
ω_e	ω	rad/s

Then, the eigenvalues of $\mathbf{A}$ are computed for different spin speeds $\omega \in [0, 2\pi 4000]$ rad/s to obtain the root locus of the system in Fig. 4.3(a).

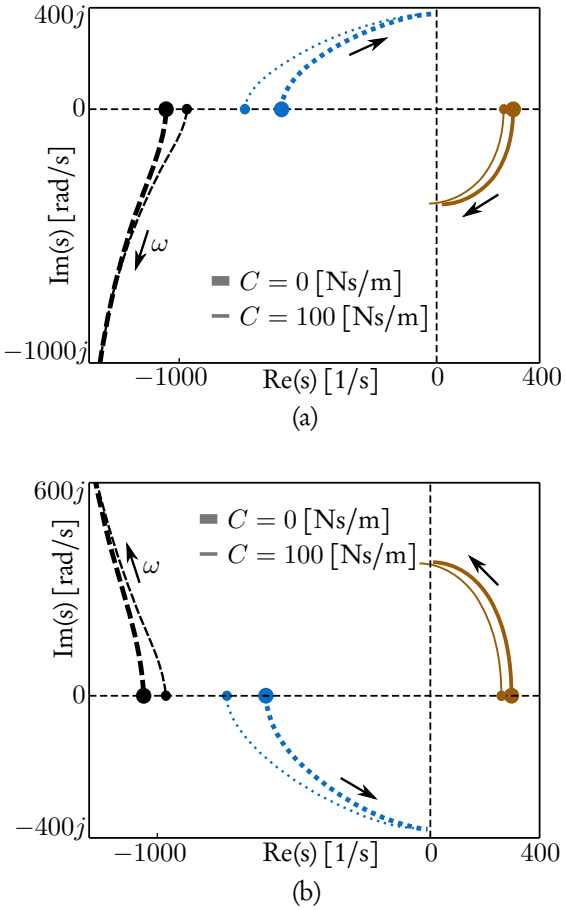

Fig. 4.3: Root loci of the EDB. (a) Rotating PMs. (b) Rotating winding.

The thick and thin lines correspond to $C = 0$ or 100 Ns/m, respectively. In Fig. 4.3(b), the root locus of a bearing with the same geometrical dimensions but with a different configuration is presented: the winding is on the rotor and the magnets are on the stator, see Fig. 2.14(c). The parameters of the model remain the same as in the PMs rotor configuration except that $\omega_e = -2\omega$ because the PMs are attached to the stator and $q = p + 1$, see Table 4.1.

In Fig. 4.3, the dashed and dotted branches correspond to roots with negative real parts. The roots on the solid branches always have a positive real part when $C = 0$ and therefore the bearing is always unstable in the absence of external damping. This is consistent with previous results (Filatov and Maslen, 2001; Kluyskens and Dehez, 2013; Tonoli et al., 2011). On the other hand, the bearing can be stabilized by adding external damping. In Figs. 4.3(a) and (b), the unstable roots cross the imaginary axis at 100 krpm and 50 krpm, respectively. In any case, a backup bearing is still required at low speed for the rotating machine to operate.

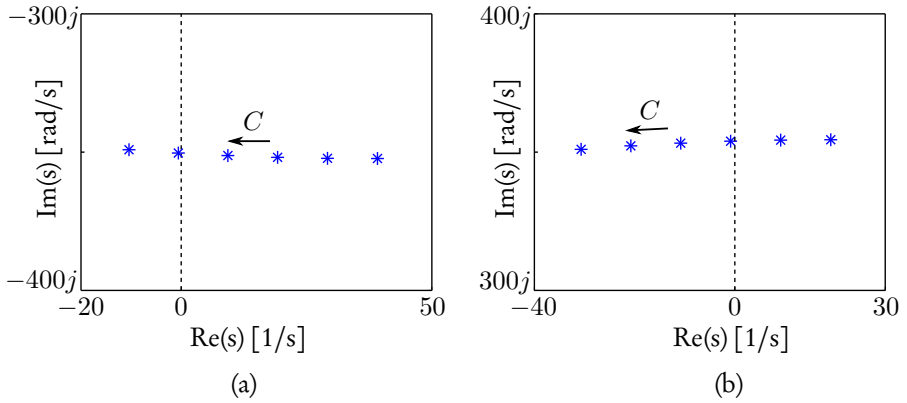

Fig. 4.4: Detailed view of the root loci showing the position of the unstable root for six equally spaced values of damping $C \in \{0, 100\}$. (a) Rotating PMs. (b) Rotating winding.

The effect of the damping on the unstable root is shown in Fig. 4.4. This was obtained for a bearing with the same parameters as in Table 4.2, except that $R_y = 22$ mm. The additional damping $C \in [0, 100]$ Ns/m and the spin speed is $\omega = 2000\pi$ rad/s. At such speed, the winding has an inductive behavior and the horizontal displacement of the unstable root is proportional to the amount of additional damping. This is further investigated in chapter 5.

4.8 Conclusion

In this chapter, an electromechanical model predicting the dynamics of a rotor supported by heteropolar EDBs was derived. It allows to evaluate the performance and stability of the system, and to select the most suitable bearing for a given application. This electromechanical model results from the combination of a mechanical model of the rotor with two degrees of freedom and a lumped-parameter model of the forces that does not assume a static eccentricity of the rotor.

The resulting state-space model is linear and requires no assumption on the kinematics of the rotor. The bearing is characterized by six parameters and a way to identify them was presented. Remarkably, this parameters identification process does not require to solve for the currents and only involves static-eccentricity simulations.

Compared to the state of the art, the present model removes numerous limitations on the bearing geometry, namely the presence of a ferromagnetic yoke attached to the winding, the number of pole pairs and phases of the winding and PMs, and the possibility to attach the PMs to the rotor or to the stator. The internal and external rotor cases are included. Furthermore, the developments included different topologies, namely the air gap winding, slotted and bell topologies.

As a result, a wider range of bearings with potentially increased performance is now in the scope of a dynamic model, thereby facilitating their comparison and optimization.

Lastly, a case study showed that such a bearing is unstable in the absence of external damping. However, this conclusion applies for any bearing topology and configuration. Since this external damping should be contactless to remain consistent with the magnetic bearing approach, it should rely on electromagnetic forces. As introducing such damping between the rotor and the stator can be an issue, the present model can be used to minimize the amount of damping required to achieve stability.

Finally, let us note that a state-space representation for other kinds of rotor models (Detoni et al., 2016) and damping (Tonoli et al., 2011) can be obtained following the same approach as in this chapter.

Bearing design

5

In this chapter, the modeling tools developed in the previous chapters are applied to the comparison and optimization of bearings. A first section presents the performance criteria of EDBs and introduces a graphical approach to evaluate them. In a second section, this graphical tool is used to study the impact of the yoke material on the performance of a bearing. A validation of this graphical tool is also presented. Finally, a third section presents the optimization of a yokeless EDB using the model developed in chapter 4.

The content of this chapter is the subject of (Dumont et al., 2014a, 2016c).

5.1 Performance criteria

As stated in the introduction of this manuscript, the implementation of EDBs in practical applications is prevented by their low stiffness and stability issues. The radial stiffness should thus be maximized and will be considered as a first bearing performance criterion. The stability issue results from the need of external damping to stabilize the bearing, as shown in section 4.7. This can be solved providing additional damping proportional to the lateral speed of the rotor, as proposed in (Filatov and Maslen, 2001; Kluyskens and Dehez, 2013; Tonoli et al., 2011). However, the difficulty of adding such damping consistently with the EDB approach, i.e. in a passive and contactless way, is widely acknowledged. As a result, the amount of damping required for the stabilization should thus be minimized and will be considered as a second performance criterion. In the next sections, the minimum amount of damping required for stabilization is referred to as the instability margin. This damping and the radial stiffness are denoted C_s and K_ϵ, respectively.

5.1.1 Graphical method

Let us derive a graphical method to evaluate the performance of a bearing with two degrees of freedom. This method is based on the analysis of root loci plots, where

the position of the roots is linked to the bearing performance criteria. To establish this link, a state-space representation of the bearing dynamics is proposed, whose eigenvalues yield the system roots. This state-space representation is based on a quasi-static model, as this allows for obtaining analytical expressions of the roots. These expressions can then be analyzed to highlight the link between the root position and the performance criteria.

As stated in section 2.2.1, the static-eccentricity assumption limits the scope of the quasi-static models as the accuracy of the current and force predictions depends on the rotor motion. However, the forces are coupled to a rotor mechanical model that is not impacted by the static-eccentricity assumption. Therefore, this assumption does not prevent the prediction of the rotor dynamics.

In this section, the quasi-static model is obtained by imposing the static-eccentricity assumption on the dynamic model derived in chapter 4, see the schematic in Fig. 2.15. Under the quasi-static assumption, (4.44) yields:

$$\begin{aligned} F &= -\left(K_d + \frac{\omega_e^2 K_\Phi^2 L_c N}{2\left(R^2 + (\omega_e L_c)^2\right)}\right) z - j\left(\frac{\omega_e K_\Phi^2 R N}{2\left(R^2 + (\omega_e L_c)^2\right)}\right) z \\ &= -K_\epsilon z - j K_\phi z. \end{aligned} \tag{5.1}$$

Let us define $F_\epsilon = -K_\epsilon |z|$ and $F_\phi = -K_\phi |z|$, i.e. the amplitude of the force components in the direction of the off-centering and in the direction perpendicular to it, see Fig. 5.4. When $K_\epsilon > 0$, it has a positive effect since F_ϵ acts on the rotor towards the axis of the winding. On the contrary, K_ϕ has a negative effect on the stability of the bearing whatever its sign. The associated tangential force induces a whirling motion of the rotor, following an outwardly growing spiral trajectory around the axis of the winding. This prevents the rotor from coming back towards the center of the winding. As stated previously, electrodynamic bearings are thus not stable unless a way to counterbalance the effect of K_ϕ is provided.

Coupling (5.1) with the mechanical model (4.46), the equation of motion of the rotor is:

$$M\ddot{z} + C\dot{z} + K_\epsilon z + jK_\phi z = 0, \tag{5.2}$$

where C is the external damping added in the system. Let us relate the position of the roots of the system governed by 5.2 to C_s and K_ϵ. The state-space equations associated with (5.2) are:

$$\begin{bmatrix} \ddot{z} \\ \dot{z} \end{bmatrix} = \mathbf{A} \begin{bmatrix} \dot{z} \\ z \end{bmatrix} + \mathbf{B}, \tag{5.3}$$

where:

$$\mathbf{A} = \begin{bmatrix} \frac{-C}{M} & \frac{-K_\epsilon - jK_\phi}{M} \\ 1 & 0 \end{bmatrix}. \tag{5.4}$$

In (5.3), matrix **B** is the external input force matrix divided by the mass M and **A** is the dynamic matrix. The two eigenvalues of **A** are:

$$\rho_{1,2} = \frac{-C}{2M} \pm \sqrt{\left(\frac{C}{2M}\right)^2 - \frac{K_\epsilon + jK_\phi}{M}}. \tag{5.5}$$

Table 5.1: Bearing geometrical dimensions, rotor mass, and remanent magnetization.

parameter	value	unit
R_i	2	mm
R_m	18	mm
R_w	19	mm
R_a	21	mm
L	70	mm
M	2	kg
B_{rem}	1.32	T

As an illustration, let us draw the root locus of a system in the absence of damping ($C = 0$). The parameters of the bearing are given in Table 5.1. The permanent magnet magnetization pattern is parallel with $p = 1$. The winding has two pole pairs and three phases.

The root locus is shown in Fig. 5.1 for different speeds ω and yoke materials. It highlights a central symmetry of the roots with respect to the origin, whatever the material of the yoke. Therefore, one of the two roots of the system is always on the right-hand side of the plane i.e., its real part is positive. This indicates that the bearing is always unstable when no damping is added in the system, which corresponds to expectations. As ω increases, the unstable root approaches the stability region on the left-hand side of the plane and $|\Re\{\rho\}| \ll |\Im\{\rho\}|$, see the region in the red square in Fig. 5.1. Let us focus on the behaviour of the unstable root in this region. The unstable root corresponds to the plus sign in (5.5):

$$\rho = \frac{-C}{2M} + \sqrt{\left(\frac{C}{2M}\right)^2 - \frac{K_\epsilon + jK_\phi}{M}}. \tag{5.6}$$

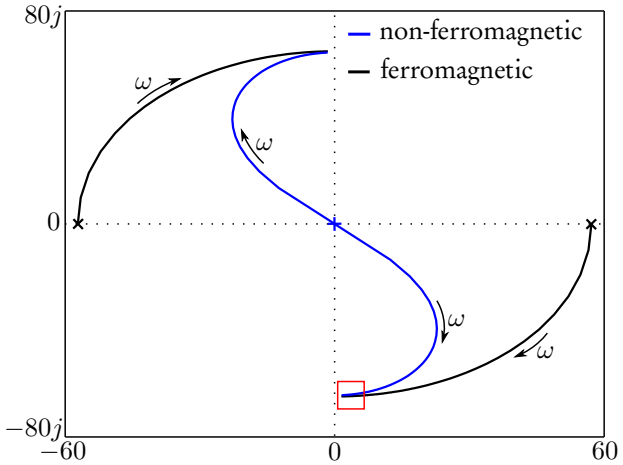

Fig. 5.1: Root locus for $\omega \in [0, 2\pi 5000]$ and $C = 0$. The arrows show the direction of increasing ω.

Using the polar form for complex numbers:

$$\frac{K_\epsilon + jK_\phi}{M} = Ne^{j\alpha}, \tag{5.7}$$

where:

$$\tan(\alpha) = \frac{K_\phi}{K_\epsilon} \tag{5.8}$$

$$N = \frac{\sqrt{K_\epsilon^2 + K_\phi^2}}{M}. \tag{5.9}$$

The root locus is drawn for $C = 0$. Therefore, (5.6) and (5.7) yield[1]:

$$\rho|_{C=0} = -j\sqrt{N}e^{j\alpha/2}. \tag{5.10}$$

This expression corresponds to the $K_\phi > 0$ case, hence the minus sign. The $K_\phi < 0$ case yields a plus sign, and the corresponding developments are presented in appendix E. In the area of interest of the root locus:

$$\left|\frac{\Re\{\rho|_{C=0}\}}{\Im\{\rho|_{C=0}\}}\right| = \tan\left(\left|\frac{\alpha}{2}\right|\right) \ll 1. \tag{5.11}$$

[1]In each of these cases, only the principal square root of $\rho|_{C=0}$ is considered, following the convention that is used in matlab.

As a result, $|\alpha/2| \ll 1$ which can be approximated as $|\alpha| \ll 1$. Considering this, (5.8) and (5.9) yield:

$$\alpha \cong \frac{K_\phi}{K_\epsilon} \ll 1 \Rightarrow \left|\frac{K_\phi}{K_\epsilon}\right| \ll 1 \tag{5.12}$$

$$N \cong \frac{K_\epsilon}{M}. \tag{5.13}$$

A consequence of $|\alpha| \ll 1$ is that $\sin(\alpha/2) \cong \alpha/2$ and $\cos(\alpha/2) \cong 1$. Therefore, (5.10) becomes:

$$\rho|_{C=0} = -j\sqrt{N}\left(\cos\left(\frac{\alpha}{2}\right) + j\sin\left(\frac{\alpha}{2}\right)\right) \cong \sqrt{N}\left(\frac{\alpha}{2} - j\right). \tag{5.14}$$

Replacing (5.12) and (5.13) in (5.14) yields:

$$\rho|_{C=0} \cong \sqrt{\frac{K_\epsilon}{M}}\left(\frac{K_\phi}{2K_\epsilon} - j\right) = \sqrt{\frac{K_\epsilon}{M}}\frac{K_\phi}{2K_\epsilon} - j\sqrt{\frac{K_\epsilon}{M}}. \tag{5.15}$$

Let us consider the effect of damping. Assuming a priori that the damping introduced in the system satisfies:

$$\left(\frac{C}{2M}\right)^2 \ll \frac{K_\epsilon}{M}, \tag{5.16}$$

(5.6) yields:

$$\rho \cong \frac{-C}{2M} + \sqrt{-\frac{K_\epsilon + jK_\phi}{M}}. \tag{5.17}$$

Combining this with (5.15) gives:

$$\rho \cong \frac{-C}{2M} + \sqrt{\frac{K_\epsilon}{M}}\frac{K_\phi}{2K_\epsilon} - j\sqrt{\frac{K_\epsilon}{M}}. \tag{5.18}$$

In this formula, the imaginary part of ρ is $-\sqrt{K_\epsilon/M}$. It reflects the stiffness associated with the centering force on the rotor of the bearing. Therefore, the vertical position of ρ in the root locus is an image of the bearing stiffness. Besides, the damping C only impacts the real part of ρ. To achieve stabilization, the damping should be increased to satisfy $\Re\{\rho\} < 0$.

From this and (5.18), the minimum amount of damping to stabilize the bearing is obtained:

$$\frac{C_s}{2M} = \sqrt{\frac{K_\epsilon}{M}} \left(\frac{K_\phi}{2K_\epsilon} \right). \tag{5.19}$$

This result is consistent with (Davey et al., 2005; Post, 2000), and shows that the horizontal position of $\rho|_{C=0}$ in the root locus is proportional to the level of instability of the bearing. Furthermore, considering (5.12), (5.19) yields:

$$\left| \frac{C_s}{2M} \right| \ll \sqrt{\frac{K_\epsilon}{M}}, \tag{5.20}$$

which confirms assumption (5.16). Finally, (5.19) shows that the amount of damping to reach stability decreases with the natural frequency associated with the bearing stiffness, and increases with the parasitic stiffness K_ϕ.

In summary, the radial stiffness and the instability margin are linked to the unstable root locus through:

$$\begin{aligned} \Re\{\rho|_{C=0}\} &= \frac{C_s}{2M} \\ \Im\{\rho|_{C=0}\} &= -\sqrt{\frac{K_\epsilon}{M}}, \end{aligned} \tag{5.21}$$

where:

$$C_s = K_\phi \sqrt{\frac{M}{K_\epsilon}}. \tag{5.22}$$

5.1.2 Rotordynamics analogy

Let us reformulate the previous results using the notations commonly used in rotordynamics. When studying a bearing with a quasi-static model, the rotor motion is governed by (5.2), i.e.:

$$M\ddot{z} + C\dot{z} + (K_\epsilon + jK_\phi)z = 0, \tag{5.23}$$

where C is the amount of external non-rotating damping. In the field of rotor dynamics, the equation governing the free motion of a perfectly balanced Jeffcott rotor in presence of rotating and non-rotating damping is:

$$M\ddot{z} + (C_r + C_n)\dot{z} + (K_{jeff} - j\omega C_r)z = 0, \tag{5.24}$$

where K_{jeff} is the stiffness, and C_r and C_n are the amounts of rotating and non-rotating damping, respectively (Genta, 2005). The corresponding equivalent mechanical model is shown in Fig. 5.2.

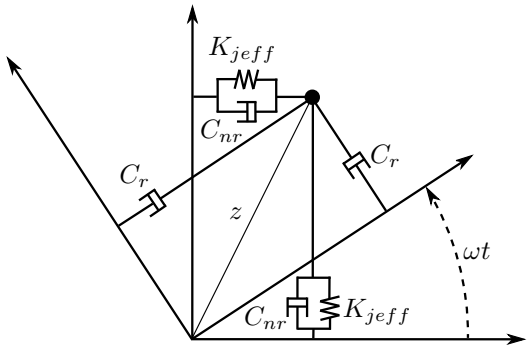

Fig. 5.2: Equivalent mechanical model of a perfectly balanced Jeffcott rotor in presence of rotational and non-rotational damping.

Looking at the coefficients of (5.23) and (5.24), it appears that the rotor governed by (5.23) behaves in the same way as the Jeffcott rotor if:

$$\begin{aligned} K_{jeff} &= K_\epsilon \\ C_r &= -\frac{K_\phi}{\omega} \\ C_n &= C + \frac{K_\phi}{\omega}. \end{aligned} \tag{5.25}$$

Finally, the equivalent mechanical model of an EDB in the absence of external non-rotating damping is shown in Fig. 5.3. The model parameters depend on the rotor spin speed ω.

5.2 Bearing comparison

In section 5.1, a graphical method for evaluating the performance criteria of EDBs was presented. This section applies this method to the study of the impact of the yoke material on the performance of EDBs. In this aim, the performance of two EDBs with the same topology, but different yoke permeabilities are compared.

This section is organized as follows. First, the bearing topology that is studied in this section is presented. Then, a field model adapted to this topology is derived.

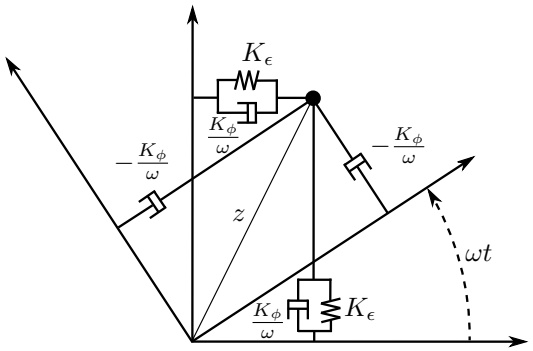

Fig. 5.3: Parameters of the Jeffcott rotor model yielding the dynamics of the EDB predicted with a quasi-static model.

This model is aimed at calculating the parameters of the lumped-parameter model (5.3), i.e. K_ϵ and K_ϕ. From this, the root locus of bearings with different yoke materials is obtained, and their performance are compared.

5.2.1 Case study

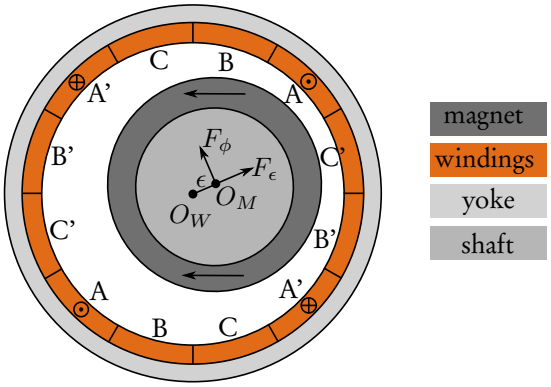

Fig. 5.4: Bearing topology with $p = 1, q = 2$, and three phases denoted A, B and C.

The presence of a ferromagnetic yoke in front of the permanent magnets has the two following effects. On the one hand, it increases the magnetic flux density in the airgap and the magnitude of the centering electrodynamic forces between the rotor and the stator of the device. This is positive since the stiffness associated with the centering force of the bearing increases too. On the other hand, it also induces a negative stiffness due to the detent force between the yoke and the magnets.

Let us study the impact of the yoke permeability on the performance of the bearing shown in Fig. 5.4. It comprises an internal rotor with a ferromagnetic shaft and

permanent magnets creating a heteropolar radial magnetic field with p pole pairs in the airgap. The stator is external and comprises a short-circuited axial airgap winding with $q = p + 1$ pole pairs and N phases, and a yoke that can be made of a ferromagnetic material or not. Figure 5.4 shows a bearing with $p = 1, q = 2$, and $N = 3$. As shown in chapter 3, verifying identity $q = p+1$ ensures that the winding is null-flux and that it can interact with the permanent magnets to create a radial centering force.

5.2.2 Field model

Parameters and variables

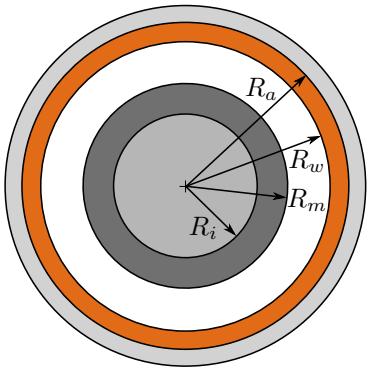

Fig. 5.5: Dimensional parameters of the bearing. The airgap width is exaggerated.

The dimensional parameters of the bearing are given in Fig. 5.5, whereas the rotor position variables are shown in Fig. 5.6. The rotor center is O_M, the stator center is O_W, and the axes $x - y$ are attached to the stator. The position of the rotor and the position of a point P in the stator frame are given by coordinates (ϵ, ϕ) and (r, θ), respectively. The rotor spins around its axis at speed ω.

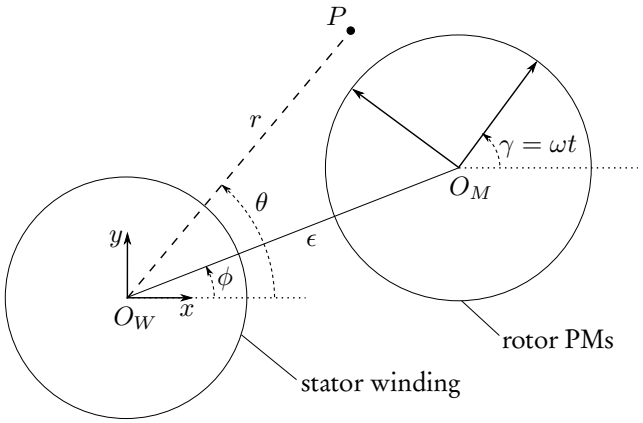

Fig. 5.6: Coordinates systems of the model.

Assumptions

In this section, the following assumptions are made:

1. the end effects are not considered and the problem is assumed to be two-dimensional;
2. the permanent magnets work in the linear range of their magnetic characteristic, the rotor shaft is made of a ferromagnetic material with infinite magnetic permeability, and the winding and the permanent magnets have the same magnetic permeability as air. The magnetic permeability of the yoke is either infinite (ferromagnetic yoke) or the same as air;
3. eddy current losses in the magnets and ferromagnetic parts are neglected;
4. the amplitude of the off-centering ϵ is small compared to the nominal airgap of the bearing;
5. the spin speed ω is constant;
6. the model is quasi-static i.e., the assumption (2.3) is made;
7. the inductances of the winding are constant and do not change with the rotor position;
8. the rotor mechanical model is that of a point mass with two radial degrees of freedom.

Force calculation

As a recall, this model aims at calculating the stiffnesses K_ϵ and K_ϕ. For this purpose, the electromagnetic forces between the rotor and the stator of the bearing are calculated using the Maxwell stress tensor. This requires the expression of the magnetic field created by the permanent magnets and by the phase currents. As stated in chapter 3, the eddy current in each short-circuited phase is governed by:

$$RI_k + L_c \frac{dI_k}{dt} = -\frac{d\Phi_k}{dt} = emf_k, \tag{5.26}$$

where R and L_c are the phase resistance and cyclic inductance, respectively. They are identical for all the phases. Φ_k is the flux from the permanent magnets linked by phase k, and emf_k is the induced electromotive force. From chapter 3, the flux Φ_k is given by:

$$\Phi_k = L \int_{R_w}^{R_a} \int_0^{2\pi} A_{Mz}(r,\theta) D_k(r,\theta) r d\theta dr, \tag{5.27}$$

where:

$$A_{Mz}(r,\theta) = \sum_{n,odd}^{\infty} \Big\{ C_n(r)\sin\left(np(\theta-\gamma)\right) + \epsilon\hat{C}_n(r)\sin\left(\left(np+1\right)\theta - np\gamma - \phi\right) + \epsilon\check{C}_n(r)\sin\left(\left(np-1\right)\theta - np\gamma + \phi\right) \Big\}, \tag{5.28}$$

is the vector potential created by the permanent magnets, L is the axial length of the bearing, and $D_k(r,\theta)$ is the conductor density of phase k:

$$D_k(r,\theta) = \frac{2Nqb(-1)^v}{\pi|R_a^2 - R_w^2|} \text{ if } \begin{cases} r \in [R_w, R_a] \\ \theta \in \left[\delta_k + \frac{\pi(N-1)}{2Nq} + \frac{\pi v}{q}, \delta_k + \frac{\pi(N+1)}{2Nq} + \frac{\pi v}{q}\right] \end{cases}$$
$$= 0 \qquad \text{elsewhere.} \tag{5.29}$$

In this expression, δ_k is the angular position of phase k, N is the number of phases, b is the number of winding turns per phase, and:

$$\begin{aligned} v &\in \{0; 2q-1\} \\ k &\in \{0; N-1\} \\ \delta_k &= \frac{\pi k}{qN}. \end{aligned} \tag{5.30}$$

When $r \in [R_w, R_a]$, the Fourier development of this function is:

$$D_k(r,\theta) = \sum_{m,odd}^{\infty} \frac{8bNq}{\pi^2 m|R_a^2 - R_w^2|} \sin\left(\frac{m\pi}{2}\right) \sin\left(\frac{m\pi}{2N}\right) \sin\left(mq\left(\theta - \delta_k\right)\right). \tag{5.31}$$

As an example, the function $D_k(r,\theta)$ of the phase A of the bearing from Fig. 5.4 is shown in Fig. 5.7.

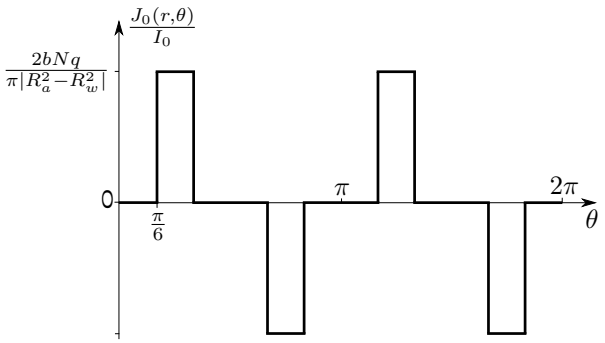

Fig. 5.7: Function $D_k(r,\theta)$ in the case of an axial winding with two pole pairs.

Because $q = p+1$, only the terms with coefficients $\hat{C}_n$ and $\check{C}_n$ in (5.28) can give a non-zero contribution to the flux Φ_k, as exposed in chapter 3. The amplitude of Φ_k is thus proportional to ϵ, as well as the corresponding electromotive forces emf_k. Considering the sixth assumption from section 5.2.2, it is calculated as:

$$\begin{aligned} emf_k &= -\frac{d\Phi_k}{dt} \\ &= -\frac{\partial\Phi_k}{\partial\gamma}\omega - \frac{\partial\Phi_k}{\partial\phi}\frac{d\phi}{dt} - \frac{\partial\Phi_k}{\partial\epsilon}\frac{d\epsilon}{dt} \\ &\cong -\frac{\partial\Phi_k}{\partial\gamma}\omega \\ &\cong \sum_{m,odd}^{\infty}\Big\{\epsilon\hat{E}_m\sin\left((mq-1)\gamma - mq\delta_k + \phi\right) \\ &\qquad + \epsilon\check{E}_m\sin\left((mq+1)\gamma - mq\delta_k - \phi\right)\Big\}. \end{aligned} \tag{5.32}$$

In this expression, $\hat{E}_m$ and $\check{E}_m$ are related to the constants in (5.28) as follows:

$$\begin{aligned} \hat{E}_m &= \frac{8bNqL}{\pi m|R_a^2-R_w^2|}\sin\Big(\frac{m\pi}{2}\Big)\sin\Big(\frac{m\pi}{2N}\Big)(mq-1)\omega\int_{R_w}^{R_a}\hat{C}_n(r)rdr \\ \check{E}_m &= \frac{8bNqL}{\pi m|R_a^2-R_w^2|}\sin\Big(\frac{m\pi}{2}\Big)\sin\Big(\frac{m\pi}{2N}\Big)(mq+1)\omega\int_{R_w}^{R_a}\check{C}_n(r)rdr. \end{aligned} \tag{5.33}$$

Knowing (5.32), the current I_k can be calculated by solving (5.26), which yields:

$$I_k = \sum_{m,odd}^{\infty} \left\{ \epsilon \hat{E}_m \frac{\sin\left((mq-1)\gamma - mq\delta_k + \phi - \hat{\varphi}_m\right)}{\sqrt{R^2 + ((mq-1)\omega L_c)^2}} + \epsilon \check{E}_m \frac{\sin\left((mq+1)\gamma - mq\delta_k - \phi - \check{\varphi}_m\right)}{\sqrt{R^2 + ((mq+1)\omega L_c)^2}} \right\}, \tag{5.34}$$

where the phase differences between emf_k and I_k are:

$$\begin{aligned} \hat{\varphi}_m &= atan\left(\frac{(mq-1)\omega L_c}{R}\right) \\ \check{\varphi}_m &= atan\left(\frac{(mq+1)\omega L_c}{R}\right). \end{aligned} \tag{5.35}$$

The previous reasoning can be repeated for each winding phase. Once the current in every phases is known, the magnetic field created by this current in the airgap is found by solving Maxwell's equations. This was done by Atallah et al. (1998) in the case of a slotless motor with a ferromagnetic yoke. This solution is re-used in the present model, and a similar approach was followed to derive the solution of Maxwell's equations in the non-ferromagnetic yoke case, see appendix F. For the axial winding shown in Fig. 5.4, the general expression of the magnetic vector potential created by a single winding phase is:

$$A_{Iz,k}(r,\theta) = \sum_{m,odd}^{\infty} I_k K_{I,m}(r) \sin\left(mq(\theta - \delta_k)\right), \tag{5.36}$$

where $K_{I,m}(r)$ depends on the magnetic properties and dimensional parameters of the bearing (Atallah et al., 1998). The potential A_{Iz} created by the induced currents is obtained by summing the contributions of all phases. The total magnetic vector potential B_{tot} in the airgap is the sum of the magnetic field from the windings and from the rotor magnets:

$$\mathbf{B}_{tot} = \mathbf{B}_M + \mathbf{B}_I = \nabla \times \mathbf{A}_M + \nabla \times \mathbf{A}_I. \tag{5.37}$$

Finally, the force between the rotor and the winding is obtained by integrating Maxwell's stress tensor in the airgap. This yields the force components acting on the rotor in the direction of the off-centering and in the direction perpendicular to it F_ϵ and F_ϕ, see Fig. 5.4:

$$
\begin{aligned}
F_\epsilon &= \int_0^{2\pi} \left\{ \frac{1}{2\mu_0} \left(B_{tot,r}^2 - B_{tot,\theta}^2 \right) \cos(\theta - \phi) \right. \\
&\qquad \left. - \frac{B_{tot,r} B_{tot,\theta}}{\mu_0} \sin(\theta - \phi) \right\} L r d\theta \\
F_\phi &= \int_0^{2\pi} \left\{ \frac{1}{2\mu_0} \left(B_{tot,r}^2 - B_{tot,\theta}^2 \right) \sin(\theta - \phi) \right. \\
&\qquad \left. + \frac{B_{tot,r} B_{tot,\theta}}{\mu_0} \cos(\theta - \phi) \right\} L r d\theta,
\end{aligned}
\tag{5.38}
$$

where $B_{tot,r}$ and $B_{tot,\theta}$ are the radial and azimuthal components of the airgap field, respectively. Finally, F_ϵ and F_ϕ are directly proportional to ϵ and can be associated with stiffnesses through:

$$
\begin{aligned}
F_\epsilon &= -K_\epsilon \epsilon \\
F_\phi &= -K_\phi \epsilon.
\end{aligned}
\tag{5.39}
$$

These forces may be pulsating and induce vibrations. However, this effect can be made negligible by increasing the number of phases (chapter 3). In the next sections, the pulsating component is neglected compared to the time average forces, and the associated stiffnesses are constants.

5.2.3 Results and discussion

Using the method exposed in section 5.1, let us compare two bearings with and without ferromagnetic yoke in terms of radial stiffness and instability margin. Both bearings have the same dimensional and magnetic parameters as in the previous sections, except that R_i and R_a can change, see Fig. 5.5.

The selection process for the best bearing is the following. The bearings have to provide a minimum stiffness when operating above a given threshold speed. Then, the best bearing is the one requiring the less damping to reach stability.

Fig. 5.8 shows a zoom on the area of interest of the root locus. The dotted lines correspond to a fixed speed ω and an increasing radius R_a. They give the minimum operating speed of the two bearings so that the area of interest with $\omega > 2\pi 500$ rad/s is below these curves. The solid lines correspond to a fixed radius $R_a = 24$ mm and an increasing speed ω. The evolution of the bearing properties with speed can thus be observed by following these solid lines in the region above the threshold speed. The performance of a bearing for a given set of parameters (R_a, ω) is obtained by looking at the crossing points between the corresponding dotted and solid lines. For example, two such points for ($R_a = 24$ mm, $\omega = 2\pi 500$ rad/s) are in the red circle of Fig. 5.8. For this set of parameters, the bearing with a ferromagnetic yoke has

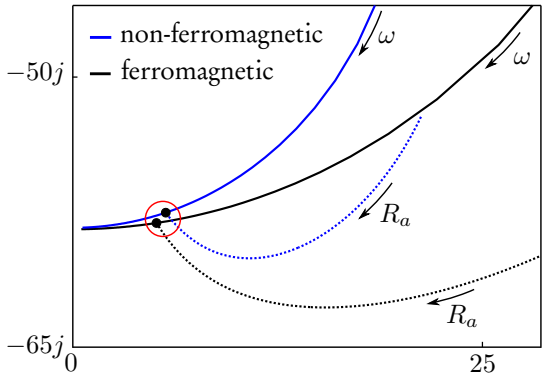

Fig. 5.8: Unstable poles in the area of interest of the root locus for $C = 0$ Ns/m and $R_i = 2$ mm. The dotted and solid lines correspond to a fixed speed $\omega = 500$ rad/s and to a fixed radius $R_a = 24$ mm, respectively.

a better stiffness since its root has a greater imaginary part (in absolute value), see (5.21). This bearing also has a lower instability margin since its root has a lower real part, see (5.21). Looking at Fig. 5.8, it is clear that the bearing performance improves with speed, whatever the yoke material.

In order to see the evolution of the previous results with ω and R_a, more data is needed, as shown in Fig. 5.9. This was obtained for different rotor shaft radii $R_i = 0$ mm and 10 mm. From Fig. 5.9 (a), it appears that the yoke material does not have a significant influence on the bearing stiffness and stability in the area of interest when $R_i = 0$ mm. E.g. for $R_a = 24$ mm, a bearing without ferromagnetic yoke has a better stiffness but is less stable than a bearing with a ferromagnetic yoke, but the differences are not very significant. However, these differences increase with R_i as shown in Fig. 5.9 (b). Comparing the corresponding points for each kind of yoke, it appears that the bearing with a ferromagnetic yoke has a significantly greater stiffness but is less stable, especially at low speed. Finally, the stiffness of the two kinds of bearing decrease with R_i, which is consistent with intuition since the amount of permanent magnet decreases with R_i.

Fig. 5.10 shows the same data than Fig. 5.9, except that the pole pairs number of the rotor and of the winding are $p = 2$ and $q = 3$. The permanent magnets still have a parallel magnetization pattern. Looking at Fig. 5.10 (a), it appears that the stiffnesses of the bearings are improved but the differences between the bearings with and without ferromagnetic yoke remain small and the situation is similar to Fig. 5.9 (a). Fig. 5.10 (b) shows that increasing the shaft radius R_i is less favourable for the bearing without ferromagnetic yoke, but the difference between Fig. 5.10 (a) and (b) is much smaller than the difference between Fig. 5.9 (a) and (b). Last but not

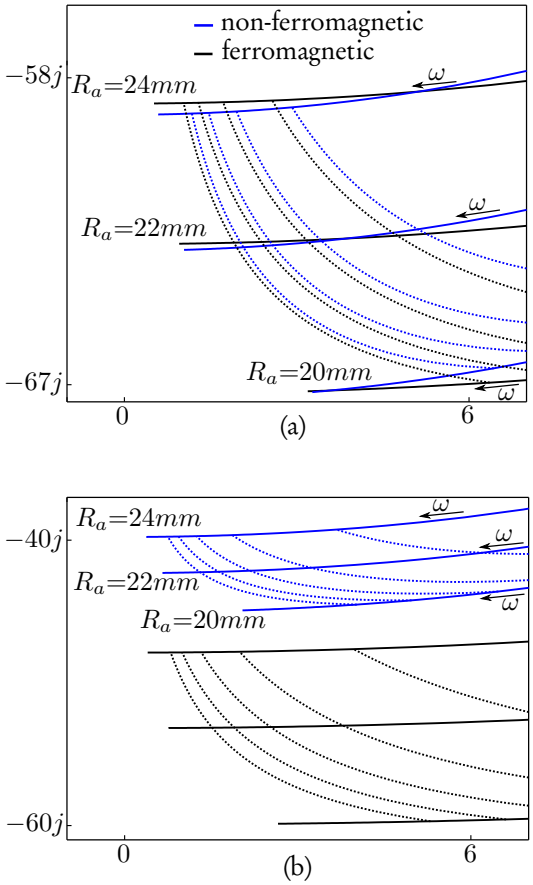

Fig. 5.9: Root loci of the bearings without damping, with $p = 1$. (a) $R_i = 0$ mm. (b) $R_i = 10$ mm.

least, the bearing with a ferromagnetic yoke has a lower stiffness than the bearing without ferromagnetic yoke when $R_a = 20$ mm i.e., when the yoke is close to the permanent magnets. This is due to the higher order harmonics in the permanent magnet field. They contribute to the negative stiffness associated with the reluctant force between the permanent magnets and the ferromagnetic yoke, but they do not contribute to the centering electrodynamic force between the permanent magnets and the winding. This effect cancels as R_a increases and is not observed with $p = 1$ because there is no higher order harmonics in the permanent magnet field in this case.

5.2.4 Quasi-static assumption

Finally, let us take a step back and analyze the validity of the quasi-static assumption made in sections 5.1 and 5.2. Indeed, this assumption results in neglecting the

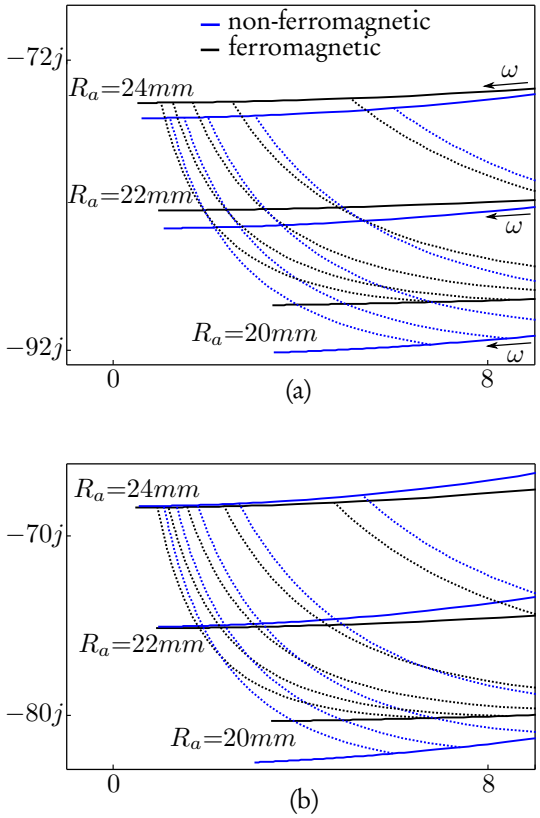

Fig. 5.10: Root loci of the bearing without damping, $p = 2$ and (a) $R_i = 0$ mm or (b) $R_i = 10$ mm.

contributions of the terms in $\frac{d\phi}{dt}$ and $\frac{d\epsilon}{dt}$ when calculating the electromotive force, see (5.32). To support this, let us consider the bearing whose root locus is shown in Fig. 5.1. The yoke is ferromagnetic, and there is no external damping. The bearing model parameters are given in Table 5.2.

Table 5.2: Parameters of the dynamic model of the bearing.

parameter	value	unit	definition
R	2.23	Ω	winding phase resistance
L_c	2.7	mH	winding cyclic inductance
M	2	kg	rotor mass
K_Φ	26	$(\mathrm{Ns}\Omega/\mathrm{m})^{1/2}$	flux constant
C	0	Ns/m	external non rotating damping
K_d	−164	kN/m	detent stiffness

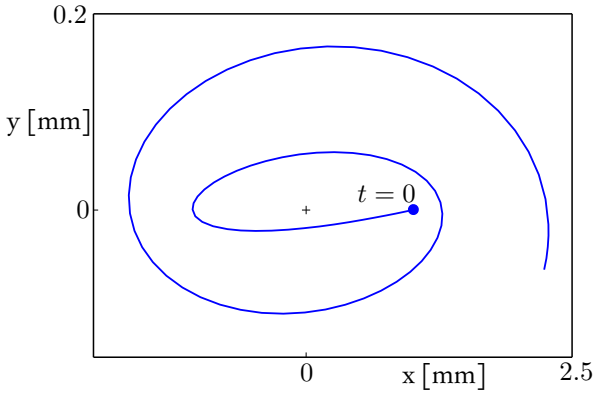

Fig. 5.11: Trajectory of the bearing rotor in the absence of external forces and without damping.

Considering an initial off-centering of 10% of the nominal airgap and a spin speed of $\omega = 2\pi 1000$ rad/s, the trajectory of the rotor moving freely during 0.04 s is simulated, see Fig. 5.11. From this data, the values of $\frac{d\phi}{dt}$ and $\frac{d\epsilon}{dt}$ are calculated and the rms amplitude of the different contributions to the emf are obtained, see Fig. 5.12. It appears that the contribution of the term in ω is approximately two orders of magnitude larger than the others which confirms the approximation in (5.32).

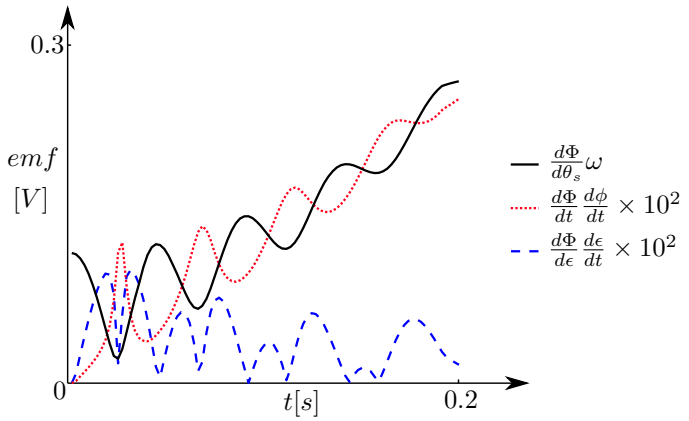

Fig. 5.12: Evolution of the amplitude of the different contributions to the electromotive force.

The previous results show that the static-eccentricity assumption is valid to predict the rotor motion in the absence of external forces. This is due to the low bearing stiffness that results in a slow rotor motion. For other kinds of rotor motion, showing the accuracy of the graphical approach presented in section 5.1 thus requires additional validations. Indeed, the system roots are the eigenvalues of the dynamic matrix (5.4), and therefore the information provided by a root locus (e.g. the system

stability) depends neither on the external forces nor on the rotor motion.

Let us further validate the graphical approach of section 5.1. In this aim, the roots, the radial stiffness, and the instability margin of the bearing considered above in this section are calculated in three different ways and compared. The first way involves the dynamic approach (4.47) from chapter 4, where the roots are calculated as the eigenvalues of the system dynamic matrix:

$$\mathbf{A} = \begin{bmatrix} -\frac{R}{L_c} - j\omega_e & -K_d - \frac{K_\Phi^2 N}{2L_c} & -\frac{RK_d}{L_c} - j\omega_e K_d - j\frac{\omega_e K_\Phi^2 N}{2L_c} \\ \frac{1}{M} & -\frac{C}{M} & 0 \\ 0 & 1 & 0 \end{bmatrix}. \tag{5.40}$$

In this case, the instability margin C_s is the value of damping C such that the unstable root of the system crosses the imaginary axis, whereas the bearing radial stiffness is (5.1):

$$K_\epsilon = K_d + \frac{\omega_e^2 K_\Phi^2 L_c N}{2\left(R^2 + (\omega_e L_c)^2\right)}. \tag{5.41}$$

This last expression of the stiffness is identical in all three ways. The second way involves the quasi-static approach without approximation (5.5) from section 5.1, where:

$$\rho_{1,2} = \frac{-C}{2M} \pm \sqrt{\left(\frac{C}{2M}\right)^2 - \frac{K_\epsilon + jK_\phi}{M}}. \tag{5.42}$$

Again, the instability margin C_s is the value of damping C such that the unstable root of the system ρ_1 crosses the imaginary axis. Finally, the third way involves the approximated quasi-static approach (5.18), where:

$$\rho_{1,2} \cong \frac{-C}{2M} \pm \sqrt{\frac{K_\epsilon}{M}}\frac{K_\phi}{2K_\epsilon} \mp j\sqrt{\frac{K_\epsilon}{M}}. \tag{5.43}$$

In this case, the unstable root ρ_1 has a negative real value when:

$$C_s = K_\phi \sqrt{\frac{M}{K_\epsilon}}. \tag{5.44}$$

The resulting root loci are shown in Fig. 5.13. As shown in Fig. 5.13 (a), the dynamic model yields three roots while the other models yield only two of them. However, only one root is unstable in the three cases. Besides, some of the roots

of the quasi-static, approximated model are scattered and clearly inaccurate. They correspond to low values of ω, such that the assumption of this model:

$$\left| \frac{\Re\{\rho|_{C=0}\}}{\Im\{\rho|_{C=0}\}} \right| \ll 1 \tag{5.45}$$

does not hold anymore. Figure 5.13 (b) shows an enlarged view in the vicinity of the unstable root of the root locus, at speeds that are consistent with the assumption (5.45). As the assumption (5.45) is better satisfied, the roots of the quasi-static models get closer to the reference roots obtained with the dynamic model, which is coherent. This validates the use of the quasi-static models to calculate the system roots. Let us validate the graphical approach itself i.e., the link between the position of the roots $\Re\{\rho\}$ and $\Im\{\rho\}$ and the performance criteria C_s and K_ϵ, see (5.21).

As shown in Fig. 5.14 (a) and (b), these sets of data agree well for all three models. This improves as (5.45) is satisfied, and validates the graphical approach presented in section 5.1. In practice, the dynamic model will be preferred to the quasi-static models when studying a bearing because it removes the static-eccentricity assumption. Therefore, showing that the link between the root position and the performance criteria of the bearing which was derived from a quasi-static model can be used to interpret the root loci obtained with the dynamic model constitutes the main result of the present validation. This is reflected in the close agreement between the two sets of data corresponding to the dynamic model in Fig. 5.14 (a) and (b).

5.3 Bearing optimization

Let us use the tools developed in the previous sections to optimize a yokeless bearing, i.e. a bearing without ferromagnetic yoke.

First, this section presents the bearing topology that is optimized. As opposed to the previous section, the quasi-static assumption is removed, and an alternate way to evaluate the bearing performance using the dynamic model from chapter 4 is exposed. Finally, the optimization yields a Pareto front of optimal bearings that are compared to existing EDBs in terms of stiffness to permanent magnet volume ratio.

5.3.1 Case study

The bearing to be optimized is shown in Fig. 5.15. The rotor magnets have one pole pair and the shaft iron is ferromagnetic. The winding has three phases and two pole pairs in order to have the null-flux characteristic, see Fig. 5.15 (b). The properties of the bearing materials are given in Table 5.3.

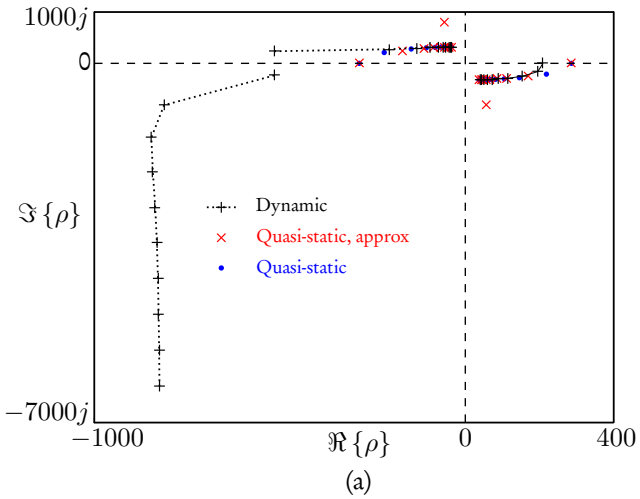

(a)

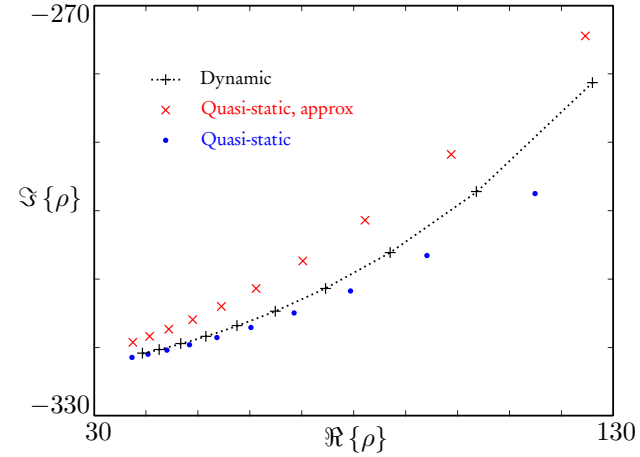

(b)

Fig. 5.13: Root loci at zero damping ($C = 0$) obtained in three different ways. (a) Root loci for $\omega = 2\pi[0, 1000]$ rad/s. (b) Enlarged view in the vicinity of the unstable root for $\omega = 2\pi[300, 1000]$ rad/s.

Let us optimize this bearing with regard to two objectives: the radial stiffness and the instability margin.

5.3.2 Performance evaluation

Let us recall the electromechanical model from chapter 4. The position of the rotor and the electrodynamic forces are:

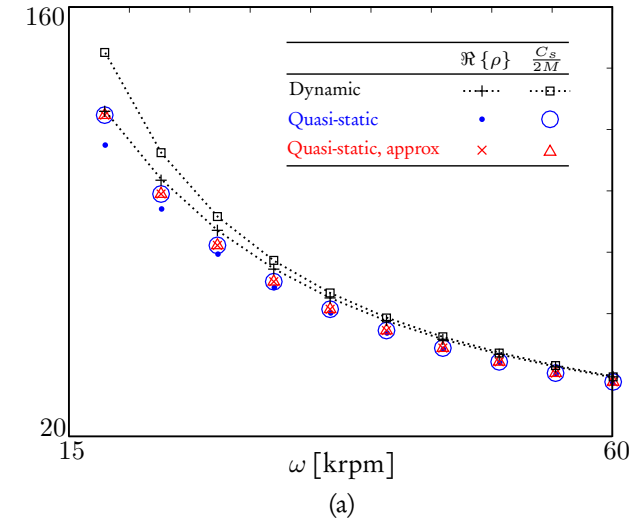

(a)

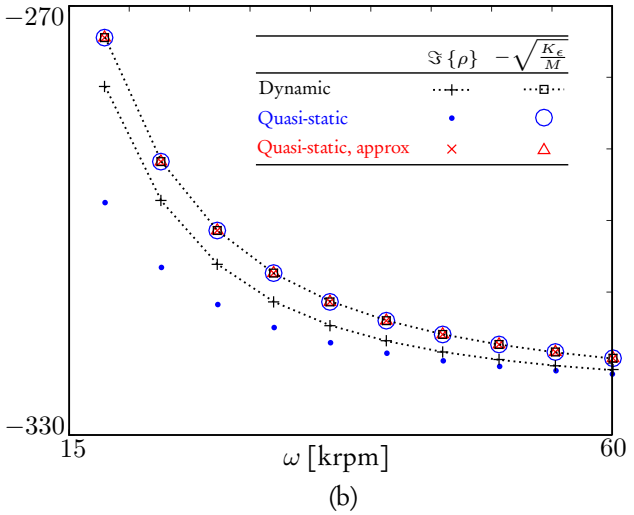

(b)

Fig. 5.14: Unstable roots for $\omega = 2\pi[300, 1000]$ rad/s. (a) Real part and predicted instability margin C_s. (b) Imaginary part and predicted stiffness K_ϵ.

$$z = x + jy, \tag{5.46}$$

$$F = F_x + jF_y. \tag{5.47}$$

They are linked with the external input force F_e through:

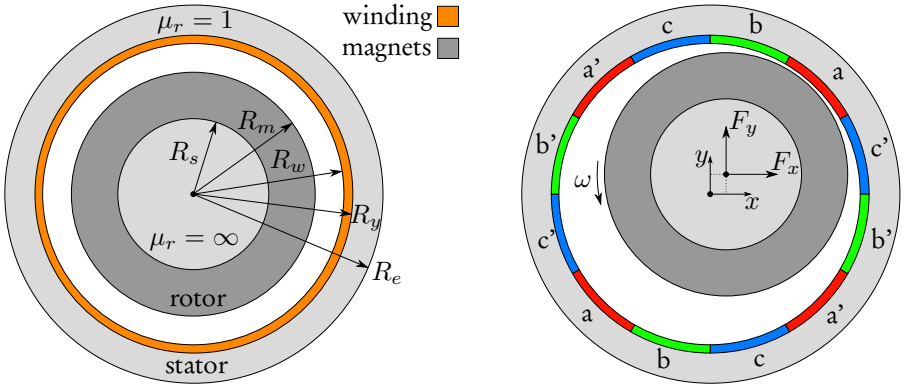

Fig. 5.15: (a) Bearing topology and design parameters. (b) Rotor position, electrodynamic forces and winding phases.

Table 5.3: Bearing material properties.

parameter	value	unit	definition
B_r	1.2	T	remanent magnetization
ρ_m	7500	kg/m^3	specific mass of the NdFeB magnets
ρ_s	7800	kg/m^3	specific mass of the shaft iron
σ_{cu}	$6e7$	$(\Omega\ \mathrm{m})^{-1}$	copper conductivity
μ_s	∞	/	relative magnetic permeability of the shaft iron
μ_r	1	/	relative magnetic permeability of the conductors, the magnets, and the stator yoke

$$\begin{bmatrix} \dot{F} \\ \ddot{z} \\ \dot{z} \end{bmatrix} = A \begin{bmatrix} F \\ \dot{z} \\ z \end{bmatrix} + BF_e \tag{5.48}$$

where the dynamic and input gain matrices are:

$$\mathbf{A} = \begin{bmatrix} -\frac{R}{L_c} - j\omega_e & -K_d - \frac{K_\Phi^2 N}{2L_c} & -\frac{RK_d}{L_c} - j\omega_e K_d - j\frac{\omega_e K_\Phi^2 N}{2L_c} \\ \frac{1}{M} & -\frac{C}{M} & 0 \\ 0 & 1 & 0 \end{bmatrix} \tag{5.49}$$

$$\mathbf{B} = \frac{1}{M}\begin{bmatrix} 0 & 1 & 0 \end{bmatrix}^T. \tag{5.50}$$

The parameters of (5.49)-(5.50) are given in Table 5.4. As the bearing is studied in 2D, all the parameters and performance criteria are evaluated per unit of active bearing length. The parameters R, L_c, and K_Φ are identified using the field model

presented in section 5.2.2. In particular, K_Φ is the ratio of the peak permanent magnet flux linkage in a winding phase to the amplitude of the rotor eccentricity $\epsilon = (x^2 + y^2)^{1/2}$. The rotor is assumed to weigh three times the weight of its active length. Therefore, its mass per unit length is:

$$M = 3\left[\rho_m \pi (R_m^2 - R_s^2) + \rho_s \pi R_s^2\right], \tag{5.51}$$

where ρ_m and ρ_s are given in Table 5.3. Lastly, the spin speed ω and the damping C are set arbitrarily.

Table 5.4: Parameters of the dynamic model.

parameter	unit	definition
R	Ω/m	winding phase resistance
L_c	H/m	winding cyclic inductance
M	kg/m	rotor mass
K_Φ	$(\mathrm{Ns}\Omega/\mathrm{m}^3)^{1/2}$	flux constant
C	$\mathrm{Ns/m}^2$	external non rotating damping
ω	rad/s	rotor spin speed

From these parameters, the two bearing performance criteria can be calculated. The bearing radial stiffness in static-eccentricity configuration is given by (5.1). In the present case, this yields:

$$K_\epsilon = \Re\left\{\frac{F}{z}\right\}\Big|_{\dot{z}=0,\ddot{z}=0,\dot{F}=0} = \frac{3\omega^2 L_c K_\Phi^2}{2\left(R^2 + (\omega L_c)^2\right)}. \tag{5.52}$$

Lastly, the damping required for stabilization C_s is obtained by increasing the value of C until the three eigenvalues of (5.49) cross the imaginary axis.

5.3.3 Optimization problem formulation

The bearing was optimized using a genetic algorithm. From this, a Pareto front defining the area of feasible choices is obtained. The two objective functions K_ϵ and C_s are optimized at a given spin speed ω. Defining the variables of the optimization problem:

$$x_1, x_2 \in [0, 1], \tag{5.53}$$

the constraints on the geometric parameters can be formulated as (in meters):

$$\begin{aligned} R_m &= x_1 R_{m,max} \\ R_s &= 0.4 R_m \\ R_w &= R_m + 0.0015 \\ R_y &= R_w + x_2(0.6 R_{m,max}) \end{aligned} \tag{5.54}$$

The maximum rotor radius $R_{m,max}$ is obtained by considering the maximum peripheral rotor speed $v_{max} = 300$ m/s. This is a realistic value for PM rotors with a retaining sleeve (Schweitzer and Maslen, 2009). It yields an upper limit on the rotor radius:

$$R_{m,max} = \max(R_m) = \frac{v_{max}}{2\pi\omega}. \tag{5.55}$$

Also, the air gap width was set at 1.5 mm, which includes the width of a potential sleeve and allows for rotor eccentricities.

5.3.4 Results and discussion

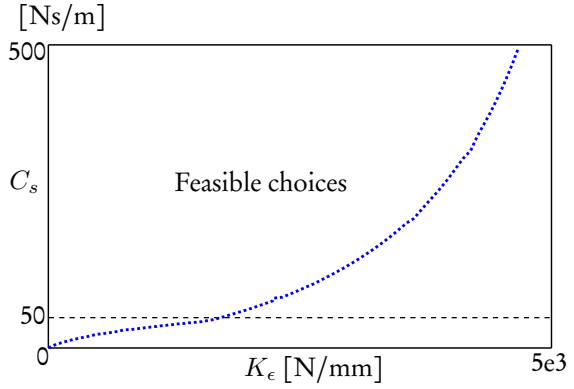

Fig. 5.16: Pareto front of the bearing performance at $\omega = 2\pi 1000$ rad/s.

Let us analyze the results for $\omega = 2\pi 1000$ rad/s. The Pareto front in Fig. 5.16 shows that the damping required for stabilization increases with the bearing stiffness. The graph was limited to values of $C_s < 500$ Ns/m, which can be considered as very large for damping added in a passive, contactless way. Damping values of an order of magnitude of 10 Ns/m are reported in the literature (Filatov and Maslen, 2001).

Regarding thermal limitations, the winding current densities for each individual on the Pareto front are given in Fig. 5.17. The losses are calculated assuming a static eccentricity of the rotor with an off-centering amplitude $\epsilon = 0.5(R_w - R_m)$. In this case, the current density always lies below the maximal value of 5 A/mm^2. In Fig. 5.17, the individuals are arranged in the same order as in Fig. 5.16: the individuals

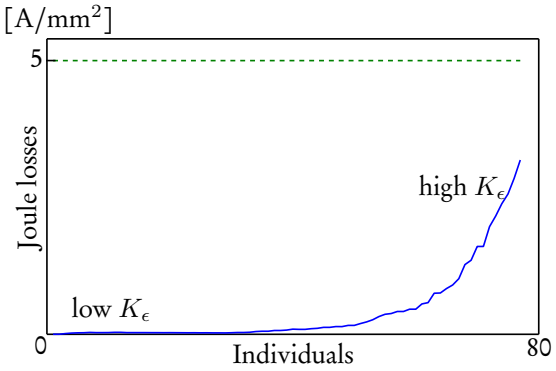

Fig. 5.17: Joule losses associated with the individuals on the Pareto front. The green, dashed line corresponds to the maximal amount of Joule losses.

with lower stiffnesses on the left-hand side and the individuals with higher stiffnesses on the right hand side. This will be the case for all the figures in the following sections.

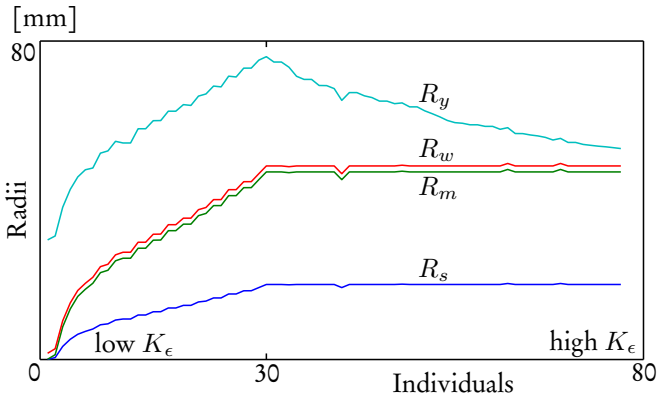

Fig. 5.18: Geometrical parameters of the individuals on the Pareto front for $\omega = 2\pi 1000$ rad/s.

Figures 5.18 and 5.19 show that bearings with a thicker winding ($R_y - R_w$) require less damping for stabilization. This is the case for the individuals 1-30 with winding thicknesses nearing the maximum value. It corresponds to expectations as a lower winding resistance yields a more inductive behavior of the bearing that is known to have a positive effect on the stability [4,7]. On the contrary, the individuals 30-80 have a greater PM thickness and thinner windings. As a result, the magnetic field strength and the bearing stiffness are higher. However, the winding is more resistive as $(R_y - R_w)$ decreases, which affects the stability.

The Pareto fronts corresponding to the spin speeds $\omega = 2\pi \{50, 100, 500, 1000\}$ rad/s are given in Fig. 5.20. For a given value of K_ϵ, more damping is required

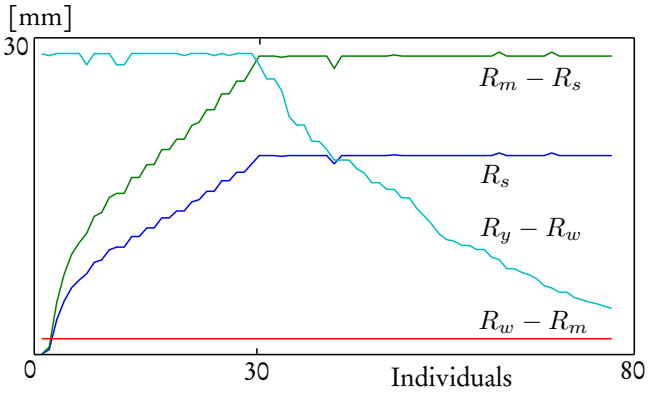

Fig. 5.19: Width of the shaft (R_s), permanent magnets ($R_m - R_s$), air gap ($R_w - R_m$) and winding ($R_y - R_w$).

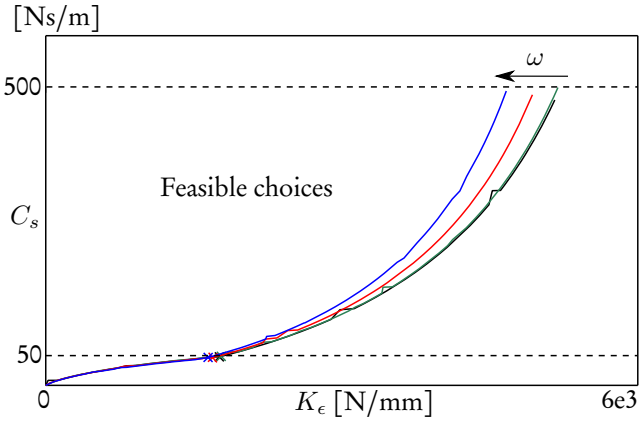

Fig. 5.20: Pareto fronts for $\omega = 2\pi \{50, 100, 500, 1000\}$ rad/s.

to stabilize the bearings running at higher speeds. This is due to the mechanical constraint on the peripheral speed. The value of $R_{m,max}$ is lower for the individuals running at higher speeds, which lowers the volume of PMs. An absence of constraint on the peripheral speed should yield opposite results as a given winding will be more inductive while running at higher speeds.

The graphs of the bearing geometrical parameters in the cases $\omega = 2\pi \{50, 100, 500\}$ rad/s have a shape similar to that of the $\omega = 2\pi 1000$ case. In each case, the crosses in Figs. 5.20 and 5.21 indicate the individuals that have PMs and winding widths close to their maximum values. For instance, it is the 30^{th} individual in the case of $\omega = 2\pi 1000$ rad/s (Fig. 5.19). For individuals lying further to the left on the Pareto front, the winding thickness reaches its maximum value, whatever the spin speed. In this area, the Pareto fronts for all the speeds are almost superimposed, as shown in Fig. 5.21. Furthermore, the values of damping lie in the range $C_s \in [0, 50]$

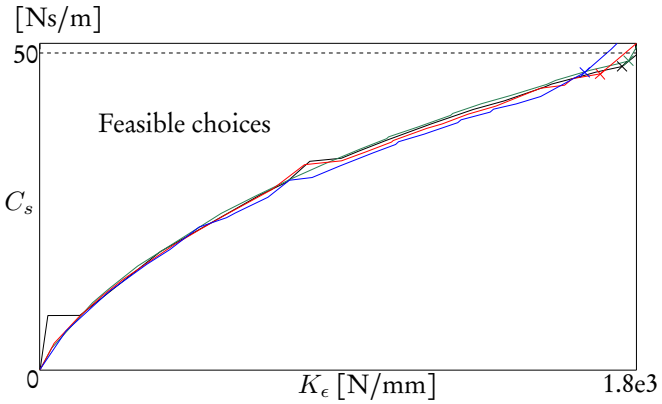

Fig. 5.21: Zoom on the area of interest where $C_s < 50$ [Ns/m].

Ns/m in this figure, which is more realistic. As a result, a bearing optimized under the constraints (5.54) and (5.55) requires a same amount of damping for a given stiffness, whatever the spin speed. For $\omega = 2\pi \{50, 100, 500\}$ rad/s, the winding current densities are not given as they are far lower than the limit of 5 A/mm^2.

5.3.5 Comparison with existing EDBs

The performance of existing EDBs are summarized in (Detoni, 2014). The stiffness to magnet volume ratio was calculated, yielding the black triangles in Fig. 5.22. The blue, solid lines correspond to the data for the EDBs lying on the Pareto front in Fig. 5.20. The magnet volume was calculated assuming a bearing length worth twice the PM radius R_m. Each of these lines has a vertical part corresponding to the individuals with $R_m \cong R_{m,max}$, which is why the PM volume remains constant.

The overall shape of the graph shows that bearings operating at higher spin speeds can reach better stiffness to PM volume ratios. Compared with existing EDBs, the present topology provides a reasonable ratio at high speed, although it was not optimized considering this specific criterion.

5.4 Conclusion

This chapter concerned the comparison and optimization of the performance of EDBs.

A first section introduces the performance criteria of EDBs, i.e. the radial stiffness and the instability margin. Then, a graphical method for the evaluation of these criteria is derived. In this aim, a lumped-parameter electromechanical model of EDBs is obtained under the quasi-static assumption. Thanks to this assumption, this model is simpler than the dynamic model of chapter 4, and an analytical expression of its

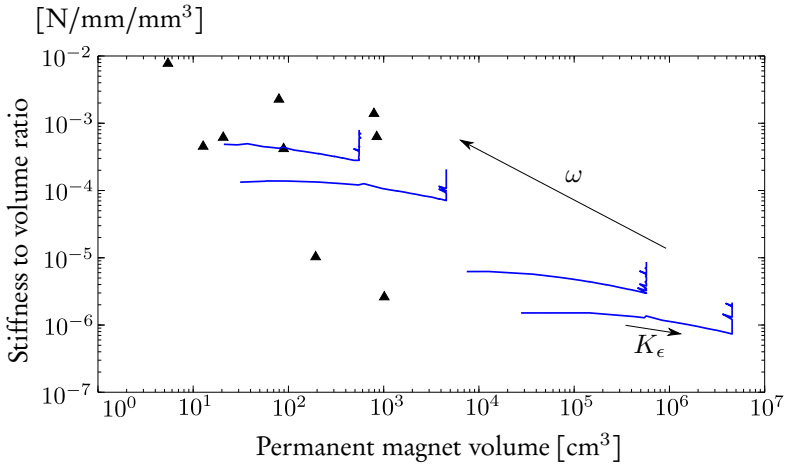

Fig. 5.22: Stiffness to volume ratio of the existing EDBs (triangles) and of the individuals on the Pareto fronts of Fig. 5.20 (solid lines).

roots can be obtained. It appears that the stability and the stiffness of a bearing can be evaluated separately by looking at the system root locus. For two bearings with a same mass M and in the absence of damping ($C = 0$), looking at the real and imaginary parts of the system roots allows to know which one has the greatest stiffness and/or needs less damping to be stable. This is valid under the assumption $|\Re\{\rho|_{C=0}\}| \ll |\Im\{\rho|_{C=0}\}|$, which corresponds to high spin speeds ω and to an inductive behaviour of the winding. This assumption is not very restrictive as it corresponds to the operating region that is preferred when considering the difficulty of adding external damping in the system.

A second section applies the previous graphical approach to the study of the impact of the yoke permeability on the performance of an EDB. In this aim, two bearings of identical topology, but with and without ferromagnetic yoke are compared. The parameters of the lumped-parameter model developed in the previous section are calculated using a field model adapted to this topology, whose derivation is summarized. Finally, the system root locus is drawn.

From the analysis of the root locus, it appears that the negative impact of the detent force associated with a ferromagnetic yoke is well counterbalanced by an increase in the centering electrodynamic force. Furthermore, the presence of a ferromagnetic yoke improves the performance of the bearings in some cases. In particular, the yoke material does not have a significant influence on the performance of the bearing for a small rotor shaft radius. As this radius increases, the stiffness of the bearing decreases and this effect is less significant for a bearing with a ferromagnetic yoke. On the other hand, increasing the pole pairs number of the bearing has a positive effect on the bearing stiffness but is less advantageous for a bearing with a

ferromagnetic yoke when the yoke is close to the permanent magnets.

At the end of the second section, a validation of the graphical analysis method is presented. It shows that the quasi-static model is appropriate to predict the free motion of the rotor. Furthermore, the roots predicted using the quasi-static and the dynamic models are calculated and compared. The close agreement between these results indicates that the graphical method derived using the quasi-static model can be used to interpret the root loci obtained with the dynamic model that is preferred when studying the system stability.

In a third section, the domain of achievable performance of a heteropolar EDB was obtained by generating a Pareto front using an optimization algorithm. The bearing is optimized with regard to the stiffness and the instability margin. These performance criteria are evaluated using the dynamic model developed in chapter 4, whose parameters are identified using the field model exposed in the second section of this chapter. The domain of achievable performance is obtained for different spin speeds, highlighting a clear trade-off between stiffness and stability.

Then, the bearings lying on the Pareto front are compared to existing EDBs in terms of stiffness to volume ratio. It was shown that ratios similar to that of existing EDBs can be achieved at high speeds with the present EDB topology. This ratio could be further optimized as it was not an objective function of the present optimization.

Unbalanced magnetic pull prediction in PM machines

6

In this chapter, the lateral forces in an electrical motor are predicted using the model derived in chapter 4. The main assumptions of the model are tested to establish its applicability in the present case. Then, the force predictions are compared to finite element analysis results for validation.

The content of this chapter is the subject of (Dumont et al., 2016a; Kluyskens et al., 2017).

6.1 Introduction

Bearing wear and manufacturing tolerances can lead to rotor eccentricities in permanent magnet (PM) machines. This affects the symmetry of the field distribution in the airgap, thereby creating a radial detent force known as unbalanced magnetic pull (UMP) (Dorrell et al., 2009; Rahideh and Korakianitis, 2011). The UMP is a potential source of excessive noise, vibrations, and additional wear of the mechanical bearings (Kim and Lieu, 2005; Li et al., 2007). Therefore, passive and active strategies have been studied to reduce these effects. Among them, the parallel connection of the stator windings is well known (Burakov and Arkkio, 2007; Kasten and Redemann, 2014). It allows passively induced currents to flow in the stator windings when the rotor spins in an off-centered position, thereby creating forces that balance the UMP.

Different models predicting the balancing forces in PM motors have been proposed (Burakov and Arkkio, 2006; Dorrell and Ionel, 2012). These models can be adapted to a wide range of machines. However, they include assumptions on the rotor motion so that only static and dynamic eccentricities are considered, and the model parameters must be re-estimated if the operating point of the motor changes. Referring to Fig. 6.1, the static eccentricity corresponds to a motion such that ϵ and

ϕ are constants, while $\gamma = \omega t$. The dynamic eccentricity corresponds to fixed values of ϵ and γ, but $\phi = \lambda t$ where λ is the whirl speed.

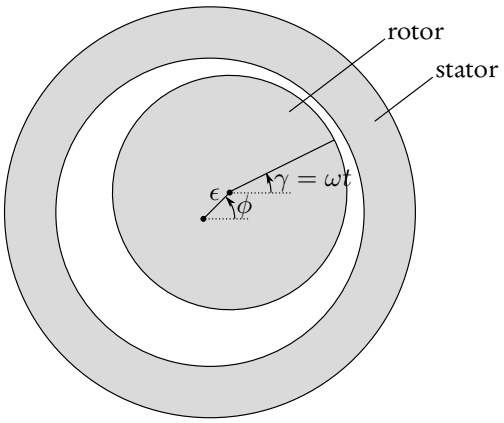

Fig. 6.1: Mechanical variables of a rotor with two degrees of freedom.

The operation of heteropolar EDBs is also based on passively induced centering forces. In particular, the origin of these forces is the same as in PM motors with parallel winding connections. When the rotor is off-centered, the PM field distribution changes in the air gap, thereby creating additional harmonics that increase with the off-centering (Rahideh and Korakianitis, 2011). For example, if the main harmonics in the initial PM field distribution has one pair of poles, the most significant harmonic created by the off-centering has two pole pairs. On the one hand, these harmonics have a negative effect since their interaction yields the UMP (Chiba et al., 2005). On the other hand, the two pole pairs harmonic can be linked by a winding that also has two pole pairs, thereby inducing balancing currents which tend to restore the centered position of the rotor. Similarly, in the case of a one pole pair PM motor, the parallel connection of each motor phase may allow for the existence of conducting paths with two pole pairs and thus for passive centering forces.

In this context, this chapter proposes a method for predicting the passive electrodynamic forces in brushless PM motors using the model derived in chapter 4. In this aim, the model is applied in the practical case of a high-speed DC motor dedicated to air compression that is currently being designed at the FEMTO-ST institute (Gilson et al., 2015). For example, the rotor of the motor could be supported by air bearings that allow small radial displacements, resulting in radial forces that can be evaluated with the model.

The chapter is organized as follows. Firstly, the appearance of radial electrodynamic forces in PM motors is explained through two examples. Secondly, the present case study is introduced, and the motor topology and winding connections are presented. Then, the EDB model is recalled and applied to the motor case. The main

assumptions of the model are validated and the parameters corresponding to the motor are computed. Finally, the model is exploited to predict the radial forces on the off-centered rotor, and these predictions are compared with finite element simulation results.

6.2 Radial electrodynamic forces in PM machines

Radial electrodynamic forces may appear in PM motors with rotor eccentricities. These forces result from currents that are induced passively in the motor windings. These currents may appear passively thanks to the presence of short-circuited current paths in the motor phases, in addition to the current path corresponding to a conventional operation of the motor. The currents flowing in these two paths are referred to as the suspension and motor currents, respectively.

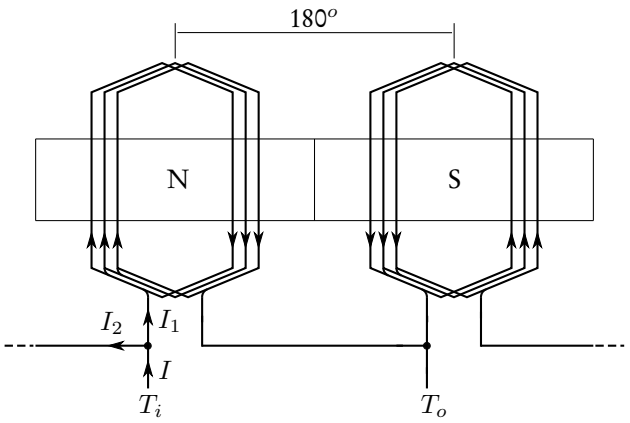

Fig. 6.2: Rotor magnet poles and a single winding phase of a motor with one pole pair. The arrows indicate the motor current path.

Let us illustrate this with a first example. Figure 6.2 shows the PM poles and the winding arrangement of a one pole pair motor. The depicted phase comprises two coils that are fed through the terminals T_i and T_o. The two possible current paths are illustrated in Fig. 6.3. The path shown in Fig. 6.3 (a) has one pole pair, and feeding the motor through the terminals T_i and T_o thus creates a torque. The second, short-circuited path is shown in Fig. 6.3 (b). It has two pole pairs, and the current flowing in this path creates a force on the rotor in accordance with the guideline $q = p + 1$ derived in chapter 3.

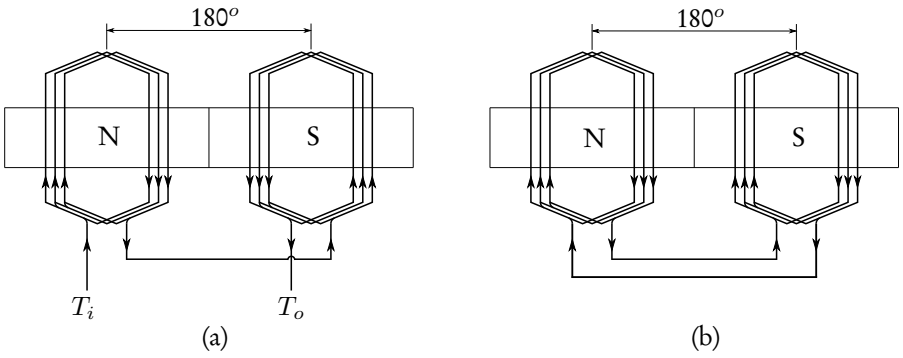

Fig. 6.3: Path of the current associated with the production of a torque (a) and a force (b). The rotor permanent magnets have one pole pair.

The analysis of the induced electromotive forces in the winding phase shows that the currents in the phase of Fig. 6.2 are governed by (Kluyskens et al., 2017):

$$\begin{aligned} U_{T_i-T_o} + E_0 + E_d - RI_1 - j\omega L_c I_1 &= 0 \\ U_{T_i-T_o} + E_0 - E_d - RI_2 - j\omega L_c I_2 &= 0 \\ I_1 + I_2 &= I, \end{aligned} \tag{6.1}$$

where R and L_c are the coil resistance and cyclic inductance, $U_{T_i-T_o}$ is the feed source voltage, E_0 is the electromotive force associated with the PM flux linkage in a coil when the rotor spins in a centered position, and E_d is the additional electromotive force due to the rotor eccentricity that causes a change in the PM flux linked by the coils. The electromotive force E_0 is constant, whereas E_d is proportional to the eccentricity. As a result, $E_d = 0$ when the rotor is centered and (6.1) yields:

$$\begin{aligned} I_1 = I_2 &= \frac{U_{T_i-T_o} + E_0}{R + j\omega L_c} \\ I &= \frac{2(U_{T_i-T_o} + E_0)}{R + j\omega L_c}. \end{aligned} \tag{6.2}$$

The currents in both coils are equal. As stated above, they only contribute to the torque production since they flow in a path with one pole pair. On the other hand, when the rotor is not centered, $E_d \neq 0$ and (6.1) yields:

$$\begin{aligned} I_1 &= \frac{U_{T_i-T_o} + E_0}{R + j\omega L_c} + \frac{E_d}{R + j\omega L_c} \\ I_2 &= \frac{U_{T_i-T_o} + E_0}{R + j\omega L_c} - \frac{E_d}{R + j\omega L_c} \\ I &= \frac{2(U_{T_i-T_o} + E_0)}{R + j\omega L_c}. \end{aligned} \tag{6.3}$$

As stated above, the additional current components due to the rotor eccentricity create a restoring force since they flow in a path with two pole pairs. The equivalent circuit corresponding to (6.1) is shown in Fig. 6.4. The left and right branches of the circuit correspond to the left and right coils in Fig. 6.2.

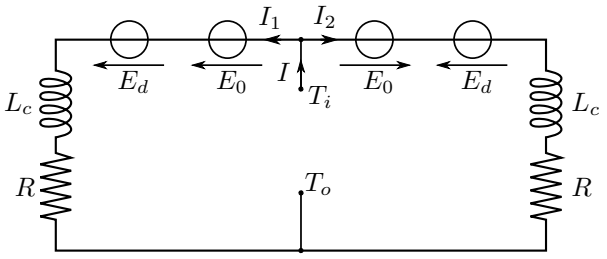

Fig. 6.4: Equivalent electrical circuit of a winding phase.

Similarly, this centering effect can be found in motors with other winding arrangements. For example, the case of a motor with two pole pairs is shown in Fig. 6.5.

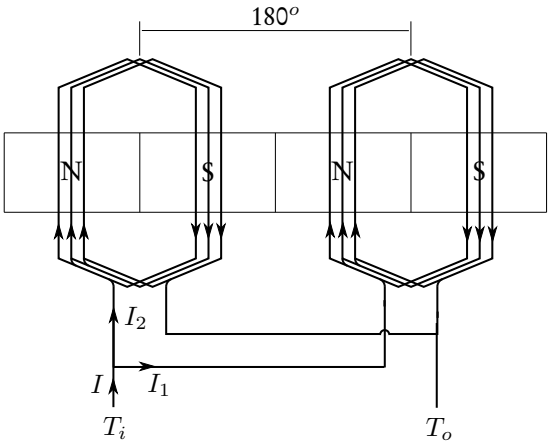

Fig. 6.5: Rotor magnet poles and a single winding phase of a motor with two pole pairs. The arrows indicate the motor current path.

Again, two conducting path can be considered. The path associated with the torque production has two pole pairs as shown in Fig. 6.6 (a). The short-circuited path associated with the radial forces has one pole pair, in accordance with the guideline $q = p - 1$ derived in chapter 3. It is shown in Fig. 6.6 (b).

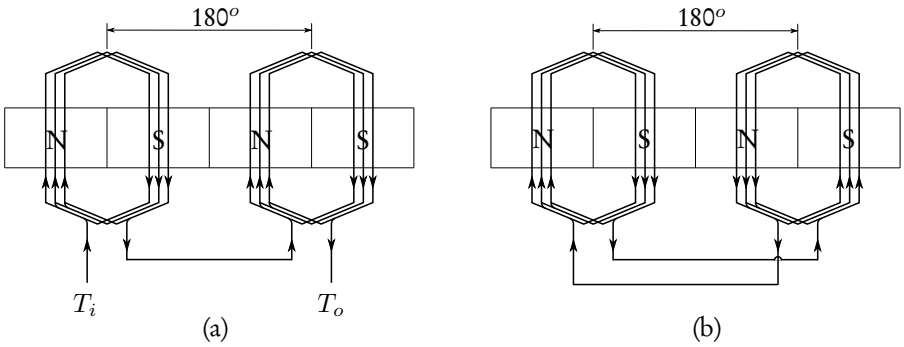

Fig. 6.6: Path of the current associated with the production of a torque (a), and a force (b).

6.3 Case study

This section presents the calculation of the radial electrodynamic force in a motor with one pole pair whose winding is connected as in Fig. 6.2.

6.3.1 Machine description

The motor topology is shown in Fig. 6.7 (a). This motor is designed for high-speed applications such as air compression. Therefore, it has a large airgap and a retaining sleeve around the PMs. The parameters of the motors are given in Tables 6.1 and 6.2. The nominal airgap is denoted $g = R_s - R_{sl}$.

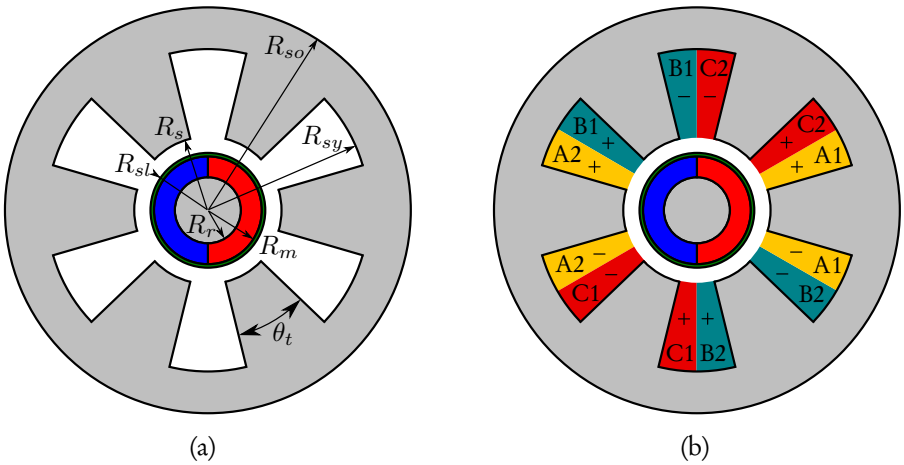

Fig. 6.7: Motor topology and phases arrangement. (a) Geometrical parameters of the motor. The internal rotor comprises surface-mounted PMs with one pole pair and a retaining sleeve. (b) The winding has three phases composed of two concentrated coils. For example, the coils A1 and A2 constitute phase A.

Table 6.1: Motor geometrical parameters.

parameter	value	units
R_{so}	35	mm
R_{sy}	27.8	mm
R_s	12.7	mm
R_{sl}	9.9	mm
R_m	9.3	mm
R_r	5.7	mm
θ_t	32.4	^{o}
L (axial length)	30	mm

Table 6.2: Other motor parameters.

parameter	value	units	definition
B_r	1.2	T	remanent magnetization
σ_c	$6e7$	S/m	copper conductivity
r	0.5	-	slot fill factor
b	10	-	number of wire turns around each slot
μ_1	1	-	relative permeability of the PMs, retaining sleeve, and winding
μ_2	∞	-	Relative permeability of the rotor shaft and stator yoke

The stator yoke has six slots and three phases, each of them being composed of two concentrated winding coils. As shown in Fig. 6.8, the coils can be connected in series or in parallel. In this section, only the parallel connection is considered. As exposed in section 6.2, this allows for passively induced currents to flow in short-circuited paths that are shown by the arrows in Fig. 6.8 (a). These paths have two pole pairs and are referred to as the suspension phases in the next sections. Let us note that there can be a non zero motor phase current with a zero suspension phase current and vice-versa.

6.3.2 Parameters identification

In this section, the dynamic model and its assumptions are recalled. Then, the model parameters are evaluated, and some of its assumptions are validated using two-dimensional magnetoquasistatic finite element (FE) simulations to show its applicability in the present case. The magnetic permeability of the shaft and yoke is set to $\mu_r = 1000$ in the FE model.

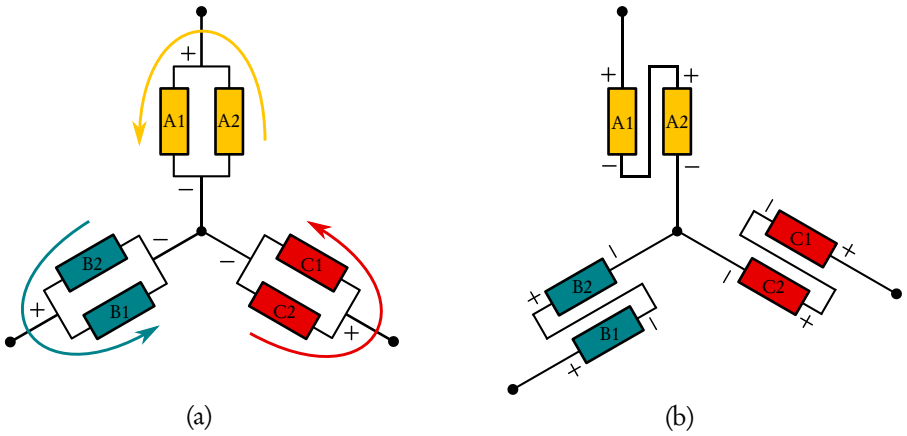

Fig. 6.8: Two different motor phase coils connections. (a) Phase coils connected in parallel. The arrows show the short-circuited current paths for the suspension currents. (b) Phase coils connected in series. There are no possible current paths in the windings for the suspension currents.

EDB model

Initially, this motor was designed without considering a rotor off-centering. However, in case of rotor off-centering, passively induced currents flow in the motor phases that are connected in parallel, resulting in balancing forces. These passive electrodynamic forces can be predicted using the model initially developed for EDBs (4.44). As a reminder, this model links the radial forces to the rotor position through a linear equation with constant coefficients:

$$\dot{F} = -\frac{R}{L_c}F - j\omega F - K_d\dot{z} - \frac{3K_\Phi^2}{2L_c}\dot{z} - \frac{RK_d}{L_c}z - j\omega z K_d - j\omega z\frac{3K_\Phi^2}{2L_c}, \qquad (6.4)$$

where the forces and rotor displacements are expressed in the stator frame using the complex notations $F = F_x + jF_y$ and $z = x + jy = |z|e^{j\phi}$, respectively. The parameter R is the phase resistance of a suspension phase, K_d is the negative stiffness associated with the detent force between the PMs and the stator yoke, and K_Φ is the PM flux constant defined in (6.5). The cyclic inductance is $L_c = L - M$, where L and M are the self- and mutual inductances of the suspension phases, respectively.

The model was derived under the following assumptions:

1. the rotor spin speed ω is an input of the system and is constant;
2. only translational eccentricity is considered, i.e., the magnetic axis of the rotor and winding remain parallel;

3. the materials have linear magnetic characteristics and therefore magnetic hysteresis and saturation are neglected;
4. there is no proximity or skin effect in the conductors;
5. the eddy currents are neglected in the PMs, in the sleeve and in the stator yoke;
6. the impact of the rotor off-centering $|z|$ on the winding inductances is neglected;
7. the detent force F_d between the PMs and the yoke obeys: $F_d = -K_d z$, where the detent stiffness K_d is real and negative;
8. the permanent magnet flux linkage in the suspension phases is proportional to the off-centering. Only the main flux harmonic is considered;
9. the motor currents do not impact the radial forces on the rotor.

As a result of assumption 8, the PM flux linkage in the suspension phases obeys:

$$\Phi_k = |z| K_\Phi \cos\left(\omega t + \phi + \frac{2\pi(k-1)}{3}\right), \tag{6.5}$$

where $k \in \{1, 2, 3\}$ is the phase number. Lastly, the coefficients K_d, K_Φ^2/L_c, and R/L_c in (6.4) do not depend on the number of winding turns k. Therefore, k has no impact on the forces and can be chosen considering only the constraints associated with the motor function.

Suspension phase resistance

The suspension phase resistance is obtained without taking the end-windings into account. Considering the motor parameters from Table 6.1 and 6.2, this yields:

$$R = \frac{48 L b^2}{\sigma_c r \pi \left(R_{sy}^2 - R_s^2\right)\left(1 - \frac{\theta_t}{60}\right)} = 5.4\ \mathrm{m\Omega}. \tag{6.6}$$

Radial detent force

Let us study the radial forces in the absence of current in the suspension phases. When the rotor is off-centered, the symmetry of the magnetic field in the airgap is broken. This results in a parasitic attraction force between the rotor and the stator. This force has two components acting in the direction of the off-centering z and in the direction perpendicular to it.

Assuming that they are proportional to the off-centering, they can be associated with the stiffnesses:

$$\begin{aligned} K_{d\epsilon} &= -\Re\left\{\frac{F}{z}\right\} \\ K_{d\phi} &= -\Im\left\{\frac{F}{z}\right\}. \end{aligned} \tag{6.7}$$

From the model assumptions in section 6.3.2, $K_{d\phi}$ is neglected and the value of $K_{d\epsilon}$ is constant and does not depend on the rotor position. Furthermore, it is assumed that the forces on the rotor in the absence of suspension currents are detent forces only i.e., the impact of the currents flowing in the motor phases is neglected.

Let us validate this by calculating $K_{d\phi}$ and $K_{d\epsilon}$ for two different kinds of rotor motion with the FE model. Figure 6.9 (a) corresponds to the static eccentricity configuration, i.e. the rotor spins in a fixed position $z = g/2$. Figure 6.9 (b) corresponds to the dynamic eccentricity configuration, i.e. the rotor center whirls around the stator center so that $|z| = g/2$, while $\omega = 0$. In the absence of motor currents, the mean value of $K_{d\epsilon}$ is $K_d = -16.96$ kN/m, whereas the amplitude of $K_{d\phi}$ does not exceed 4% of K_d for both kinds of rotor motion.

The impact of the motor currents is obtained by setting $I_A = -2I_B = -2I_C$, where I_A is such that the current density on the copper cross-section of phase A reaches the maximum value of 5 A/mm^2. The results are also shown in Fig. 6.9. In presence of motor currents, the value of $K_{d\epsilon}$ does not differ by more than 7% of the mean value $K_d = -16.96$ kN/m, whereas the amplitude of $K_{d\phi}$ does not exceed 4% of K_d for both kinds of rotor motion.

In the next sections, the impact of the off-centering and motor currents on $K_{d\phi}$ is neglected and $K_{d\epsilon}$ is assumed to be constant: $K_{d\epsilon} \approx K_d = -16.96$ kN/m, and $K_{d\phi} \approx 0$ kN/m.

PM flux linkage

Let us validate (6.5), which states that only the main PM flux harmonic is considered in the suspension phases, and that it is proportional to the off-centering $|z|$. In this aim, the value of $K_\Phi = 0.486$ Wb/m is identified by evaluating the amplitude of the main PM flux harmonic in the suspension phase A when the rotor spins at $z = g/4$. This corresponds to the 'fitting curve' in Fig. 6.10 (a). Then, the PM flux in all the suspension phases are predicted through (6.5) and compared to FE results for different eccentricities and different kinds of motion. As shown in Fig. 6.10 (a) and (b), the model is accurate and assumption 8 is thus valid in this case.

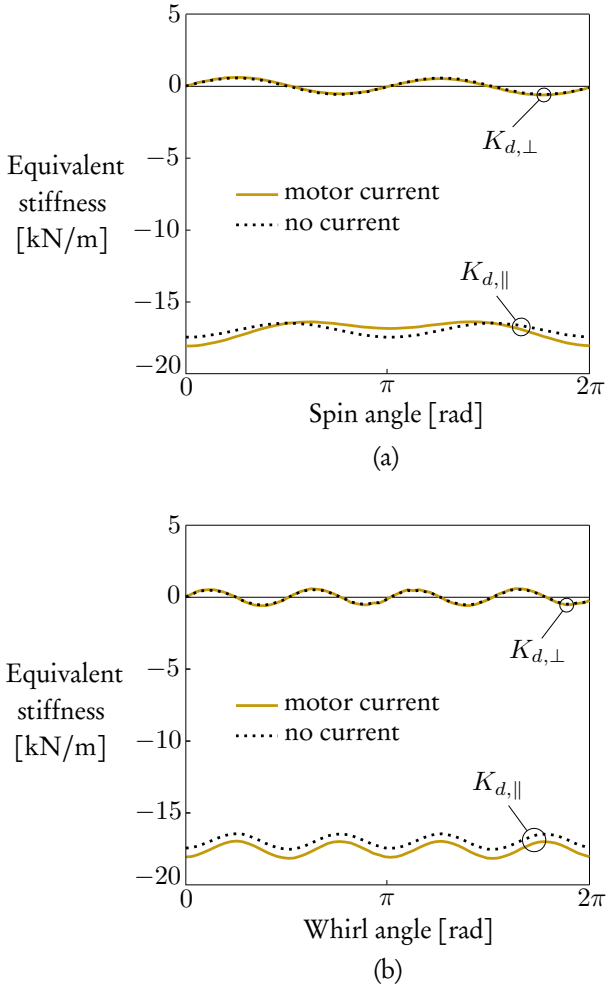

Fig. 6.9: Amplitude of the equivalent stiffness between the rotor and the stator in the absence of suspension currents. The motor currents are set to zero or to maximum values so that $I_A = -2I_B = -2I_C$, where I_A is such that the current density on the copper cross-section of phase A reaches 5 A/mm^2. (a) Data obtained in a static eccentricity configuration. (b) Data obtained in a dynamic eccentricity configuration.

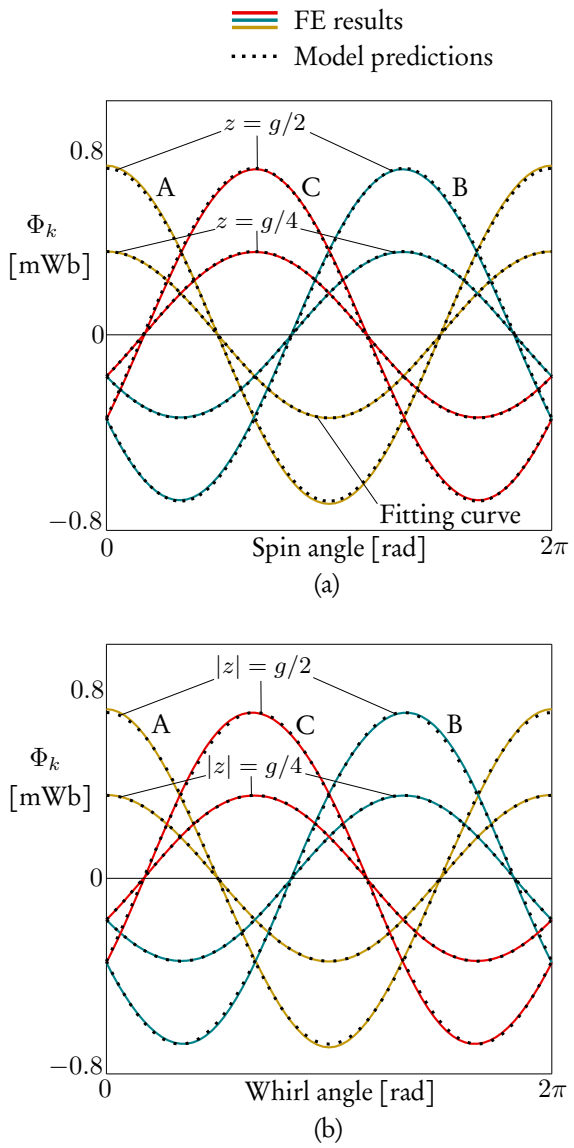

Fig. 6.10: Comparison between FE and the model predictions of the PM flux in the suspension phases. The rotor eccentricity is set to $g/4$ and $g/2$. Coefficient K_Φ is identified using the data of the 'fitting curve', allowing to predict the flux linkage in each winding phase when the rotor spins (a) or whirls (b), for example.

Suspension phases inductances

Due to the presence of a ferromagnetic shaft, a rotor off-centering impacts the mutual inductances of the suspension windings. The ratio of the mutual inductances between the suspension phases to their respective average values is shown in Fig. 6.11. This is obtained assuming a whirling rotor motion such that $|z| = g/2$. The impact of the off-centering on the mutual inductances does not exceed 0.5% of their average value and is thus neglected.

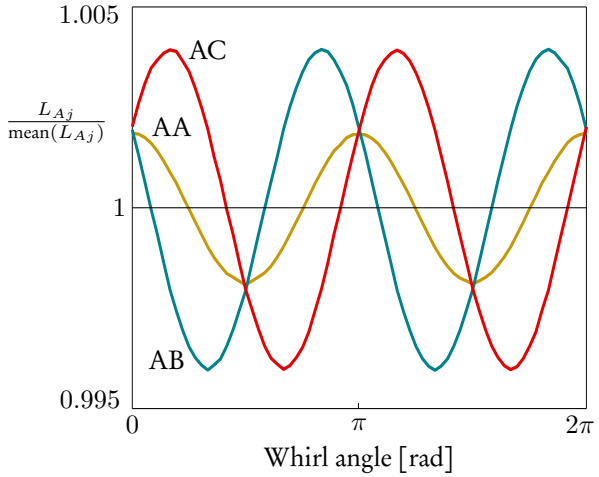

Fig. 6.11: Ratio of the mutual inductances between the suspension phases to their respective average values.

In conclusion, assumption 6 regarding the inductances is confirmed. From the FE results, the cyclic inductance of the suspension windings is obtained by combining the mutual inductances obtained when the rotor is centered. Assuming a single winding turn, this yields:

$$L_c = L_{AA} - \frac{1}{2}L_{AB} - \frac{1}{2}L_{AC} = 32.5\mu\text{H}. \tag{6.8}$$

6.3.3 Forces prediction

The accuracy of the model force predictions are validated through a comparison with FE simulation results. In this aim, a transient FE model of the motor is run using the following approach. The motor is fed with three-phase balanced sinusoidal currents so that the peak current density in each phase is 5 A/mm^2. The radial forces are then obtained in a static eccentricity configuration for different spin speeds and eccentricities. Figure 6.12 (a) and (b) show the average values of F_ϵ and F_ϕ calculated over one full revolution of the rotor. They are denoted $\bar{F}_\epsilon$ and $\bar{F}_\phi$, respectively. As the model

is transient, it is run during more than $5\tau = 5L_c/R$ seconds before recording the data to ensure that the suspension currents have reached a steady state.

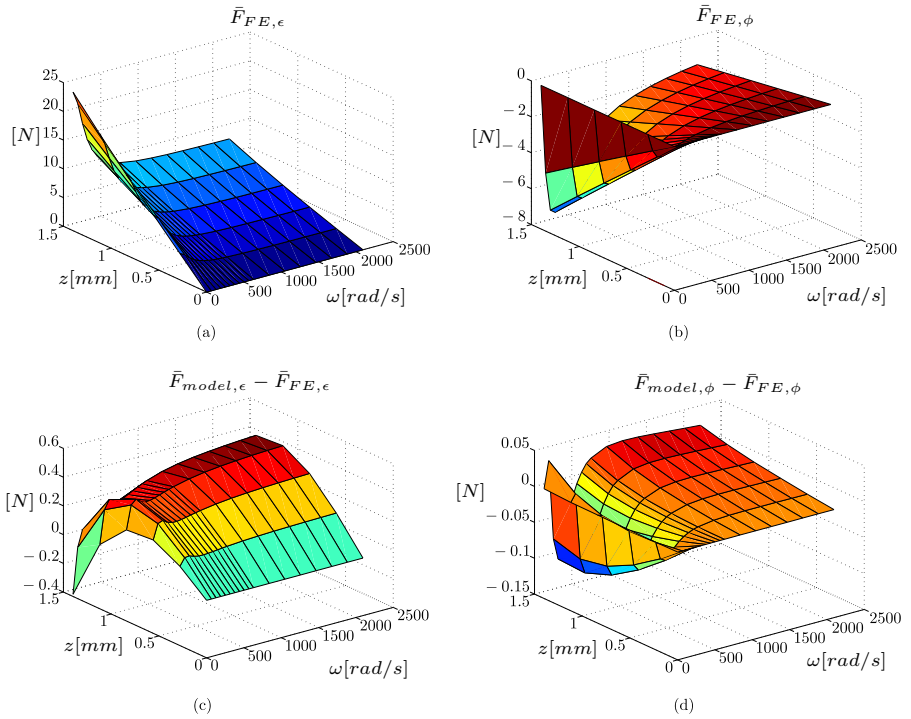

Fig. 6.12: Forces on the rotor spinning in a static eccentricity configuration. (a) and (b) Average forces $\bar{F}_\epsilon$ and $\bar{F}_\phi$ from FE results. (c) and (d) Difference between the FE results and the model predictions of the average forces $\bar{F}_\epsilon$ and $\bar{F}_\phi$.

Let us analyze these results. At zero spin speed, there is no electrodynamic centering force. Only the detent force acts in the direction of the off-centering and its amplitude is given by the curve $\omega = 0$ rad/s in Fig. 6.12 (a). At higher values of ω, the centering electrodynamic force increases and saturates above $\omega = 600$ rad/s. This effect is significant, resulting in a reduction of $\bar{F}_\epsilon$ to 40% of its value at zero spin speed. Despite this reduction, the electrodynamic force is not sufficient to fully counterbalance the detent force. On the other hand, $\bar{F}_\phi$ can also reach significant values of up to -7.2 N at $z = 1.4$ mm and $\omega = 189$ rad/s. This value decreases at higher speeds.

Finally, the difference between the model predictions and the FE results is given in Fig. 6.12 (c) and (d), showing the accuracy of the model.

The model predicts that the amplitude of the forces is constant in the static eccentricity configuration. Its predictions fit well to the average values of the forces obtained from the FE simulations, as shown in Fig. 6.12 (c) and (d). However, the

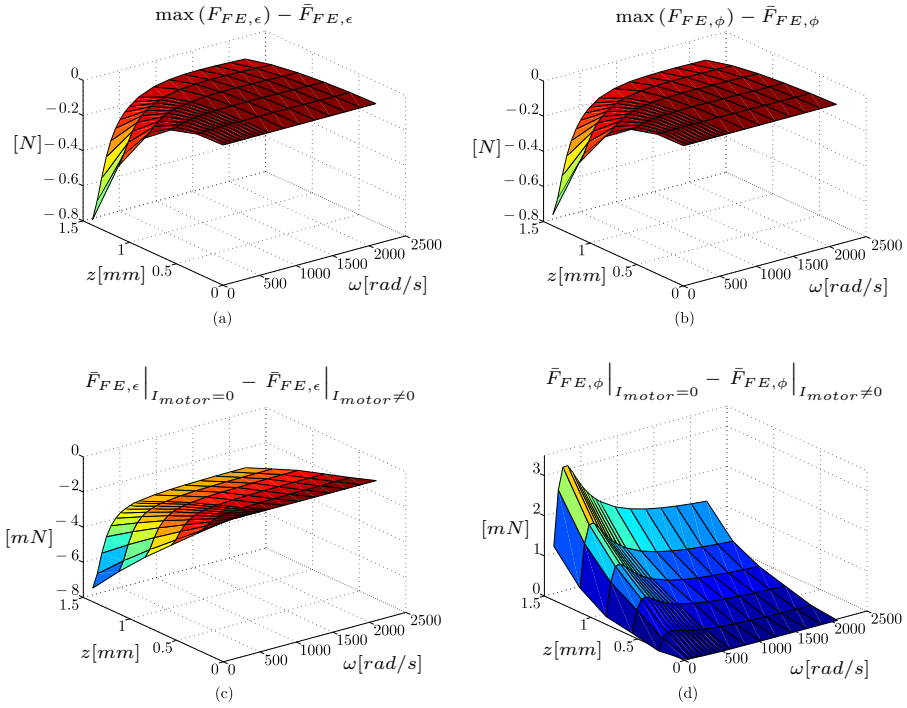

Fig. 6.13: Forces on the rotor spinning in a static eccentricity configuration. (a) and (b) Maximum difference between FE predictions of F_ϵ and F_ϕ and their respective average values. (c) and (d) Difference between the average forces on the rotor, with and without motor currents.

amplitude of the forces can vary with the angular position of the rotor, according to the FE results. Let us now compare the maximum values of F_ϵ and F_ϕ to their respective average values. As shown in Fig. 6.13 (a) and (b), the absolute difference between the maximum and average values of the forces is moderate. In relative terms and for F_ϵ, this difference does not exceed 3% of its average value within the domain shown in Fig. 6.13 (a). For F_ϕ, the relative difference is also small except at low speed and for large eccentricities, where the relative error peaks up because the force amplitude approaches zero.

Lastly, the average forces $\bar{F}_\epsilon$ and $\bar{F}_\phi$ are calculated in the absence of motor currents. The difference between the average forces with and without the motor currents are negligible, as shown in Fig. 6.13 (c) and (d). This validates assumption 9 from section 6.3.2.

6.4 Conclusion

This chapter aimed at applying the EDB model to the prediction of the radial electrodynamic forces in PM machines. First, the appearance of electrodynamic forces in motors was illustrated through two examples of motors with parallel connections of the stator windings. Then, a slotted PM motor that is being designed at the FEMTO-ST institute was introduced as a case study. The most important assumptions of the EDB model were validated to show its applicability in this case. In particular, it was shown that the suspension function can be studied separately from the motor function. Finally, the force predictions were compared with FE simulation results, showing a good agreement between them. In particular, the model shows a good accuracy at low eccentricities, which corresponds to the most likely operating conditions of the motor.

Besides, this study showed that the electrodynamic force cannot fully compensate the detent force in the present motor. However, the effect of the detent force can be reduced by up to 60% of its value in the absence of electrodynamic forces.

From a theoretical point of view, further studies could include a more detailed analysis of the coupling between the suspension and motor functions. Also, other kinds of rotor eccentricities should also be simulated to better illustrate the potential of the model when it comes to predicting the forces for various kinds of rotor motion. The EDB model could also be used to investigate potential self-bearing PM machines based on electrodynamic forces, such as those presented in (Kluyskens et al., 2017). In addition, this model and the associated parameters identification process could also be used during the thermal design of the machine for predicting the balancing currents and the associated increase in Joule losses due to a rotor eccentricity. The possibility of further reducing the UMP through the use of non-ferromagnetic materials for the slots could also be investigated.

Conclusion 7

Content overview

This thesis first presented the state of the art of null-flux, heteropolar EDBs. Their operating principle was explained concisely, based on the identity linking the centering force to the magnetic coenergy gradient. Then, the topologies proposed in the literature were gathered and re-drawn in a single framework to ease the understanding of their operation and their comparison. It appeared that many bearing topologies have been described, but no design guideline has been proposed yet.

The state of the art regarding the models was also browsed. The existing models were found to be very diverse, and based on analytical and/or numerical methods. Most of them were shown to be quasi-static and adapted to a particular bearing geometry, whereas only one dynamic model had been derived. The use of these models was shown to be limited by kinematic assumptions and/or a limited scope regarding the bearing topologies. The few existing experimental results were also pointed out, including a conclusive levitation test.

In this context, two new models were proposed. The first one is derived in the aim of obtaining general guidelines for the design of heteropolar bearings. It is quasi-static and predicts the forces in a bearing with PMs creating a magnetic field with p pole pairs and an airgap winding of arbitrary shape, but with q pole pairs. By imposing constraints on the winding shape to ensure the presence of a centering force and the null-flux characteristic, the design guideline $q = p \pm 1$ was obtained. This was validated through finite element simulations. From these guidelines, other bearing topologies were brought to light.

The second model is dynamic. It takes the form of a linear state-space representation and is based on a lumped-parameter model comprising six parameters that fully characterize the bearing. Thanks to the absence of static eccentricity assumption, the stiffness and the required amount of damping for stabilization can be evaluated in a rigorous way. Compared to the state of the art, this model can be applied to

a wider range of bearing geometries and therefore constitutes an objective tool for performance comparison. Furthermore, its parameters can be identified using magnetoquasistatic finite element simulations, which facilitates the application of the model to more complex bearing geometries e.g.. Lastly, let us point out that a state-space representation corresponding to other kinds of rotor models and damping can be obtained by modifying the mechanical model of the rotor.

The tools developed in the previous sections for predicting the performance of EDBs were then applied to three case studies.

First, two EDB performance criteria were proposed, namely the radial stiffness and the instability margin. Based on a simple quasi-static model yielding an analytical formula of the system roots, a graphical method linking the stiffness and stability margin of a bearing based on the position of the root locus was presented. This method was validated, showing its applicability for interpreting the root loci obtained with the dynamic model too.

Using this method, a first case study investigated the impact of the yoke material on the performance of EDBs. Two bearings with and without ferromagnetic yoke were compared. It was shown that the negative impact of the detent force associated with a ferromagnetic yoke is well counterbalanced by an increase in the centering electrodynamic force. In some cases, the presence of a ferromagnetic yoke may improve the performance of the bearings. However, the impact of the yoke material on the bearing performance is negligible for small rotor shaft radii.

As a second case study, a bearing with no ferromagnetic yoke was optimized using the new dynamic model presented in this thesis. The optimization consisted in maximizing the bearing stiffness while minimizing the instability margin. This yielded the domain of achievable performance of the bearing, which is bounded by a Pareto frontiers of optimal bearings for different spin speeds. These optimal bearings were then compared to the existing bearings in the literature, showing their potential in terms of PM volume to stiffness ratio.

The third case study concerns the radial balancing force in a slotted PM motor. These forces are electrodynamic and can thus be predicted with the dynamic model developed for EDBs. The main assumptions of the model were validated, and the predicted forces were compared to finite element simulation results, showing a good agreement between them.

Original contributions

In summary, the main original contributions of this work are:

- Modeling

  The analysis of a new quasi-static model and the resulting guideline $q = p \pm 1$; see chapter 3 and (Dumont et al., 2014b).

  The derivation of a new dynamic model with an enlarged scope. More specifically, the use of the magnetic coenergy approach to obtain the forces, and the elimination of the current variables through an appropriate change of frame; see chapter 4 and (Dumont et al., 2016b).

  The derivation of a field model adapted to slotless bearing topologies, for the evaluation of the parameters of the lumped-parameter model; see section 5.2.2 and (Dumont et al., 2014a).

- Design

  The introduction of new topologies of heteropolar EDBs following the guideline $q = p \pm 1$; see section 2.1.8 and (Dehez et al., 2017, 2015; Dumont et al., 2016b).

- Model applications

  The establishment of a design approach considering two criteria: the stiffness and the instability margin of the bearing; see section 5.3 and (Dumont et al., 2016c).

  The establishment of a link between the position of the roots in a root locus plot, and the stiffness and stability margin of a bearing with two degrees of freedom; see section 5.1 and (Dumont et al., 2014a).

  The evaluation of the impact of the yoke material on the performance of a slotless EDB. In particular, it is shown to be negligible for small rotor shaft radii; see section 5.2 and (Dumont et al., 2014a).

  The calculation of an upper bound for the performance criteria of a yokeless heteropolar bearing; see section 5.3 and (Dumont et al., 2016c).

  The prediction of radial electrodynamic forces in a PM motor; see chapter 6 and (Dumont et al., 2016a; Kluyskens et al., 2017).

Outlook

The present work can be continued by building bearings and/or bearingless machines involving electrodynamic radial forces, using the models and performance criteria proposed in this work as design tools.

In addition, experimental tests could be carried out to validate the operation of heteropolar EDBs and the models derived in this thesis. A first test could be made in a static eccentricity configuration. This would allow to evaluate how easily the null-flux characteristic is obtained by measuring the phase current/voltage for different rotor positions. The force measurements could be compared to the model predictions, as well as the losses due to the induced currents.

A more sophisticated test could also be performed to validate the dynamic model in particular, following the path initiated at Politecnico di Torino (Cui, 2016). For example, the model predictions of the rotor kinematics and the amount of damping required for stability could be compared to experimental results.

Finally, introducing a significant amount of damping to stabilize the bearing is still the main barrier to the implementation of EDBs in practical applications. Therefore, investigating other strategies to introduce damping in a passive, contactless way is critical.

Broader considerations

The initial aim of this thesis was the advancement of the null-flux, heteropolar EDB technology. In particular, it is believed to complete the research works performed over the last decades from the modeling point of view, as the performance of all existing embodiments of null-flux heteropolar EDBs can now be predicted with a dynamic model.

However, experimental validations of this model are lacking, and subsequent works should be carried out to fill this gap. In addition to validating the model, these experimental tests shall also confirm the expected operation of heteropolar EDBs.

Besides these bearing modeling and validation aspects, the question of finding a practical application where EDBs could be implemented shall be raised. This could yield a technical framework that would allow to focus the future research efforts on more specific issues.

Finally, from a broader perspective, the results presented in this work may also find applications in fields other than bearings. For example, the effects of a possible occurrence of rotor eccentricities due to the wear of mechanical bearings in PM machines may be considered during their design process. In this case, the resulting radial electrodynamic forces and the associated increase in joule losses may be quantified through a model developed for EDBs.

Density of current stream lines

A

This section provides more details about the density of current streamlines function. A common way of calculating the magnetic flux linked by a conducting path consists in integrating the magnetic vector potential along the conductor:

$$\Phi = \oint \mathbf{A}^T \mathbf{dl}, \tag{A.1}$$

where $\mathbf{dl}$ is a vector line element that is aligned with the conductor. This formula can be generalized to take the thickness of the wire into account. In this aim, let us define the vector quantity $\mathbf{D}$ over the cross section of the wire S:

$$\mathbf{J} = \mathbf{D}i, \tag{A.2}$$

where $\mathbf{J}$ is the distribution of the current density within the conductor when a current i flows in it. The vector $\mathbf{D}$ thus yields the local direction of the current within the conductor, and the local current density when a total current of 1 A flows in the winding. As a consequence of (A.2):

$$\int_S \mathbf{D}\mathbf{dS} = 1. \tag{A.3}$$

The function $\mathbf{D}$ is denoted 'density of current streamlines' or 'density of current paths'. Using this concept, the thickness of the conductor can be taken into account in (A.1) by considering that instead of being linked by a single conducting path, the magnetic flux is linked by an infinity of conducting path distributed over the cross section of the wire, that are modeled as a density. This density is not uniformly distributed over the cross section, but follows the real current distribution as expressed in (A.2). In addition, the magnetic flux is linked by a single winding turn, which results in (A.3). To take the thickness of the wires into account, the differential $\mathbf{dl}$ is thus replaced by:

$$\mathbf{D}dSdl = \mathbf{D}dv. \tag{A.4}$$

As a result, (A.1) yields:

$$\Phi = \int_V \mathbf{A}^T \mathbf{D} dv, \tag{A.5}$$

where the volume V comprises the entire loop of wire. When considering multi-turn windings, (A.2) remains, except that i is the current amplitude in a single winding turn. Therefore, (A.3) yields:

$$\int_S \mathbf{D}\mathbf{dS} = b, \tag{A.6}$$

where b is the number of winding turns. As an example, let us consider a single straight wire with a flat cross-section where the current density is constant, as shown in Fig. A.1. In this case, the norm of $\mathbf{D}$ is:

$$D = \frac{1}{S}, \tag{A.7}$$

and its direction is the same as that of $\mathbf{dl}$. Therefore, the thickness of the wire is taken into account by replacing the differential $\mathbf{dl}$ by:

$$DdS\mathbf{dl} = \mathbf{dl}(DdS) = (D\mathbf{dl})dS = \frac{\mathbf{dl}}{dl} dl DdS = \mathbf{D}dldS = \mathbf{D}dv. \tag{A.8}$$

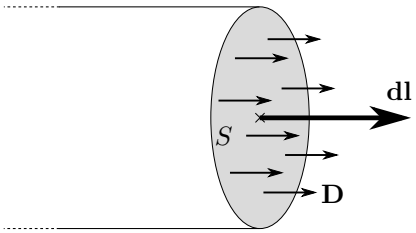

Fig. A.1: Constant density of current streamlines over the flat cross-section of the wire. The vector $\mathbf{dl}$ is the line element of the wire when its thickness is not considered.

Lastly, another example of use of the density of current streamlines can be found in (Bennecib et al., 2011).

Matrices Q

B

This appendix gathers the matrices $\mathbf{Q}$ for all four bearing configurations:

PMs on the rotor and $q = p + 1$:

$$\mathbf{Q} = \begin{bmatrix} \cos\left((q-1)\,\gamma\right) & -\sin\left((q-1)\,\gamma\right) \\ \sin\left((q-1)\,\gamma\right) & \cos\left((q-1)\,\gamma\right) \end{bmatrix}. \tag{B.1}$$

PMs on the rotor and $q = p - 1$:

$$\mathbf{Q} = \begin{bmatrix} \cos\left((q+1)\,\gamma\right) & \sin\left((q+1)\,\gamma\right) \\ \sin\left((q+1)\,\gamma\right) & -\cos\left((q+1)\,\gamma\right) \end{bmatrix}. \tag{B.2}$$

PMs on the stator and $q = p + 1$:

$$\mathbf{Q} = \begin{bmatrix} -\cos\left(-q\gamma\right) & \sin\left(-q\gamma\right) \\ -\sin\left(-q\gamma\right) & -\cos\left(-q\gamma\right) \end{bmatrix}. \tag{B.3}$$

PMs on the stator and $q = p - 1$:

$$\mathbf{Q} = \begin{bmatrix} -\cos\left(-q\gamma\right) & -\sin\left(-q\gamma\right) \\ -\sin\left(-q\gamma\right) & \cos\left(-q\gamma\right) \end{bmatrix}. \tag{B.4}$$

Transformed flux vector

C

The transformed flux vector $\mathbf{\Phi_s}$ is defined in (4.20):

$$\mathbf{\Phi^s} = K_\Phi \mathbf{U^{-1}PQx}. \tag{C.1}$$

Let us calculate $\mathbf{U^{-1}P}$. Considering (4.8) and the identities:

$$\begin{aligned} \cos(x) &= \frac{e^{jx} + e^{-jx}}{2}; \\ \sin(x) &= -j\frac{\left(e^{jx} - e^{-jx}\right)}{2}, \end{aligned} \tag{C.2}$$

the matrix $\mathbf{P}$ can be expressed as:

$$\mathbf{P} = \mathbf{G} + \mathbf{D}. \tag{C.3}$$

The components of $\mathbf{G}$ and $\mathbf{D}$ are:

$$\begin{aligned} G_{k1} = jG_{k2} &= \frac{e^{j\frac{2\pi}{N}(k-1)}}{2} \\ D_{k1} = -jD_{k2} &= \frac{e^{-j\frac{2\pi}{N}(k-1)}}{2}. \end{aligned} \tag{C.4}$$

with $k \in \{1, N\}$. Let us calculate the components of $\mathbf{U^{-1}G}$ and $\mathbf{U^{-1}D}$ separately:

$$\begin{aligned} \left[\mathbf{U}^{-1}\mathbf{G}\right]_{k1} &= \sum_{i=1}^{N} U_{ki}^{-1} G_{i1} \\ &= \frac{1}{2\sqrt{N}} \sum_{i=1}^{N} e^{j\frac{2\pi}{N}(i-1)(k-1)} e^{j\frac{2\pi}{N}(i-1)} \\ &= \frac{1}{2\sqrt{N}} \sum_{i=1}^{N} e^{j\frac{2\pi}{N}(i-1)k} \\ &= \frac{\sqrt{N}}{2}, \qquad \text{if } k = N \end{aligned} \tag{C.5}$$

and 0 otherwise. The derivation of the second column of $\mathbf{U^{-1}G}$ is straightforward:

$$\left[\mathbf{U}^{-1}\mathbf{G}\right]_{k2} = -j\left[\mathbf{U}^{-1}\mathbf{G}\right]_{k1}. \tag{C.6}$$

The term $\mathbf{U}^{-1}\mathbf{D}$ is derived in a similar way:

$$\begin{aligned}\left[\mathbf{U}^{-1}\mathbf{D}\right]_{k1} &= \sum_{i=1}^{N} U_{ki}^{-1} D_{i1} \\ &= \frac{1}{2\sqrt{N}} \sum_{i=1}^{N} e^{j\frac{2\pi}{N}(i-1)(k-1)} e^{-j\frac{2\pi}{N}(i-1)} \\ &= \frac{1}{2\sqrt{N}} \sum_{i=1}^{N} e^{j\frac{2\pi}{N}(i-1)(k-2)} \\ &= \frac{\sqrt{N}}{2}, \qquad \text{if } k = 2\end{aligned} \tag{C.7}$$

and 0 otherwise. The derivation of the second column of $\mathbf{U^{-1}D}$ is also straightforward:

$$\left[\mathbf{U}^{-1}\mathbf{D}\right]_{k2} = j\left[\mathbf{U}^{-1}\mathbf{D}\right]_{k1}. \tag{C.8}$$

Using (C.5), (C.6), (C.7) and (C.8), the matrix $\mathbf{U}^{-1}\mathbf{P}$ can be assembled:

$$\mathbf{U}^{-1}\mathbf{P} = \frac{\sqrt{N}}{2}\begin{bmatrix} 0 & 0 \\ 1 & j \\ 0 & 0 \\ \vdots & \vdots \\ 0 & 0 \\ 1 & -j \end{bmatrix}. \tag{C.9}$$

Finally, combining (C.1) and (C.9) yields:

$$\mathbf{\Phi^s} = K_\Phi \frac{\sqrt{N}}{2}\begin{bmatrix} 0 & 0 \\ 1 & j \\ 0 & 0 \\ \vdots & \vdots \\ 0 & 0 \\ 1 & -j \end{bmatrix}\mathbf{Q}\mathbf{x}. \tag{C.10}$$

State-space representation

D

Using the real notation, the equation of motion of the rotor (4.46) is:

$$M\ddot{\mathbf{x}} + C\dot{\mathbf{x}} = \mathbf{F} + \mathbf{F_e}. \tag{D.1}$$

Coupling (4.43) and (D.1) yields:

$$\begin{bmatrix} \dot{\mathbf{F}} \\ \ddot{\mathbf{x}} \\ \dot{\mathbf{x}} \end{bmatrix} = \mathbf{A} \begin{bmatrix} \mathbf{F} \\ \dot{\mathbf{x}} \\ \mathbf{x} \end{bmatrix} + \mathbf{B}\mathbf{F_e}, \tag{D.2}$$

where:

$$\mathbf{A} = \begin{bmatrix} -\frac{R}{L_c} & \omega_e & -K_d - \frac{K_\Phi^2 N}{2L_c} & 0 & -\frac{RK_d}{L_c} & \frac{\omega_e K_\Phi^2 N}{2L_c} + \omega_e K_d \\ -\omega_e & -\frac{R}{L_c} & 0 & -K_d - \frac{NK_\Phi^2}{2L_c} & \frac{-\omega_e K_\Phi^2 N}{2L_c} - \omega_e K_d & -\frac{RK_d}{L_c} \\ \frac{1}{M} & 0 & -\frac{C}{M} & 0 & 0 & 0 \\ 0 & \frac{1}{M} & 0 & -\frac{C}{M} & 0 & 0 \\ 0 & 0 & 1 & 0 & 0 & 0 \\ 0 & 0 & 0 & 1 & 0 & 0 \end{bmatrix} \tag{D.3}$$

$$\mathbf{B} = \frac{1}{M} \begin{bmatrix} 0 & 0 & 1 & 0 & 0 & 0 \\ 0 & 0 & 0 & 1 & 0 & 0 \end{bmatrix}^T. \tag{D.4}$$

Graphical approach generalization

E

In section 5.1, a graphical analysis of the root locus of bearings with two degrees of freedom and $K_\phi < 0$ was introduced. This appendix presents similar developments corresponding to $K_\phi > 0$.

In this case, the unstable root still corresponds to the plus sign in (5.5):

$$\rho = \frac{-C}{2M} + \sqrt{\left(\frac{C}{2M}\right)^2 - \frac{K_\epsilon + jK_\phi}{M}}. \tag{E.1}$$

Using the polar form for complex numbers:

$$\frac{K_\epsilon + jK_\phi}{M} = Ne^{j\alpha}, \tag{E.2}$$

where:

$$\tan(\alpha) = \frac{K_\phi}{K_\epsilon} \tag{E.3}$$

$$N = \frac{\sqrt{K_\epsilon^2 + K_\phi^2}}{M}. \tag{E.4}$$

The root locus is drawn for $C = 0$. Therefore, (E.1) and (E.2) yield[1]:

$$\rho|_{C=0} = +j\sqrt{N}e^{j\alpha/2}. \tag{E.5}$$

In the area of interest of the root locus:

[1] Only the principal square root of $\rho|_{C=0}$ is considered.

$$\left|\frac{\Re\left\{\rho|_{C=0}\right\}}{\Im\left\{\rho|_{C=0}\right\}}\right| = \tan\left(\left|\frac{\alpha}{2}\right|\right) \ll 1. \tag{E.6}$$

As a result, $|\alpha/2| \ll 1$ which can be approximated as $|\alpha| \ll 1$. Considering this, (E.3) and (E.4) yield:

$$\alpha \cong \frac{K_\phi}{K_\epsilon} \ll 1 \Rightarrow \left|\frac{K_\phi}{K_\epsilon}\right| \ll 1 \tag{E.7}$$

$$N \cong \frac{K_\epsilon}{M}. \tag{E.8}$$

A consequence of $|\alpha| \ll 1$ is that $\sin(\alpha/2) \cong \alpha/2$ and $\cos(\alpha/2) \cong 1$. Therefore, (E.5) becomes:

$$\rho|_{C=0} = +j\sqrt{N}\left(\cos\left(\frac{\alpha}{2}\right) + j\sin\left(\frac{\alpha}{2}\right)\right) \cong -\sqrt{N}\left(\frac{\alpha}{2} - j\right). \tag{E.9}$$

Replacing (E.7) and (E.8) in (E.9) yields:

$$\rho|_{C=0} \cong -\sqrt{\frac{K_\epsilon}{M}}\left(\frac{K_\phi}{2K_\epsilon} - j\right) = -\sqrt{\frac{K_\epsilon}{M}}\frac{K_\phi}{2K_\epsilon} + j\sqrt{\frac{K_\epsilon}{M}}. \tag{E.10}$$

Let us consider the effect of damping. Assuming a priori that the damping introduced in the system satisfies:

$$\left(\frac{C}{2M}\right)^2 \ll \frac{K_\epsilon}{M}, \tag{E.11}$$

(E.1) yields:

$$\rho \cong \frac{-C}{2M} + \sqrt{-\frac{K_\epsilon + jK_\phi}{M}}. \tag{E.12}$$

Combining this with (E.10) gives:

$$\rho \cong \frac{-C}{2M} - \sqrt{\frac{K_\epsilon}{M}}\frac{K_\phi}{2K_\epsilon} + j\sqrt{\frac{K_\epsilon}{M}}. \tag{E.13}$$

To achieve stabilization, the damping should be increased to satisfy $\Re\{\rho\} < 0$, which yields:

$$\frac{C_s}{2M} = -\sqrt{\frac{K_\epsilon}{M}}\left(\frac{K_\phi}{2K_\epsilon}\right), \tag{E.14}$$

where C_s is the minimum amount of damping to stabilize the bearing. This result shows that the horizontal position of $\rho|_{C=0}$ in the root locus is proportional to the level of instability of the bearing. Furthermore, considering (E.7) and (E.14) yields:

$$\left|\frac{C_s}{2M}\right| \ll \sqrt{\frac{K_\epsilon}{M}}, \tag{E.15}$$

which confirms assumption (E.11). In summary, the radial stiffness and the instability margin are linked to the unstable root locus through:

$$\begin{aligned} \Re\{\rho|_{C=0}\} &= \frac{C_s}{2M} \\ \Im\{\rho|_{C=0}\} &= \sqrt{\frac{K_\epsilon}{M}}, \end{aligned} \tag{E.16}$$

where:

$$C_s = -K_\phi\sqrt{\frac{M}{K_\epsilon}}. \tag{E.17}$$

Current vector potential

F

Let us consider a bearing comprising an axial airgap winding with k phases, q pole pairs, N turns per phase, and no ferromagnetic yoke. The rotor has surface-mounted permanent magnets and a ferromagnetic shaft. The axial active length is denoted L, and the radial geometrical parameters of the bearing are given in Fig. F.1. This section presents an analytical solution of the magnetic vector potential created by the phase currents, as well as the cyclic inductance of the winding. These expressions were derived following the same approach as in (Atallah et al., 1998).

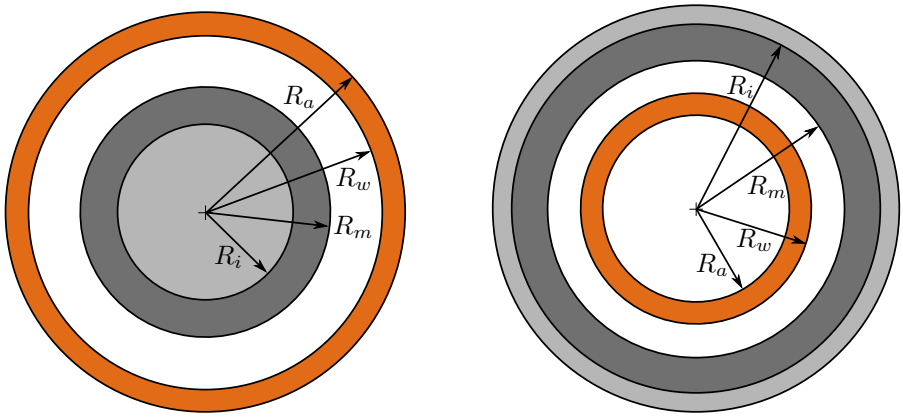

Fig. F.1: Radial geometrical parameters of the bearing. (a) External winding case. (b) Internal winding case. The airgap width is exaggerated.

External winding case

The airgap potential created by the current I_i in the phase i is:

$$A_{Iz,i}(r,\theta) = \sum_{m,odd}^{\infty} \left(C_{2m} r^{mq} + C_{3m} r^{-mq}\right) I_i \sin\left(mq(\theta - \delta_i)\right), \tag{F.1}$$

where $\delta_i = \frac{\pi i}{qk}$ is the phase angular position. The winding cyclic inductance is:

$$L_c = \sum_{m,odd}^{\infty} L\pi K_{Im} \left[\sum_{j=0}^{k-1} \cos\left(\frac{\pi j}{k}\right) \cos\left(\frac{m\pi j}{k}\right) \right] K_{Lm} \tag{F.2}$$

where L is the active length of the bearing, and:

$$\begin{aligned} K_{Lm} &= C_{1m} \frac{\left(R_a^{mq+2} - R_w^{mq+2}\right)}{mq+2} + C_{4m} \ln\left(\frac{R_a}{R_w}\right) \\ &\quad - \frac{\mu_0 K_{Im}}{64} \left[R_a^4 \left(4\ln(R_a) - 1\right) - R_w^4 \left(4\ln\left(R_w\right) - 1\right)\right] \qquad \text{if } mq = 2, \\ &= C_{1m} \frac{\left(R_a^{mq+2} - R_w^{mq+2}\right)}{mq+2} + C_{4m} \frac{\left(R_a^{2-mq} - R_w^{2-mq}\right)}{2-mq} \\ &\quad + \mu_0 K_{Im} \frac{\left(R_a^4 - R_w^4\right)}{4\left((mq)^2 - 4\right)} \qquad \text{otherwise.} \end{aligned} \tag{F.3}$$

In (F.1) and (F.2), the constants are given by:

$$K_{Im} = \frac{8Nqk}{m\pi^2 |R_w^2 - R_a^2|} \sin\left(\frac{m\pi}{2}\right) \sin\left(\frac{m\pi}{2k}\right), \tag{F.4}$$

and:

$$\begin{aligned} C_{1m} &= \frac{K_t(R_a) - K_r(R_a)}{2R_a^{mq-1}} \\ C_{2m} &= C_{1m} - \frac{K_t(R_w) - K_r(R_w)}{2R_w^{mq-1}} \\ C_{3m} &= C_{2m} R_i^{2mq} \\ C_{4m} &= C_{3m} - \frac{K_r(R_w) + K_t(R_w)}{2R_w^{-mq-1}}, \end{aligned} \tag{F.5}$$

where:

$$\begin{aligned} K_r(r) &= -\frac{\mu_0 K_{Im} r \ln(r)}{4} \qquad \text{if } mq = 2, \\ &= \frac{\mu_0 K_{Im} r}{(mq)^2 - 4} \qquad \text{otherwise.} \end{aligned} \tag{F.6}$$

$$\begin{aligned} K_t(r) &= \frac{\mu_0 K_{Im} r(2\ln(r) + 1)}{4mq} \qquad \text{if } mq = 2, \\ &= -\frac{\mu_0 K_{Im} 2r}{mq((mq)^2 - 4)} \qquad \text{otherwise.} \end{aligned}$$

Internal winding case

The airgap potential created by the current I_i in the phase i is:

$$A_{Iz,i}(r,\theta) = \sum_{m,odd}^{\infty} \left(C_{3m} r^{mq} + C_{2m} r^{-mq}\right) I_i \sin\left(mq(\theta - \delta_i)\right), \tag{F.7}$$

where $\delta_i = \frac{\pi i}{qk}$ is the phase angular position. The winding cyclic inductance is:

$$L_c = \sum_{m,odd}^{\infty} L\pi K_{Im} \left[\sum_{j=0}^{k-1} \cos\left(\frac{\pi j}{k}\right) \cos\left(\frac{m\pi j}{k}\right)\right] K_{Lm} \tag{F.8}$$

where L is the active length of the bearing, and:

$$\begin{aligned} K_{Lm} &= C_{4m} \frac{\left(R_w^{mq+2} - R_a^{mq+2}\right)}{mq+2} + C_{1m} \ln\left(\frac{R_w}{R_a}\right) \\ &\quad - \frac{\mu_0 K_{Im}}{64} \left[R_w^4 \left(4\ln(R_w) - 1\right) - R_a^4 \left(4\ln\left(R_a\right) - 1\right)\right] \qquad \text{if } mq = 2, \\ &= C_{4m} \frac{\left(R_w^{mq+2} - R_a^{mq+2}\right)}{mq+2} + C_{1m} \frac{\left(R_w^{2-mq} - R_a^{2-mq}\right)}{2-mq} \\ &\quad + \mu_0 K_{Im} \frac{\left(R_w^4 - R_a^4\right)}{4\left((mq)^2 - 4\right)} \qquad \text{otherwise.} \end{aligned} \tag{F.9}$$

In (F.7) and (F.8), the constants are given by:

$$K_{Im} = \frac{8Nqk}{m\pi^2 |R_w^2 - R_a^2|} \sin\left(\frac{m\pi}{2}\right) \sin\left(\frac{m\pi}{2k}\right), \tag{F.10}$$

and:

$$\begin{aligned} C_{1m} &= -\frac{K_r(R_a) + K_t(R_a)}{2R_a^{-mq-1}} \\ C_{2m} &= C_{1m} + \frac{K_r(R_w) + K_t(R_w)}{2R_w^{-mq-1}} \\ C_{3m} &= C_{2m} R_i^{-2mq} \\ C_{4m} &= C_{3m} + \frac{K_t(R_w) - K_r(R_w)}{2R_w^{mq-1}}, \end{aligned} \tag{F.11}$$

where:

$$\begin{aligned} K_r(r) &= -\frac{\mu_0 K_{Im} r \ln(r)}{4} \qquad \text{if } mq = 2, \\ &= \frac{\mu_0 K_{Im} r}{(mq)^2 - 4} \qquad \text{otherwise.} \end{aligned} \tag{F.12}$$

$$\begin{aligned} K_t(r) &= \frac{\mu_0 K_{Im} r(2\ln(r) + 1)}{4mq} \qquad \text{if } mq = 2, \\ &= -\frac{\mu_0 K_{Im} 2r}{mq((mq)^2 - 4)} \qquad \text{otherwise.} \end{aligned}$$

Some of the previous results are validated in (Dumont et al., 2016d).

Bibliography

Andrews, J. A. and Pinkerton, J. F. (1996). Magnetic bearing with phase-shifted loops. US Patent 5,508,573.

Atallah, K., Zhu, Z. Q., and Howe, D. (1998). Armature reaction field and winding inductances of slotless permanent-magnet brushless machines. *IEEE Transactions on Magnetics*, 34(5):3737–3744.

Bachovchin, K. D., Hoburg, J. F., and Post, R. F. (2013). Stable levitation of a passive magnetic bearing. *IEEE Transactions on Magnetics*, 49(1):609–617.

Basore, P. A. (1980). *Passive stabilization of flywheel magnetic bearings*. PhD thesis, Department of Electrical Engineering and Computer Science, Massachusets Institute of Technology.

Bender, D. A. and Post, R. F. (2000). Ambient-temperature passive magnetic bearings for flywheel energy storage systems. In *Proceedings of the Seventh International Symposium on Magnetic Bearings*, pages 153–158, Zurich, Switzerland.

Bennecib, N., Matagne, E., and Dehez, B. (2011). Circuit model of a magneto-hydrodynamic dc pump. In *Proceedings of Tenth International Conference on Modeling and Simulation of Electric Machines, Converters and Systems*, Cergy-Pontoise, France.

Braunbek, W. (1939a). Freies schweben diamagnetischer körper im magnetfeld. *Zeitschrift für Physik*, 112(11):764–769.

Braunbek, W. (1939b). Freischwebende körper im elektrischen und magnetischen feld. *Zeitschrift für Physik*, 112(11):753–763.

Burakov, A. and Arkkio, A. (2006). Low-order parametric force model for eccentric-rotor electrical machine with parallel connections in stator winding. *IEE Proceedings - Electric Power Applications*, 153(4):592–600.

Burakov, A. and Arkkio, A. (2007). Comparison of the unbalanced magnetic pull mitigation by the parallel paths in the stator and rotor windings. *IEEE Transactions on Magnetics*, 43(12):4083–4088.

Chiba, A., Fukao, T., Ichikawa, O., Takemoto, M., and Dorrell, D. G. (2005). *Magnetic Bearings and Bearingless Drives*. Elsevier.

Clifton, D. B., Little, S. R., and Pinkerton, J. F. (1995). Null flux magnetic bearing with cross-connected loop portions. US Patent 5,471,105.

Cui, Q. (2016). *Stabilization of Electrodynamic Bearings with Active Magnetic Dampers*. PhD thesis, Laboratoire de systèmes robotiques, Ecole polytechnique fédérale de Lausanne EPFL, Lausanne, Switzerland.

Danby, G. T. (1971). Electromagnetic suspension and positioning device with inherent dynamical stability in three dimensions. US Patent 3,572,854.

Davey, K., Filatov, A., and Thompson, R. (2005). Design and analysis of passive homopolar flux bearings. *IEEE Transactions on Magnetics*, 41(3):1169–1175.

Davey, K. R. (1996). Passive null flux coil magnetic bearing system for translation or rotation. US Patent 5,481,146.

Davey, K. R. (1997). Designing with null flux coils. *IEEE Transactions on Magnetics*, 33(5):4327–4334.

Davey, K. R. (2003). Use and analysis of null flux coils. *COMPEL - The international journal for computation and mathematics in electrical and electronic engineering*, 22(2):304–313.

Dehez, B., Dumont, C., Kluyskens, V., and Baudart, F. (2017). Electric machine having a radial electrodynamic bearing. EU Patent 3118976A1.

Dehez, B., Kluyskens, V., Dumont, C., and Beneden, M. V. (2015). Radial electrodynamic bearing. WO Patent 2015/024830 A1.

Detoni, J., Impinna, F., Tonoli, A., and Amati, N. (2012). Unified modelling of passive homopolar and heteropolar electrodynamic bearings. *Journal of Sound and Vibration*, 331(19):4219 – 4232.

Detoni, J. G. (2012). *Development on Electrodynamic Levitation of Rotors*. PhD thesis, Department of Mechanical and Aerospace Engineering, Politecnico di Torino, Turin, Italy.

Detoni, J. G. (2014). Progress on electrodynamic passive magnetic bearings for rotor levitation. *Proceedings of the Institution of Mechanical Engineers, Part C: Journal of Mechanical Engineering Science*, 228(10):1829–1844.

Detoni, J. G., Impinna, F., Amati, N., and Tonoli, A. (2016). Stability of a four-degree-of-freedom rotor on homopolar electrodynamic passive magnetic bearings. *Proceedings of the Institution of Mechanical Engineers, Part I: Journal of Systems and Control Engineering*, 230(4):330–338.

Dorrell, D. G., Hsieh, M. F., and Guo, Y. (2009). Unbalanced magnet pull in large brushless rare-earth permanent magnet motors with rotor eccentricity. *IEEE Transactions on Magnetics*, 45(10):4586–4589.

Dorrell, D. G. and Ionel, D. (2012). Radial forces and vibrations in permanent magnet and induction machines. In *2012 IEEE Power and Energy Society General Meeting*, pages 1–6.

Dumont, C., Gilson, A., Kluyskens, V., Espanet, C., and Dehez, B. (2016a). Evaluation of the electrodynamic forces in high-speed permanent magnet machines with rotor eccentricity. In *Proceedings of the Fifteenth International Symposium on Magnetic Bearings*, Kitakyushu, Japan.

Dumont, C., Kluyskens, V., and Dehez, B. (2014a). Impact of the yoke material on the performance of wound electrodynamic bearings. In *Proceedings of the Fourteenth International Symposium on Magnetic Bearings*, pages 275–280, Linz, Austria.

Dumont, C., Kluyskens, V., and Dehez, B. (2014b). Null-flux radial electrodynamic bearing. *IEEE Transactions on Magnetics*, 50(10):1–12.

Dumont, C., Kluyskens, V., and Dehez, B. (2016b). Linear state-space representation of heteropolar electrodynamic bearings with radial magnetic field. *IEEE Transactions on Magnetics*, 52(1):1–9.

Dumont, C., Kluyskens, V., and Dehez, B. (2016c). Performance of yokeless heteropolar electrodynamic bearings. In *Proceedings of the conference Advances in Magnetics - AIM*, Bormio, Italy.

Dumont, C., Kluyskens, V., and Dehez, B. (2016d). Yokeless radial electrodynamic bearing. *Mathematics and Computers in Simulation*, 130:57 – 69. 11th International Conference on Modeling and Simulation of Electric Machines, Converters and Systems.

Earnshaw, S. (1842). On the nature of the molecular forces which regulate the constitution of the luminiferous ether. *Transactions of the Cambridge Philosophical Society*, 7:97–112.

Eichenberg, D. J., Gallo, C. A., and Thompson, W. K. (2006). Development and testing of a radial halbach magnetic bearing. Technical Report NASA/TM-2006-214477, National Aeronautics and Space Administration, Glenn Research Center, Cleveland, Ohio.

Filatov, A. (2002). *Null-E Magnetic Bearings*. PhD thesis, Department of Mechanical and Aerospatial Engineering, School of Applied Sciences, University of Virginia, Blacksburg, USA.

Filatov, A. V. and Maslen, E. H. (2001). Passive magnetic bearing for flywheel energy storage systems. *IEEE Transactions on Magnetics*, 37(6):3913–3924.

Genta, G. (2005). *Dynamics of Rotating Systems*. Springer-Verlag New York.

Genta, G., Delprete, C., and Rondano, D. (1999). Gyroscopic stabilization of passive magnetic levitation. *Meccanica*, 34(6):411–424.

Gilson, A., Tavernier, S., Gerber, M., Espanet, C., Dubas, F., and Depernet, D. (2015). Design of a cost-efficient high-speed high-efficiency pm machine for compressor applications. In *2015 IEEE Energy Conversion Congress and Exposition (ECCE)*, pages 3852–3856.

Grenier, D., Labrique, F., Buyse, H., and Matagne, E. (2009). *Électromécanique: convertisseurs d'énergie et actionneurs*. Sciences SUP. Cours et exercices corrigés. Dunod.

Han, Y. H., Hull, J. R., Han, S. C., Jeong, N. H., Sung, T. H., and No, K. (2005). Design and characteristics of a superconductor bearing. *IEEE Transactions on Applied Superconductivity*, 15(2):2249–2252.

Impinna, F., Detoni, J. G., Amati, N., and Tonoli, A. (2013). Passive magnetic levitation of rotors on axial electrodynamic bearings. *IEEE Transactions on Magnetics*, 49(1):599–608.

Jungmayr, G., Marth, E., Amrhein, W., Berroth, H. J., and Jeske, F. (2014). Analytical stiffness calculation for permanent magnetic bearings with soft magnetic materials. *IEEE Transactions on Magnetics*, 50(8):1–8.

Kasten, H. and Redemann, C. (2014). Influence on unbalanced magnetic pull. In *Proceedings of the Fourteenth International Symposium on Magnetic Bearings*, pages 758–761.

Kim, U. and Lieu, D. K. (2005). Effects of magnetically induced vibration force in brushless permanent-magnet motors. *IEEE Transactions on Magnetics*, 41(6):2164–2172.

Kluyskens, V. (2011). *Electromechanical Model for the Dynamical Behavior of Magnetic Bearings Subjected to Induced Currents*. PhD thesis, Ecole Polytechnique de Louvain, Université catholique de Louvain, Louvain-la-Neuve, Belgium.

Kluyskens, V. and Dehez, B. (2009). Parameterized electromechanical model for magnetic bearings with induced currents. *Journal of System Design and Dynamics*, 3(4):453–461.

Kluyskens, V. and Dehez, B. (2013). Dynamical electromechanical model for magnetic bearings subject to eddy currents. *IEEE Transactions on Magnetics*, 49(4):1444–1452.

Kluyskens, V., Dumont, C., and Dehez, B. (2017). Description of an electrodynamic self-bearing permanent magnet machine. *IEEE Transactions on Magnetics*, 53(1):1–9.

Lembke, T. A. (2005). *Design and Analysis of a Novel Low Loss Homopolar Electrodynamic Bearing*. PhD thesis, Department of Electrical Engineering, Royal Institute of Technology, Stockholm, Sweden.

Li, J. T., Liu, Z. J., and Nay, L. H. A. (2007). Effect of radial magnetic forces in permanent magnet motors with rotor eccentricity. *IEEE Transactions on Magnetics*, 43(6):2525–2527.

Looser, A. and Kolar, J. W. (2014). An active magnetic damper concept for stabilization of gas bearings in high-speed permanent-magnet machines. *IEEE Transactions on Industrial Electronics*, 61(6):3089–3098.

Murakami, C. (1995). All-passive-type rotary magnetic bearing system based on stability principle of sleeping tops. *JSME international journal. Ser. C, Dynamics, control, robotics, design and manufacturing*, 38(3):601–608.

Murakami, C., Satoh, I., Shirao, Y., and Kanemitsu, Y. (1996). Principle and experiments of an all-passive-type magnetic bearing system. In *Proceedings of the Fifth International Symposium on Magnetic Bearings*, pages 491–496, Kanazawa, Japan.

Pinkerton, J. F. (1994). Magnetic bearing and method utilizing movable closed conductive loops. US Patent 5,302,874.

Post, R. F. (1996). Dynamically stable magnetic suspension/bearing system. US Patent 5,495,221.

Post, R. F. (1998). Passive magnetic bearing element with minimal power losses. US Patent 5,847,480.

Post, R. F. (1999). A combination of a passive magnetic bearing element and generator/motor. World Patent 99/39424.

Post, R. F. (2000). Stability issues in ambient-temperature passive magnetic bearing systems. Technical Report UCRL-ID-137632, Lawrence Livermore National Laboratory.

Post, R. F. (2006). Passive magnetic bearing for a motor-generator. US Patent 7,078,838.

Post, R. F. (2012). Passive magnetic bearing system. US Patent 2012/0175985.

Post, R. F. and Ruytov, D. D. (1998). Ambient-temperature passive magnetic bearings: theory and design equations. In *Proceedings of the Sixth International Symposium on Magnetic Bearings*, pages 110–122, Cambridge, USA.

Rahideh, A. and Korakianitis, T. (2011). Analytical open-circuit magnetic field distribution of slotless brushless permanent-magnet machines with rotor eccentricity. *IEEE Transactions on Magnetics*, 47(12):4791–4808.

Sandtner, J. and Bleuler, H. (2004). Electrodynamic passive magnetic bearing with planar halbach arrays. In *Proceedings of the Ninth International Symposium on Magnetic Bearings*, Lexington, USA.

Schweitzer, G. and Maslen, E. H., editors (2009). *Magnetic Bearings*. Springer-Verlag Berlin Heidelberg, 1 edition.

Silber, S., Grabner, H., Amrhein, W., and Lohninger, R. (2012). Design aspects of bearingless torque motors. In *Proceedings of the Thirteenth International Symposium on Magnetic Bearings*, Virginia, USA.

SKF (2016). Skf s2m magnetic bearings for the oil and gas industry. website booklet.

Takanashi, T., Matsuya, Y., Ohtsuka, Y., and Nishikawa, M. (2006). Analysis of magnetic bearing using inductive levitation by relative motion between magnet and conductor. *IEEJ Transactions on Industry Applications*, 126(12):1699–1705.

Tonoli, A., Amati, N., Impinna, F., and Detoni, J. G. (2011). A solution for the stabilization of electrodynamic bearings: Modeling and experimental validation. *ASME Journal of Vibration and Acoustics*, 133(2):021004–10.

White, D. C. and Woodson, H. H. (1959). *Electromechanical Energy Conversion*. Wiley, NY, USA.